

박사 학위논문
Ph. D. Dissertation

반도체 박막을 이용한 테라헤르츠 전자기파
발생과 응용에 관한 연구

Terahertz wave generation from semiconductor thin films and its
applications

이 민 우 (李旻雨 Yi, Minwoo)

물리학과

Department of Physics

KAIST

2012

반도체 박막을 이용한 테라헤르츠 전자기파 발생과 응용에 관한 연구

Terahertz wave generation from semiconductor thin films and its
applications

Terahertz wave generation from semiconductor thin films and its applications

Advisor : Professor Ahn, Jaewook

by

Yi, Minwoo

Department of Physics

KAIST

A thesis submitted to the faculty of KAIST in partial fulfillment of the requirements for the degree of Doctor of Philosophy in the Department of Physics . The study was conducted in accordance with Code of Research Ethics¹.

2012. 5. 4.

Approved by

Professor Ahn, Jaewook

[Advisor]

¹Declaration of Ethical Conduct in Research: I, as a graduate student of KAIST, hereby declare that I have not committed any acts that may damage the credibility of my research. These include, but are not limited to: falsification, thesis written by someone else, distortion of research findings or plagiarism. I affirm that my thesis contains honest conclusions based on my own careful research under the guidance of my thesis advisor.

반도체 박막을 이용한 테라헤르츠 전자기파 발생과 응용에 관한 연구

이 민 우

위 논문은 한국과학기술원 박사학위논문으로
학위논문심사위원회에서 심사 통과하였음.

2012년 5월 4일

심사위원장 안 재 욱 (인)

심사위원 김 병 윤 (인)

심사위원 정 기 훈 (인)

심사위원 조 영 달 (인)

심사위원 조 용 훈 (인)

DPH
20057956

이 민 우. Yi, Minwoo. Terahertz wave generation from semiconductor thin films and its applications. 반도체 박막을 이용한 테라헤르츠 전자기파 발생과 응용에 관한 연구. Department of Physics . 2012. 76p. Advisor Prof. Ahn, Jaewook. Text in English.

ABSTRACT

Pulsed terahertz (THz) wave technology that utilizes ultrafast laser system for THz waves generation and detection has been studied extensively for several decades. It has seen great success and interest in spectroscopy and more applications are being developed such as security scanning, bio-chemical identification, defect characterization, and so on. However, the major technical obstacles for most THz imaging and applications are absorption loss by water vapor, the difficulty in miniaturizing the system size, and the rather poorer imaging resolution than that of the conventional spectral region. Also, to overcome low signal to noise ratio, several types of semiconductors for the purpose of powerful THz wave generation and its application have been investigated. Narrow band gap semiconductor such as InAs has attracted more and more interest due to their powerful THz wave generation via photo-Dember effect. With a comparatively longer wavelength, Rayleigh's criterion limits its use for imaging of single cells and other microstructures. Typical human cell sizes range from a few to hundreds of microns. A method for achieving sub-wavelength resolution is to adopt near-field imaging techniques by the usage of a small aperture, near-field tip, focused optical laser beam. In this manner, we have developed sub-wavelength THz emission microscope by using MBE-grown thin InAs film and small optical-fiber THz emission tip.

In this dissertation, we have studied and demonstrated a new method of displaying temporal phase information of THz pulses for sub-wavelength imaging, whereby a semiconductor film with diffraction apertures is illuminated by ultrafast laser pulses to produce THz waves. Temporal phase advancement of THz pulses occurs when THz pulses are generated from sub-wavelength InAs emission apertures. This temporal phase shift is explained by transverse spatial confinement of sub-wavelength THz radiation from thin InAs apertures. The geometrical phase shift of radiated THz waves has been induced when the spatial frequency of the beam size is larger than wavenumber k . This phase shift behavior can be applied to sensitive recognition of micrometer-size patterns smaller than the wavelength of THz pulses. Also, we have devised and constructed an optical-fiber THz emitter using a (100)-oriented InAs thin film placed on a 45-degree wedged optical-fiber tip. Using this method, the THz imaging resolution is expected to be improved to the size of the optical-fiber core. The designed compact THz emission tip here can be extended to near-field imaging, spectroscopy, polarization studies, and remote sensing with sub-wavelength resolution. Furthermore, we have shown the developed functional THz imaging system by using intendedly shaped THz pulses via optical pulse shaping technique. Adaptively pre-designed THz pulses with the evaluation of cost function for material spectral response have enabled THz pulsed spectroscopy and imaging since spectral phase modulations in a spatial light pulse shaper on Fourier domain produce tailored THz pulses with different spectral sensitiveness. As a result, we have acquired THz functional images by elaborately shaped THz pulses. This shaped THz pulse imaging system enhances the contrast of THz image.

Keywords: Terahertz, Diffraction theory, Near-field imaging, Optical Fiber, Terahertz imaging, Pulse shaping

Contents

Abstract	i
Contents	ii
List of Tables	iv
List of Figures	v
Chapter 1. Introduction	1
Chapter 2. Terahertz spectrum and spectroscopy	3
2.1 Terahertz spectrum	3
2.2 Terahertz radiation and spectroscopy	4
2.2.1 Generation of terahertz electromagnetic waves	4
2.2.2 Optical sampling of terahertz electromagnetic waves	5
2.2.3 Terahertz time-domain spectroscopy	6
Chapter 3. Sub-wavelength THz pulse radiation and imaging	7
3.1 Introduction	7
3.2 Terahertz pulses generation from semiconductor surfaces	7
3.2.1 Optical rectification	8
3.2.2 Surface depletion field	9
3.2.3 Photo-Dember effect	10
3.3 Terahertz near-field imaging	11
3.3.1 The far-field and near-field spatial region	12
3.3.2 Review of the methods for terahertz near-field imaging	12
3.4 Sub-wavelength THz radiation from thin InAs film	15
3.4.1 MBE-grown thin InAs fabrication	15
3.4.2 The resolution of THz pulse from thin InAs film	19
Chapter 4. Terahertz phase microscopy in the sub-wavelength regime	25
4.1 Introduction	25
4.2 Experimental description	25
4.3 The Gouy phase shift of sub-wavelength emission aperture	26
4.4 Terahertz sub-wavelength phase microscopy	29
4.5 Discussion	30

Chapter 5.	Terahertz optical fiber emitter	32
5.1	Introduction	32
5.2	Experimental description	32
5.3	Terahertz optical fiber emitter and imaging	36
5.4	Discussion	39
Chapter 6.	Terahertz shaped pulse spectroscopy and imaging	41
6.1	Introduction	41
6.2	Femtosecond optical pulse shaping	42
6.2.1	Acousto-optic modulator	43
6.2.2	Liquid crystal modulator	43
6.2.3	Phase-only Fourier-domain pulse shaping	46
6.3	Experimental description	51
6.4	Linear response function for shaped terahertz pulses	52
6.5	Adaptive terahertz pulse shaping	56
6.6	Shaped terahertz pulses sensitive to spectral response materials	58
6.7	Terahertz spectral correlation imaging	62
6.8	Discussion	63
Chapter 7.	Conclusion	64
7.1	Summary	64
7.2	Future work	64
References		68
Summary (in Korean)		77

List of Tables

3.1	Properties of selected semiconductor materials	8
3.2	Calculated waist, corresponding THz wavelength and fitted waist to wavelength ratio. . .	24

List of Figures

2.1	The electromagnetic spectrum spanning from microwaves to X-rays. THz frequency region between microwaves and infrared waves spans over frequencies from 0.1 to 10 THz.	3
3.1	Optical geometry for generation of THz radiation from a semiconductor surface.	9
3.2	Band diagram and the schematic flow of drift current in (a) <i>n</i> -type and (b) <i>p</i> -type semiconductors	10
3.3	Schematic diagram of diffusion current by photoexcited carriers near the surface of a semiconductor	11
3.4	A three-dimensional spatial and temporal carrier concentration distribution of photoexcited electrons and holes at the InAs surface. The gray curves represent electron distribution and the dark curves represent the hole distribution [25].	15
3.5	The incident angular dependence of radiated TM-THz power (circle) from thin InAs film for <i>p</i> -polarized optical excitation beam and calculated TM radiation field for <i>p</i> -polarized (red) and <i>s</i> -polarized (black) optical beam.	17
3.6	The azimuthal dependence of THz wave generation from differently-oriented InAs surfaces. The squares and circles represent the experimental measurements of THz wave amplitude from a (111) oriented <i>n</i> -type InAs with a doping concentration at $3 \times 10^{16} \text{cm}^{-3}$ and a (100) oriented <i>p</i> -type InAs with a doping concentration at $1 \times 10^{18} \text{cm}^{-3}$, respectively. The curves represent the fitting results by cosine equations.	17
3.7	The result of X-ray Diffraction for MBE-grown (100) InAs film on MgO substrate.	18
3.8	1- μm -thick InAs thin film fabrication layout.	18
3.9	(a) Layout and (b) schematic diagram of transmissive sub-wavelength THz emission microscope.	19
3.10	Measured temporal THz pulses and its spectrum up to 2 THz from sub-wavelength THz emission microscope with 1- μm -thick InAs film.	19
3.11	Measured THz-peak image of knife-edge experiment using half filled InAs film at fixed temporal position. The spatial resolution of the THz-peak image is measured about 10 μm by the 10% - 90% method ($X_{10-90} = 2 \times 0.64w_x = 14 \mu\text{m}$).	20
3.12	The THz-peak image of single mode optical fiber (HP780, Nufern) with 125- μm -diameter cladding. Cladding diameter is slightly smaller than $\lambda_0/2$. The image shows the cladding region of optical fiber and do not resolve the core of optical fiber with 5.5 μm , which is smaller than the resolution of developed THz microscope.	21
3.13	(a) Measured THz temporal signals and (b) their spectra as a function of different spatial position scanned on the surface of half-filled InAs film for edge response experiment	22
3.14	Radiated THz spectral amplitude profile (circles) taken using the translating edge response method. The red line are fitted by Eq. 3.18.	23
3.15	The ratio between evaluated THz waist and THz wavelength for different wavelength components. The ratio shows that longer wavelength components exhibit marked near-field properties.	24

4.1	Schematic diagram of transmissive sub-wavelength THz phase microscope	26
4.2	(a) Temporal and (b) spectral THz waveforms generated from InAs apertures varying the diameter from 30 to 200 μm	27
4.3	The schematic experimental setup for direct observation of Gouy phase shift showing the lens configurations: (a) collimated and (b) focused configuration. (c) Dashed and solid curve: measured THz pulse in the collimated configuration (a) and the focused configuration (b), respectively [87].	28
4.4	Calculated Gouy phase shifts ϕ_G of THz pulses radiated from sub-wavelength emission apertures. The Gouy phase shifts ϕ_G for three different-size apertures, $w_1 = \lambda/40$ (black), $w_2 = \lambda/20$ (red), and $w_3 = \lambda/40$ (blue) are plotted with ϕ_G^0 (dashed line) of the one from a large-size aperture ($w = 2\lambda$).	29
4.5	(a) Radiated THz pulses for three different-size InAs emission apertures; 50-(blue), 100-(red), and 200- μm (black) from bottom to top. (b) The centroid time of radiated THz pulses for various different-size InAs emission apertures from 30 to 200 μm (circle) and calculated temporal advancement of THz pulses (dashed line).	30
4.6	(a) The microscope image of hexagram which consists of 30-, 50- and 100- μm diameter InAs emission apertures. (b) Measured THz intensity image and (c) THz temporal phase image scanned with 60- μm -diameter NIR pulses.	31
5.1	(a) Schematic diagram of the optical-fiber THz emitter and (b) microscopic photograph of 45-degree angle cut optical fiber.	33
5.2	InAs film fabrication layout.	33
5.3	Setup photograph of the THz optical-fiber tip in a near-field microscope application. . . .	34
5.4	(a) Measured THz temporal waveform from the optical-fiber THz emitter and (b) The amplitude spectrum of the THz pulse shown in (a).	35
5.5	(a) Measured temporal THz image of horizontal components of the THz field emitted from the fiber tip as a function of rotation angle. (b) The sinusoidal angle dependence around the optical axis at three different times (dashed line) shown in (a).	36
5.6	(a) Optical power dependence of measured THz pulses from the devised optical-fiber THz emitter (star) and a bare InAs film attached to a 500- μm -thick sapphire substrate (solid line). (b) The optical beam diameter dependence on measured THz power from the bare InAs film at some different optical power.	37
5.7	(a) A knife-edge THz image using an 18- μm -thick aluminum foil. (b) The lateral THz amplitude profile taken from a line as drawn in (a).	38
5.8	(a) Optically magnified photo of the metal sieve and an overall view (inset). (b) A THz near-field image superimposed on an optical microscope image. (c) Measured THz amplitude as a function of lateral position at dashed line in (b).	40
6.1	A concept of femtosecond laser pulse shaping.	42
6.2	Concept diagram of the pulse shaping with an acousto-optic programmable dispersive filters [125].	43
6.3	(a) 4 <i>f</i> -type pulse shaper with a computer controlled spatial light modulator with two grating-lens and (b) Schematic diagram of a liquid crystal modulator.	44

6.4	Dual modulator systems for shaping both spectral amplitude and phase. (a) Polarization of the incident laser pulse E_{in} relative to the liquid crystal axis of first and second SLM. (b) The structure of dual light modulator.	45
6.5	The modulation and phase shift as a function of SLM drive at 775 nm Ti:sapphire cw laser.	46
6.6	The required SLM drive as a function of intended phase retardation.	47
6.7	The pixel calibration map and the position of wavelength for each pixel number.	47
6.8	The relative modulation as a function of wavelength. The modulation is a unit at 633nm.	48
6.9	Design of phase-only shaping masks by simulated annealing algorithms.	49
6.10	Operation of the GS algorithm. The two constraints of the problem are applied sequentially in time and frequency domains.	50
6.11	A schematic experimental diagram. A grating pair and a spatial light modulator (SLM) in the pump beam path is used for optical pulse shaping. The pulse shaping apparatus consists of a pair of 1800 lines/mm placed at the focal planes of a pair of cylindrical lens and a programmable liquid crystal modulator with 128 pixels at the Fourier plane of the shaper. The other probe beam is used to gate generated THz waveforms into the <110> ZnTe sampler.	51
6.12	The total response functions of THz system in temporal and spectral domain, $H(t)$ and $ \tilde{H}(\omega) $. These response functions are empirically measured by using unshaped optical pulses and used to anticipate shaped THz pulses from shaped optical pulses via phase-only pulse shaping.	53
6.13	Calculated temporal (middle) and spectral (right) THz pulses from different two optical pulses with different temporal spacing.	54
6.14	Demonstration of four different shaped optical intensity profiles and calculated THz pulses with multiple peaks from one to four pulses. The intended optical pulse (left), and temporal (middle) and spectral (right) THz waveforms are shown.	54
6.15	Measured temporal (middle) and spectral (right) THz pulses from different two optical pulses with different temporal spacing. The measured cross correlations (star) with numerical target pulse (red) are also shown in the left panel.	55
6.16	Experimental results of four different shaped optical intensity profiles and designed THz pulses with multiple peaks from one to four pulses. The cross correlation signal (left), and temporal (middle) and spectral(right) THz waveforms are shown.	55
6.17	Optimization procedure for adaptive THz pulse shaping. In each iteration a random phase change array is generated and added to the current phase-mask to to optimize the spectral correlation. After the output shaped THz pulses are measured to calculate the spectral correlation, the change in the phase mask array is accepted if the correlation change is larger than that of the last accepted change, and rejected otherwise.	57
6.18	(a, b) The norm of the electric field at resonance frequency, and (c) the calculated THz spectral profiles for two ETMs. The red region in the gap indicates strong local field enhancement. ETM1 and ETM1 have the resonance characteristics at 0.47 and 0.77 THz, respectively.	58

6.19	(a) The photographs of electric THz metamaterials used in this experiment. (b) The power of measured THz signals through ETM1 materials as a function of unit-cell distance of ETM1 (a_1). The unit-cell distance of ETM2 are fixed while that of ETM1 are changed to manipulate the sum of squared THz signal. By considering the measurement error, the measured power of transmitted THz signals through two ETMs are similar when the distance of unit cell for ETM1 and ETM2 are 54 and 50 μm , respectively. The temporal (c) and spectral (d) characteristics of those materials passing unshaped THz pulses for ETM1 ($a_1 = 50$ and 54 μm , blue and red) and ETM2 ($a_2 = 50\mu m$, black). There exist electrical resonances for 0.5 (ETM1) and 0.8 THz (ETM2), respectively.	59
6.20	(a) The maximization of measured cost function as a function of iteration number for the optimization procedure. Circles denote the fitness values found during the optimization procedure. During the procedure, total five correlation evolution are observed. (b) The normalized correlation value divided by the initial value measured by zero phase modulation as a function of the evolution number. The observed correlation enhancement is about 25 times compared to the initial error level.	60
6.21	(a) Measured THz waveforms and (b) their THz spectra tailored by the adaptive THz pulse shaping from the zeroth to the fifth evolution number. With an increase in the evolution number, measured THz waveforms and spectra are significantly change. These spectral change results on the change in absorption when shaped THz pulses transmit through two ETMs. For the fifth evolution, the optimally shaped THz pulse is highly sensitive around 0.5 THz by the attenuation and relatively nonsensitive around 0.8 THz, inversely.	61
6.22	(a) An imaging target consists of two different THz metamaterials, where the left half circle is filled with ETM1 of 0.5 THz resonance frequency and the right half with the other with 0.8 THz. (b, c) Measured THz power images with different THz pulses for the zeroth- and fifth-evolution phase-mask array, respectively. A shaped THz pulse image with fifth-evolution phase pattern shows the highest contrast than others since this last phase-mask array has the largest cost value. (d) Measured THz power as function of lateral x -position at dashed line in (b) and (c). This plot shows the relative contrast of THz images for initial (0th-) and final (5th-) evolution THz pulses.	62
7.1	Simulation of the near-field current density distribution for THz electrical resonance materials (ETM1 and ETM2).	65
7.2	Optical microscope images of (a) sperms and (b) red blood cells (Image courtesy of University of Kansas Medical Center and Exploratorium).	65

Chapter 1. Introduction

Terahertz (THz) radiation is electromagnetic radiation whose frequency lies between the microwave and infrared bands of spectral ranging from 0.1 to 10 THz ($1 \text{ THz} = 10^{12} \text{ cycles/s}$). The electromagnetic spectrum of THz radiation has not been historically studied due to the inefficient and unstable generation and detection techniques and high atmospheric absorption for the THz radiation. In Chapter 2, we introduce the properties of THz radiation and the techniques for generating and detecting it for THz spectroscopy and imaging in which there are still some issues in these applications. Current pulsed THz wave emitters offer extremely low conversion efficiency from the input laser power into THz wave power and a lock-in amplifier has to be used to single out the signal from the noise. The high water vapor absorption significantly weakens the THz wave signal during its propagation in the free-space air. Accomplishing remote sensing with THz wave in the air is very difficult. All these issues could be resolved by improving the systems with large signal-to-noise ratio (SNR). Several approaches are investigated to enhance the THz wave radiation from semiconductor surfaces: increasing the built-in surface electric field by modification of the surface structure; seeking novel materials with large electron mobility and small band gap; reducing the doping concentration to weaken the screening of the THz radiation; adjusting the photoexcited dipole orientation for appropriate radiation direction; etc.

Narrow band gap semiconductor such as InAs has attracted more and more interest due to their powerful THz wave generation. In Chapter 3, we study the several basic mechanisms of THz pulse generation from semiconductor surfaces. Three mechanisms are explained and specified: the optical rectification, the surface depletion field, and the photo-Dember effect. With the explanation of THz generation mechanism from semiconductor surfaces, various THz near-field spectroscopy and imaging techniques are reviewed. THz imaging offers many attractive advantages for applications in material characterization, microelectronics, medical diagnosis, environmental control, and chemical and biological identification. With a comparatively longer wavelength ($300 \mu\text{m} = 1 \text{ THz}$), Rayleigh's criterion limits its use for imaging of single cells and other microstructures. Typical human cell sizes range from a few to hundreds of microns. A method for breaking the Rayleigh's criterion and thus achieving sub-wavelength resolution is to adopt near-field imaging techniques. For overpassing this low imaging resolution, several technical advances of THz imaging and microscopy have developed by the usage of a small aperture, near-field tip, focused optical laser beam. In this manner, we have developed sub-wavelength THz emission microscope by using MBE-grown thin InAs film because the photocarriers in thin InAs film are enough to radiate THz waves.

In general, amplitude of temporal signals and magnitude of spectral signals are used for THz imaging applications. Even though there are many methodological and practical attempts for more advanced and developed THz imaging and microscopy, the method of how to use plentiful information of broad band THz pulses has not been extensively studied so far. In Chapter 4, we have studied and demonstrated a new method of displaying temporal phase information of THz pulses for sub-wavelength imaging, whereby a semiconductor film with diffraction apertures is illuminated by ultrafast laser pulses to produce THz waves. Temporal phase advancement of THz pulses occurs when THz pulses are generated from sub-wavelength InAs emission apertures. This temporal phase shift is explained by transverse spatial confinement of sub-wavelength THz radiation from thin InAs apertures. This phase shift behavior can be

applied to sensitive recognition of micrometer-size patterns smaller than the wavelength of THz pulses. The imaging results show that the difference of temporal phase in time-delay domain can resolve small objects. In Chapter 5, we have developed and constructed a simple method of creating THz waves by applying the photo-Dember effect in a (100)-oriented InAs film coated onto the 45° wedged facet of an optical fiber. The charged photocarriers in thin InAs film generate THz waves on the surface of semiconductor due to the difference of the electron and hole diffusion coefficients. Using this alignment-free THz source, we have obtained a bandwidth of 2 THz and sub-wavelength spatial resolution and performed proof-of-principle experiments of THz spectroscopy and near-field imaging. The designed compact THz emission tip can be extended to near-field imaging, spectroscopy, polarization studies, and remote sensing with sub-wavelength resolution.

Also, the contrast of THz image may be significantly increased by an actively shaped THz pulse imaging system which generates adaptively and selectively generated THz pulses via optical pulse shaping technique. Femtosecond pulse shaping techniques have been widely used for electronic and vibrational responses of atoms, molecules, and crystals. Similarly in THz spectral region, selective excitations of phonon modes in a molecular crystal, charge oscillations in semiconductor heterostructures, or phonon-polaritons in a lithium tantalate have been already studied by temporally shaped optical near-infrared pulses. With a great interest, a shaping of THz spectral and spatial profile is required for telecommunication, signal processing, material characterization and control, and functional imaging. In Chapter 6, we explain the optical pulse shaping techniques: acousto-optic modulator and liquid crystal modulator, and phase-only Fourier-domain pulse shaping including the alignment of $4f$ spatial shaper and two phase-only shaping algorithms.

Furthermore, we have shown adaptively shaped THz pulses for spectroscopy and imaging. By using ultrafast optical pulse shaping, adaptively shaped THz pulses with the evaluation of cost function for material spectral response have enabled functional THz spectroscopy and imaging. Spectral phase modulations in a spatial light pulse shaper on Fourier domain produce tailored THz pulses with different sensitiveness. We have acquired THz functional images by elaborately shaped THz pulses. This shaped THz pulse imaging system enhances the contrast of THz image since an intendedly shaped THz pulse has the sensitive attenuation to specific spectrum. This developed spectroscopic and imaging method with designed THz pulses for material spectral response will rapidly enable pulsed THz spectroscopy and imaging without temporal or spectral scanning if direct THz power measurement is used. Finally, the dissertation with discussion and conclusions based on the content of the dissertation will be summarized in Chapter 7.

Chapter 2. Terahertz spectrum and spectroscopy

2.1 Terahertz spectrum

The electromagnetic spectrum is conceptually divided into two broad areas. The radio and microwave frequency regions (≤ 100 GHz) are approached directly with electronics, while the frequencies of infrared radiation and above (≥ 20 THz) are handled by optics and photonics. The frequency range between the microwave and infrared is hardly attainable because the electron mobility is rapidly decreasing towards higher frequencies and because of the absence of semiconductor materials with a wide enough band gap. This frequency range between microwave and infrared wave which spans over frequencies from 0.1 to 10 THz is nominally the THz gap, THz radiation, THz waves, T-rays, or simply THz. The value of frequency of 1 THz can be expressed by various units as follows:

$$1 \text{ THz} \sim 1 \text{ ps} \sim 300 \mu\text{m} \sim 33 \text{ cm}^{-1} \sim 4.14 \text{ meV} \sim 48 \text{ K}. \quad (2.1)$$

Although the first observation of the THz radiation is dated late 1890's [1] according to some reports [2], this THz region has not much interest of researchers for a long time. This delayed development was mainly caused by difficulties in producing reliable and practical sources, as well as by the complexity and low sensitivity of sensors to detect this electromagnetic wave.

During recent few decades, a result of the efforts of many researchers and scientists, advanced techniques in photoconductive switching and optical rectification has been developed [3, 4]. These techniques made it possible to generate THz pulses directly using multimode lasers, Ti:sapphire based lasers, and free-electron lasers. After this added momentum to the field of THz generation and detection, some scientific researches including the extraction of material parameters from terahertz time-domain spectroscopy (THz-TDS) systems have been widely opened. THz research field is applied in many sectors. The photon energy of THz radiation corresponds to the range of fundamental energies associated with changes between molecular energy levels [5], the range of low-energy excitations in electronic materials [6], and vibrational and rotational transitions in molecules [7]. Furthermore THz radiation has been a promising candidate for nondestructive evaluation of the internal structures of targets since THz radiation is transparent to many dry dielectric materials [8, 9]. Hu and Nuss firstly acquired two dimensional THz

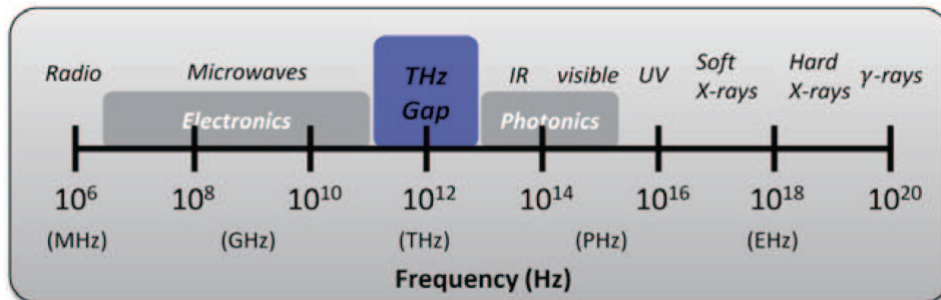


Figure 2.1: The electromagnetic spectrum spanning from microwaves to X-rays. THz frequency region between microwaves and infrared waves spans over frequencies from 0.1 to 10 THz.

images by using a traditional scanned imaging system [10]. This was the beginning of geometric image formation of an object in the THz range. THz pulsed imaging was extended as a novel and promising method, especially applied to medical diagnostics [11].

2.2 Terahertz radiation and spectroscopy

2.2.1 Generation of terahertz electromagnetic waves

All optical-assisted THz techniques have been recognized as an alternative approach to produce and measure THz radiation owing to difficulties in fabricating solid-state THz sources and detectors. Ultrafast charge transport techniques and bulk electrooptic rectification (difference frequency mixing) combined with femtosecond lasers have been exploited. This section will explain how semiconductor structures and electrooptic materials can be used to convert ultrashort pulses into THz pulses.

Photoconductive switching

The first THz emission by a photoconductive switch based on the idea of Hertz original experiment [12] was realized by irradiating a biased semiconductor plate with high-energy argon ions [3]. In a photoconductive switch, a lateral antenna comprising two electrodes deposited onto a semiconductor surface is drawn. A large electric field is applied between the electrodes. An undoped semiconductor material placed under bias is illuminated by ultrashort laser pulses (≤ 100 fs). The photon energy is higher than the band gap energy of the illuminated semiconductor. A photoexcited electron-hole pair created in this process can be well approximated by an elementary Hertzian dipole. The free carriers are accelerated by the applied voltage and rapidly trapped or recombine. This rapid current variation results in the radiation of a pulse perpendicularly to the bias field. The emission bandwidth can be modified by appropriate bands structure design [13, 14].

Optical rectification

Optical rectification is a second-order nonlinear optical process of generating a DC polarization in a nonlinear medium at the passage of an intense optical beam [15]. This method is adapted as one of the most popular technique to generate THz pulses on pulsed laser systems. For ultrashort laser with large bandwidth ($\omega - \Delta\Omega, \omega + \Delta\Omega$), the static polarization is replaced by the pulse envelope, and the various frequency components are differenced with each other to produce a bandwidth from 0 to several THz ($0, 2\Delta\Omega$) [16]. The generated THz field is proportional to the intensity of the incident pump pulse and the value of the second-order susceptibility. This mechanism has been used to generate THz pulses from a number of electrooptic materials such as bulk semiconductors including GaAs, ZnTe, CdTe, GaP, and LiNbO₃ [16, 17, 18, 19, 20]. The organic crystals such as DAST [21] and electro-polymers [22] are also used for THz generation due to a very large electrooptic coefficient. Recently, THz radiation via optical rectification from metal surfaces was reported [23].

Surface emitters

When a bulk semiconductor is illuminated by an ultrafast optical pulse with the photon energy greater than the semiconductor band gap, a surface electric field is built up in the vicinity of the surface. As the difference of mobilities (or diffusion constants) for holes and electrons generates a band bending

which has the effect of accelerating and separating carriers of opposite charges in opposite directions, a charge dipole in the vicinity of a semiconductor surface is formed. This effect is known as surface field emission or a photo-Dember effect [24]. The surface depletion field is vertical to the semiconductor surface. This mechanism of the ultrafast buildup and relaxation of the photo-Dember field results in the generation of THz radiation in narrow band gap semiconductors. The phenomena is particularly strong in high-mobility low-band gap semiconductors such as InAs [25]. The emitted THz radiation is completely transverse-magnetic (TM) polarized waves, caused by the surface depletion field. In this mechanism, the enhancement of THz radiation by a magnetic field was also achieved [26].

2.2.2 Optical sampling of terahertz electromagnetic waves

Optical sampling to probe the electric field of THz radiation can be simply performed by the reverse phenomena of THz emission itself. This optical sampling is ideal for ultrafast and phase-sensitive THz detection. The response times of a room-temperature photoconductive switch and also of an optoelectronic crystal is as short as a fraction of a picosecond or period of THz pulses.

Coherent sampling of terahertz radiation

The detection techniques of coherent THz radiation involve free-space electrooptic and photoconductive sampling. The electrooptic sampling shows good sensitivity and a broad bandwidth, compared to photoconductive sampling. Electrooptic sampling using an optoelectronic crystal can be realized via exploiting the linear electrooptic effect, Pockel's effect. A change of polarization of an ultrashort optical pulse, an electrooptic probe beam is occurred by electric field of radiated THz pulses during only a short time interval. A polarizing beam splitter is used to split the polarization rotation of the probe beam and to achieve intensity modulation of the polarization. A pair of balanced photo-diodes is used to analyze the split polarization rotations. The slow variation in the arrival time of the probe pulse traces a full electric field waveform of radiated THz pulses [27, 28, 29].

Photoconductive sampling is also an optical sampling technique. The antenna detection scheme mostly has a better signal-to-noise ratio than electrooptic sampling. Photoconductive sampling is similar to photoconductive generation. A bias electrical field across the antenna leads is generated by the electric field of radiated THz pulses. The photoconductive antenna directly detects a photocurrent induced by the incident THz electric field. The electric field strength of radiated THz pulse is only sampled for an extremely short time interval of entire THz electric field waveform because the carriers in the semiconductor substrate have an extremely short lifetime.

Synchronous and asynchronous optical sampling

Synchronous optical sampling is an important and conventional sampling method in THz time-domain system. In this system, the electric field of radiated THz pulse is recorded in the time domain via different delay time. The varied time delay is achieved by several mechanical approaches: (i) traditional motorized scanning stage (ii) raster mechanical scanning devices. Synchronous sampling have to timely match between each acquired THz waveform and optical gating pulse for optical sampling.

Asynchronous optical sampling (ASOPS) is a technique for high resolution and fast measurements of time-domain spectroscopy [30, 31, 32]. This sampling technique needs two different mode-locked lasers with a slight difference in pulse repetition rates. The two different pulses automatically provide a

temporally varying delay. The scan rate is determined by the difference of repetition rates between two laser system.

2.2.3 Terahertz time-domain spectroscopy

In 1980's, THz time-domain spectroscopy (THz-TDS) was developed and had been pursued in a couple of laboratories [33, 34]. THz-TDS is a phase-sensitive measurement. This is an important advantage over the FTIR spectroscopy where the information about the phase change is not measurable. The technique is much faster for broadband detection than scanning a narrow-band tunable THz source. THz-TDS uses single-cycle pulses of broadband THz radiation generated by ultrashort laser pulses. Because of the ability to read out both amplitude and phase change of full THz electric field, a table-top THz-TDS is the most useful and versatile for comprehensive material research, and it eliminates many disadvantages of tunable narrow-band and large facilities. This versatility and efficiency of THz-TDS caused a boom of THz experiments. The principle of conventional THz-TDS based on the femtosecond laser system is that pump pulses are incident on a THz emitter to generate THz pulses, which are guided into the THz sampler by using four off-axis parabolic mirrors. Probe pulses from the same laser are used to optically sample the THz pulses incident upon a THz sampler.

Chapter 3. Sub-wavelength THz pulse radiation and imaging

3.1 Introduction

In this chapter, the basic mechanisms of THz generation from semiconductor surfaces and some near-field techniques to overcome diffraction of THz pulses are described. Ultrashort electromagnetic radiation with THz region can be generated from illuminated semiconductor surfaces by femtosecond laser pulses. The current research of THz radiation from a variety of semiconductors as well as the emission mechanism have been studied. It is commonly understood that the radiation of THz pulses from semiconductor surfaces is primarily due to the surge current normal to the surface and/or the second-order nonlinear optical processes in the semiconductors. It is shown that the surface of InAs is an efficient THz emitter and that the efficiency is further enhanced by applying an external magnetic field [26, 35, 36]. THz radiation method on the surface of InAs has attracted much interest because of the potential as a simple and powerful THz radiation source in practical applications such as spectroscopy and imaging. In addition, THz imaging offers many attractive advantages for applications in material characterization, microelectronics, medical diagnosis, environmental control, and chemical and biological identification. With a comparatively longer wavelength ($300 \mu\text{m} = 1 \text{ THz}$), Rayleigh's criterion limits its use for imaging of single cells and other microstructures. Typical human cell sizes range from a few to hundreds of microns. A method for breaking the Rayleigh's criterion and thus achieving sub-wavelength resolution is to adopt near-field imaging techniques.

3.2 Terahertz pulses generation from semiconductor surfaces

The physical principles for THz generation from semiconductor surfaces can be categorized into two types. One is the nonlinear optical processes and the other is the ultrafast surface surge-current with carrier excitation due to the surface built-in field or photo-Dember effect. Generated THz radiation via the nonlinear optical process is explained as the optical rectification of ultrashort laser pulses, which creates a transient polarization on the semiconductor surface. The generated THz pulse is proportional to the second time derivative of the electronic polarization due to the optical rectification. This process is equivalently described in the frequency domain as the difference-frequency mixing between spectrum components of femtosecond laser pulse. On the other hand, the surge-current model is closely related to real excitation carrier. There are two origins for radiated THz waves via photoexcited carrier from semiconductor surfaces. One is the acceleration of photoexcited carriers by the surface-depletion field, and the other is the photo-Dember effect originating from a charge dipole in the vicinity of a semiconductor surface. The dipole forms owing to the difference of mobilities for holes and electrons. Because electrons have much greater diffusion velocity due to their higher mobility than that of holes, electrons diffuse more rapidly from the surface inwardly, which creates an effective charge separation in the direction perpendicular to the surface. For the explanation of the mechanisms of THz radiation from semiconductor surfaces, several representative semiconductors are listed in Table 3.1 with their basic properties and some

Table 3.1: Properties of selected semiconductor materials

	InAs	GaAs	InSb	InP
Band gap (eV)	0.354	1.43	0.17	1.344
Electron mobility ($cm^2/(Vs)$)	$\leq 40,000$	$\leq 8,500$	$\leq 77,000$	$\leq 5,400$
Hole mobility ($cm^2/(Vs)$)	≤ 500	≤ 400	≤ 850	≤ 200
Γ valley electron mass m_e^*	0.023	0.063	0.014	0.08
Hole mass m_h^*	0.33	0.5	0.18	0.40
Intrinsic carrier concen. (cm^{-3})	10^{15}	2.1×10^6	2×10^{16}	1.3×10^7
Infrared refractive index	3.5	3.3	4.0	3.1
Refractive index (@1THz)	3.7	3.6	1.9	3.5
Optical penetration depth (μm)	0.15	1	0.1	0.3

important parameters [37, 38].

3.2.1 Optical rectification

The emission mechanism of THz radiation from semiconductor surfaces via nonlinear optical process is an effective $\chi^{(2)}$ process. Many semiconductors without the inversion crystal symmetry, such as the zincblende-type semiconductors, have been reported to radiate THz waves via optical rectification effect [17, 39]. The generated THz field by the optical rectification, $E_{THz}(t)$, is proportional to the second-order nonlinear polarization and can be described by the following equations:

$$P(t) = \frac{1}{2\pi} \int_{-\infty}^{+\infty} P^{(2)}(\Omega) e^{-i\Omega t} d\Omega, \quad (3.1)$$

$$P_i^{(2)}(\Omega) = \sum_{j,k} \varepsilon_0 \chi_{ijk}^{(2)}(\Omega = \omega_1 - \omega_2) \int_{-\infty}^{+\infty} E_j(\omega_1 = \Omega + \omega_2) E_k(\omega_2) d\omega_2, \quad (3.2)$$

where $\chi_{ijk}^{(2)}$ is the second-order nonlinear susceptibility tensor for a difference frequency, $\Omega = \omega_1 - \omega_2$, and $E_j(\omega_1)(E_k(\omega_2))$ is the amplitude spectral component of the pump laser at frequency $\omega_1(\omega_2)$ in the $j(k)$ direction. Here, i, j , and k are the dummy indexes for x -, y -, and z -directions in the crystallographic axis system. The integral is extended to the negative frequency by using the definition, $E(-\omega) = E^*(\omega)$.

In the far-field, the measured THz field amplitude, E_{THz} , is proportional to the projection of the second time derivative of the nonlinear polarization to the polarization direction of detection:

$$E_{THz}(t) = \hat{u} \cdot \mathbf{E}_{THz} \propto \hat{u} \cdot \frac{\partial^2 \mathbf{P}(t)}{\partial t^2}. \quad (3.3)$$

The spectral amplitude, $E_{THz}(\Omega)$, at a frequency Ω is thus given by

$$E_{THz}(\Omega) \propto \Omega^2 \hat{u} \cdot \mathbf{P}(\Omega). \quad (3.4)$$

The strong dependence of emitted THz radiation intensity on the crystal orientation to the pump beam polarization is the evidence of the contribution of $\chi^{(2)}$ process. By rotating a THz emission crystal about its surface normal, the azimuthal-angle dependency of difference frequency mixing component to the total THz radiation can be expected.

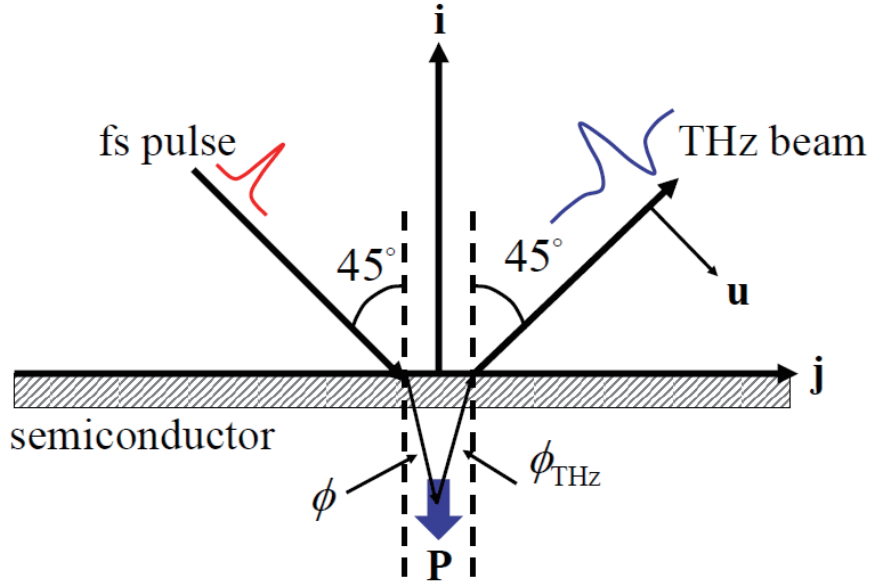


Figure 3.1: Optical geometry for generation of THz radiation from a semiconductor surface.

When the p -polarized THz field amplitude is observed in the direction of optical reflection, the refraction angles for the optical and THz beams are determined by the generalized Snell's law as

$$\sin 45^\circ = n_{opt} \sin \phi = n_{THz} \sin \phi_{THz}, \quad (3.5)$$

where n_{opt} and n_{THz} is the refractive index for the pump laser and THz radiation in the semiconductor, respectively. ϕ_{THz} is the refraction angle of THz radiation inside the semiconductor (see Fig. 3.1). For above condition, the azimuthal-angle dependence of the radiation amplitude due to the optical rectification can be easily written as [40]

$$\begin{aligned} E_{THz} &\propto 1.093d_{14}(\cos 3\theta - 0.103) \text{ for } (111) - \text{InAs}, \\ E_{THz} &\propto 0.1823d_{14}\sin 2\theta \text{ for } (100) - \text{InAs}, \\ E_{THz} &\propto -0.069d_{14}\sin 2\theta \text{ for } (100) - \text{InSb}, \\ E_{THz} &\propto 0.199d_{14}\sin 2\theta \text{ for } (100) - \text{InP}. \end{aligned} \quad (3.6)$$

We can manipulate a proper azimuthal angle, where the nonlinear contribution vanishes. For an azimuthal angle of 26° for (111)-InAs and 0° (or 90°) for all (100)-oriented samples, the azimuthal dependency is null [40].

3.2.2 Surface depletion field

In semiconductors with a wide band gap, such as GaAs ($E_g = 1.43$ eV) or InP ($E_g = 1.34$ eV), Fermi-level pinning occurs, leading to band bending and formation of a depletion region, which results in the surface built-in field [41, 42]. When femtosecond pulses are illuminated on the surface of semiconductor, the electrons and holes are accelerated in opposite directions under the surface-depletion field, forming a surge current in the direction normal to the surface. The direction and magnitude of the surface depletion field depend on the dopant or impurity species. The energy band is bending upward in n -type semiconductors and downward in p -type semiconductors as shown in Fig. 3.2.

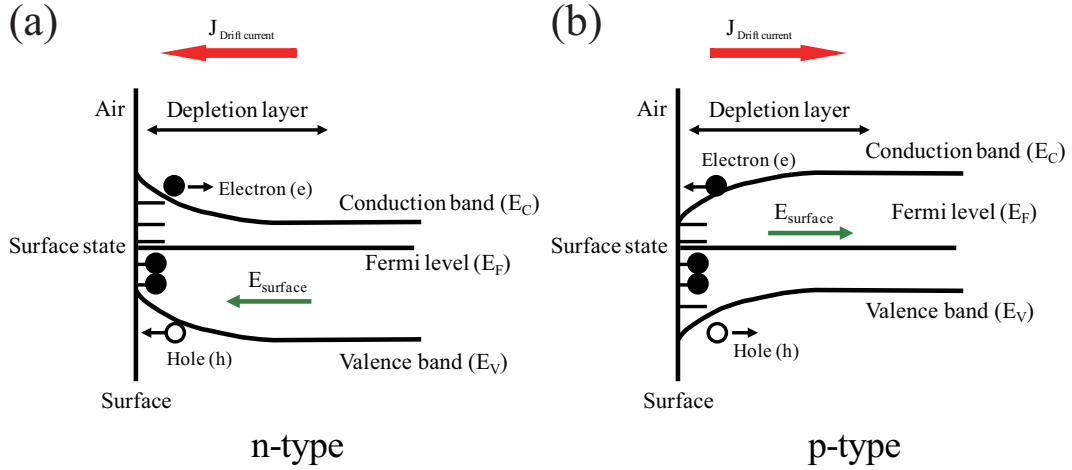


Figure 3.2: Band diagram and the schematic flow of drift current in (a) n -type and (b) p -type semiconductors

The radiated THz amplitude, $E_{THz}(t)$, is proportional to the time derivative of the surge current, $J(t)$: $E_{THz}(t) \propto \partial J(t)/\partial t$. When the depletion-surface field is the dominant mechanism for the surge current, the polarity of radiated THz waveform is opposite between that of the n -type and that of the p -type semiconductors. On the other hand, when the photo-Dember effect is the dominant mechanism, the polarity of radiated THz amplitude will be independent to the type of semiconductor.

3.2.3 Photo-Dember effect

InAs and InSb are very interesting semiconductors because of their high electron mobilities to generate THz electromagnetic waves. The surface-depletion voltage of narrow band gap semiconductors is generally not so large because of the small band gap energy while the excess energy of photoexcited carriers is very large with the excitation femtosecond pulses ($h\nu \sim 1.5$ eV). All these conditions in narrow band gap semiconductors enhance the photo-Dember effect, which generates current or voltage in semiconductors due to the difference of the electron and hole diffusion velocities. The diffusion current due to the photo-Dember effect near photoexcited semiconductor surface is illustrated in Fig. 3.3.

The diffusive currents of the electrons (J_n) and holes (J_p) are, respectively, described by the following equations [43],

$$J_n \sim -eD_e \frac{\partial \Delta n}{\partial x}, \quad J_p \sim eD_h \frac{\partial \Delta p}{\partial x}, \quad (3.7)$$

where e is the electron unit charge, Δn and Δp the density of photoexcited electrons and holes, D_e and D_h the diffusion coefficient of electrons and holes, respectively. The diffusion coefficient D is defined by the Einstein relation, $D = k_B T \mu / e$, where k_B is the Boltzmann constant, T is the temperature of photoexcited carrier, and μ is the mobility of electrons or holes. Radiated THz amplitude due to photo-Dember current $J_{diff} = J_n + J_p$ is thus proportional to the difference in the mobility and temperature for the electrons and holes, and the gradient of the carrier density. We discuss the equation of the steady-state photo-Dember voltage (V_D) [44],

$$V_D = \frac{k_B(T_e b - T_h)}{e} \frac{1}{b+1} \ln \left(1 + \frac{(b+1)\Delta n}{n_0 b + p_0} \right), \quad (3.8)$$

Here, $b = \mu_e / \mu_h$ is the mobility ratio of the electrons (μ_e) and holes (μ_h), n_0 and p_0 are the initial density of the electrons and holes, T_e and T_h are the temperature of photoexcited electrons and holes, respectively.

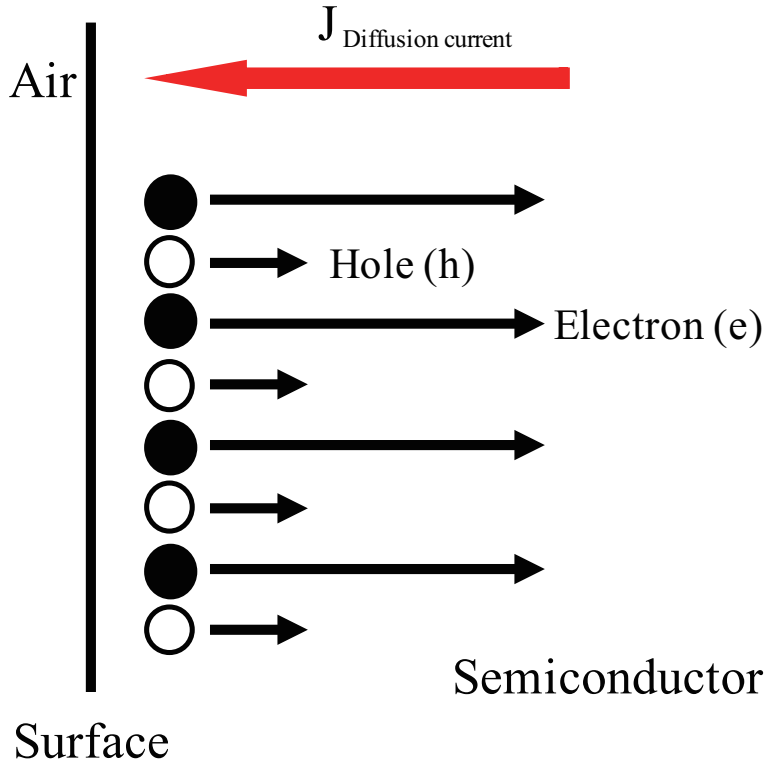


Figure 3.3: Schematic diagram of diffusion current by photoexcited carriers near the surface of a semiconductor

The photo-Dember effect is enhanced by larger electron mobility ($\mu_e \propto b$), and higher electron excess energy ($\propto T_e$). The narrow band gap semiconductor is good to generate a huge photo-Dember field due to the very large electron mobilities and large excess carrier energies. The photo-Dember field, E_D (V_D/d , d : the optical penetration depth) in narrow band gap semiconductors is also further enhanced by the small absorption depth. From (3.8), we can anticipate that some important properties affect the emission of THz pulse via photo-Dember effect. First, low residual electron and hole concentrations (n_0 and p_0) enhance the photo-Dember effect and the photo-Dember voltage, V_D is expected to be proportional to the pump intensity, I , ($V_D \propto \Delta n \propto I$) in a low-intensity regime and proportional to $\ln(I)$ [$\propto \ln(\Delta n)$] in a high-intensity regime. Also, the photo-Dember voltage does not depend strongly on the electron-hole mobility ratio when b is large enough. Consequently, the emitted THz field amplitude is proportional to the acceleration field and electron mobility ($E_{THz} \propto \Delta J \propto e\mu_e E_D$).

3.3 Terahertz near-field imaging

Far infrared imaging was already performed by using a cw far infrared waveguide laser [45]. The image shows a contrast of a hidden metal key revealed behind an obstacle paper box. After the THz radiation and detection via a photoconductive switch by Auston et al., the research of THz radiation has been widely opened. Shortly after, the same group introduced pulsed THz image in the focal plane [10]. The THz pulsed imaging has attracted much interest since its first demonstration and has gained importance as a promising tool for various basic research and industrial applications. It has been increasingly used in a variety of areas such as non-invasive packaging inspection, material

inspection in industrial production, biomedical diagnostics and imaging, 3D-computed tomography, and scientific phenomena including the distribution of electromagnetic waves and phase transition. Most THz imaging have been accomplished using conventional THz-TDS focal plane imaging in far-field region. In conventional focal plane imaging, the spatial resolution is limited by the wavelength radiated THz pulses or by the size of an aperture, whereby the intensity of radiated THz pulse significantly reduces. Many more or less successful attempts have been invented and applied to increase the spatial resolution in the THz imaging.

3.3.1 The far-field and near-field spatial region

The far-field region

The far-field region is also known as far-field, or Fraunhofer diffraction region and it is the region outside the near-field region, where the angular field distribution is essentially independent of the distance from the source. In the far-field region, the shape of the antenna pattern is independent of distance. If the source or aperture has an overall dimension that is large compared to the wavelength, the far-field region is commonly assumed to exist the Fresnel number smaller than an unity ($F \ll 1$). The Fresnel number F is defined as

$$F = a^2/L\lambda, \quad (3.9)$$

where a is the characteristic size of the aperture, L is the distance of the screen from the aperture, and λ is the incident wavelength. The propagation of THz radiation in the far-field region can be sufficiently described by the propagation of a Gaussian beam.

The near-field region

The near-field region is also known as near-field, or Fresnel diffraction region and it is in general the close in region of an antenna where the angular field distribution is strongly dependent upon the distance from the antenna. In the study of diffraction and antenna design, the near-field is that part of the radiated field of the source or the antenna, which exists the Fresnel number similar or greater than an unity ($F \geq 1$). The diffraction pattern in the near-field differs significantly from that observed at infinity and varies with distance from the source, and non propagation of electromagnetic wave, so-called evanescent wave is present.

3.3.2 Review of the methods for terahertz near-field imaging

The near-field effect at THz frequencies was reported by Budiarto et al. on a diffraction behind an aperture [46] and the first near-field imaging was obtained by using tip-enhanced near-field technique [47]. Several other methods were developed during the following decade, mainly by transmigrating near-field methods already used in other frequency regions, either in optics [48] or in microwave [49]. Currently, various near-field techniques and approaches have been applied successfully, the majority of these are described below.

Small Aperture near-field methods

Small aperture-based near-field techniques use a small aperture on the top of the sample to enhance the spatial resolution. On Babinet's principle, the diffraction pattern should be the same from a tip and from a hole of the same diameter size except for the overall forward beam intensity. And, the power of

the useful signal is dependent on the size of the opening and is strongly attenuated [50]. Even though it's the significant power reduction, some THz near-field experiments were realized by using a small aperture [51, 52].

Confinement methods

Confinement near-field methods are such techniques in which the light is constrained into a small volume by a waveguide structure. Most of the waveguide structures are of transmission-line or waveguide types. Originally developed for IR waveguides [53], it was first experimentally demonstrated using a tapered metal tube for THz region [47]. For a symmetrical cross-section structure, a waveguide shows a strong frequency cut-off behavior. To eliminate the low-frequency cut-off of a constraining waveguide, variety methods were attempted.

A conical aperture [54] and a logarithmic coupling structure [55] were introduced. So, the field confinement at the structure opening is enhanced, coupling is also more efficient. An open-side pyramidal-shaped dielectric probe also was shown to eliminate the cut-off frequency in microwave region [56]. A spatial resolution of at 80 GHz was achieved by a metal-dielectric probe [57]. Also, the sub-wavelength resolution was realized by a narrow spacing in a parallel-plate waveguide [58] and by a photoconductive near-field probe-tip consisting from two tapered electrodes, which is a confinement structure in plane [59].

Sub-wavelength dimensional tip methods

Tip-enhanced (or scattering-type) near-field methods are frequently adapted methods to achieve sub-wavelength resolution in any frequency range. A sharp metallic tip is positioned close to the sample surface into the place irradiated by radiation. A near-field is created at the end of the probe tip during the propagation of the pulse. It is affected by the sample characteristics and is again coupled into the far-field radiation. This method reflects a small changed portion of the field from the very vicinity of the probe. Only a small part of the incident light can be used to retrieve the near-field information. The probe-sample interaction may be non-trivial in the time-domain regime and was recently the subject of other studies. A near-field probe made of tungsten was used [60] and metal-dielectric and doped dielectric contrast were measured [61, 62].

This technique was improved to enhance the spatial resolution and image contrast by a shear force technique [63]. An imaging tip can be as small as possible. Atomic force microscopy (AFM) tips have been irradiated by THz radiation and spatial resolution down to tens of nm was demonstrated [64]. Other method, the concept of Sommerfeld-wire waveguide method, can be transformed into the tip-enhanced type. THz radiation travels along the surface of the metallic tip back-and-forth with a reflection on the sample surface at the end of the probe where near-field phenomena appear [65]. A combined method with the vibrating probe has the potentiality for pulsed THz sensing and diagnostic systems with unreported resolution [66]. Also, THz-ANSOM is a complex result of combining the tip-enhanced method with the laser-beam involved imaging. The THz near-field in close vicinity of a metallic tip is sampled on electrooptic sensor just behind a thin sample. All electric field component of the near-field around a metallic disturbance was measured [67].

A focused optical laser beam near-field methods

An alternative apertureless THz near-field method achieves sub-wavelength resolution by exploiting the fact that the THz emission or detection point is smaller than the THz wavelength. This can be realized by placing the sample close to the emitter or sensor, so that the radiation would not have time to diffract forward far-field region. We can easily create and measure the near-field by focusing and manipulating the optical laser beam which generate and sample THz pulses. In those technique, reducing the shape and choosing the right placement of the laser-beam spot is playing the biggest role. One example is THz wave generated through optical rectification process, where size of THz wave emitter is limited by spot size of the excitation optical beam in the electrooptic crystal [68, 69]. To get higher spatial resolution, one need to focus the excitation laser beam to smaller focal spot size and use thinner THz emitter. An alternative way is the THz generation with optical excitation from the target itself, such as semiconductor devices. THz wave emission microscopy images of IC circuits were obtained [70]. Sub-wavelength spatial resolution can also be obtained by a localized THz wave on electrooptic sensor detector [71]. Similar to a localized THz wave emission method, focused probe beam with sub-THz wavelength size forms a localized THz wave detector by placing the target within near-field distance. The spatial resolution was determined by the size of THz wave detector.

3.4 Sub-wavelength THz radiation from thin InAs film

Here before, some techniques of THz radiation from semiconductor and the method to overcome diffraction limit of THz pulses are explained. Some THz emission microscope have explored to get sub-wavelength resolution of THz pulses. THz emission microscope system has been studied because this can be easily realized by placing the sample close to the emitter and the size of radiated THz pulse is limited by spot size of the excitation optical beam. To get higher spatial resolution, one need to focus the excitation laser beam to smaller focal spot size and use thinner THz emitter. The coherence length and the thickness of nonlinear crystal are crucial parameters for THz emission via optical rectification. Generally, thinner nonlinear crystal results in lower signal, which may be not enough to THz spectroscopy and imaging. However, the diffusion length of InAs for THz radiation is only about $1 \mu\text{m}$. An alternative way using thin InAs film instead of nonlinear crystal such as ZnTe is good for THz wave emission microscopy.

3.4.1 MBE-grown thin InAs fabrication

The excitation of InAs with 800-nm femtosecond pulses provides desirable conditions for the photo-Dember effect: (i) large spatial gradient of carrier density due to the short absorption depth, (ii) large kinetic energy of photoexcited carriers are obtained from the large excess energy ($\Delta E = E_{opt} - E_g, \sim 1.2 \text{ eV}$), and (iii) large difference between the electron and hole mobilities. By using the intrinsic mobility of InAs [$40,000 \text{ cm}^2/(\text{V} \cdot \text{s})$] and the excess energy during excitation ($\sim 1.2 \text{ eV}$) at room temperature, the diffusion constant from the Einstein Relation is computed to be $\sim 3.6 \text{ m}^2/\text{s}$. Using this value and the average scattering time (momentum relaxation time of $\sim 0.5 \text{ ps}$), the diffusion length is estimated to be $1.3 \mu\text{m}$. Considering effective Dember charge separation, the $1\text{-}\mu\text{m}$ thickness of InAs is enough to generate THz pulses via photo-Dember effect. This thickness is good for the sub-wavelength THz emission microscope because there is no significant diffraction of radiated THz pulses on the surface of semiconductor.

Figure 3.4 shows the spatio-temporal distribution of photoexcited carriers within 1-ps time evolution and within the depth of $1 \mu\text{m}$ under the surface of InAs. The gray grid and dark grid represents the photoexcited electron and hole distribution, respectively. After femtosecond pulses are illuminated, the number of photogenerated electrons and holes increases drastically with an exponential decrease spatially.

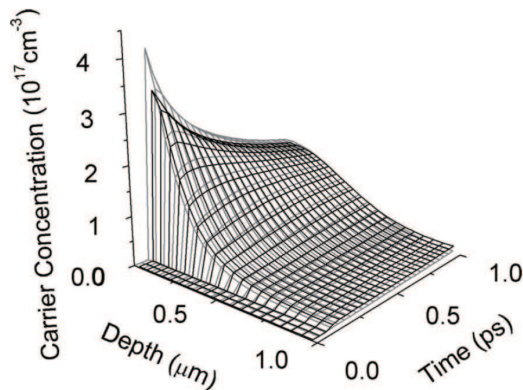


Figure 3.4: A three-dimensional spatial and temporal carrier concentration distribution of photoexcited electrons and holes at the InAs surface. The gray curves represent electron distribution and the dark curves represent the hole distribution [25].

Then, due to the large gradient of the carrier distribution, these carriers diffuse inward the InAs. The concentration of electrons near the surface drops down faster than that of holes since the mobility of the electrons is much higher than that of the holes. The subsequent spatial difference of the electron and hole distribution generates photo-Dember electric field, E_D . This field causes the drift of electron and holes toward each other. The sudden rising of the photoexcited electrons and their movement afterwards could result in THz wave radiation. The electric field of the THz wave is given by $E_{THz} \propto \partial J / \partial t$, where J is the current induced from the photoinduced electrons and holes.

To study the optically induced electromagnetic radiation from semiconductors, we simply assume the dipole approximation. This assumption is valid because when the carrier's velocity is much less than the velocity of light, the dipole approximation is the simplest model to estimate the radiation and gives a qualitative description for the radiation phenomena. The electric and magnetic components \mathbf{E} and \mathbf{B} from a charged particle in the expression of dipole radiation can be written as

$$\mathbf{E} = (e\mathbf{r}/4\pi\kappa c^2 r^3) + (e/4\pi\kappa c^2 r^3)\mathbf{r} \times (\mathbf{r} \times \dot{\mathbf{v}}), \quad (3.10)$$

$$\mathbf{B} = e(\dot{\mathbf{v}} \times \mathbf{r})/4\pi\kappa c^2 r^2, \quad (3.11)$$

where r is the distance from the charged particle to the observation position, κ is the dielectric constant, c is the speed of the light, and $\dot{\mathbf{v}}$ is the acceleration of the particle. The first term in the \mathbf{E} expression is a Coulomb field; it decreases as r^2 and can be ignored at far-field. The second term is the radiated field with TM wave. Using the equation of the current $\mathbf{J} = e\mathbf{v}$, where \mathbf{v} is the charge velocity, the radiation term can be rewritten as

$$\mathbf{E}_\theta = (\sin \theta / 4\pi\kappa c^2 r) \dot{\mathbf{J}} \hat{e}_\theta, \quad (3.12)$$

where θ is the angle between the observation direction and particle acceleration direction.

The amplitude of the radiated field from semiconductors strongly depends on the optical incident angle. The angular dependent radiated field (forward) as a function of the incident angle has the following form:

$$E(\theta) \propto \sin(\theta)[1 - r^2(\theta)]t(\theta). \quad (3.13)$$

The first term comes from the radiation pattern of the dipole approximation, the second term from the photocarrier density which is proportional to the optical absorption, and the third term from the transmission coefficient of the electromagnetic wave. For p -polarized and s -polarized optical beam denoted “ \parallel ” and “ \perp ”, Fresnel coefficients are written as

$$\begin{aligned} r_{\parallel} &= \frac{\tan(\theta - \theta_t)}{\tan(\theta + \theta_t)}, \\ r_{\perp} &= \frac{\sin(\theta - \theta_t)}{\sin(\theta + \theta_t)}, \\ t_{\parallel} &= \frac{2 \cos \theta \sin \theta_t}{\sin(\theta + \theta_t) \cos(\theta - \theta_t)}, \\ t_{\perp} &= \frac{2 \cos \theta \sin \theta_t}{\sin(\theta + \theta_t)}, \end{aligned} \quad (3.14)$$

where $\theta_t = \sin^{-1}[\sin(\theta)/n_2]$ with n_2 the index of refraction of the radiated field. The maximum radiation direction is close to the Brewster angle. Figure 3.4.1 shows the angular dependent radiation TM THz power (circle) from thin InAs film for p -polarized optical excitation beam and calculated TM radiation field for p -polarized (red) and s -polarized (black) optical beam.

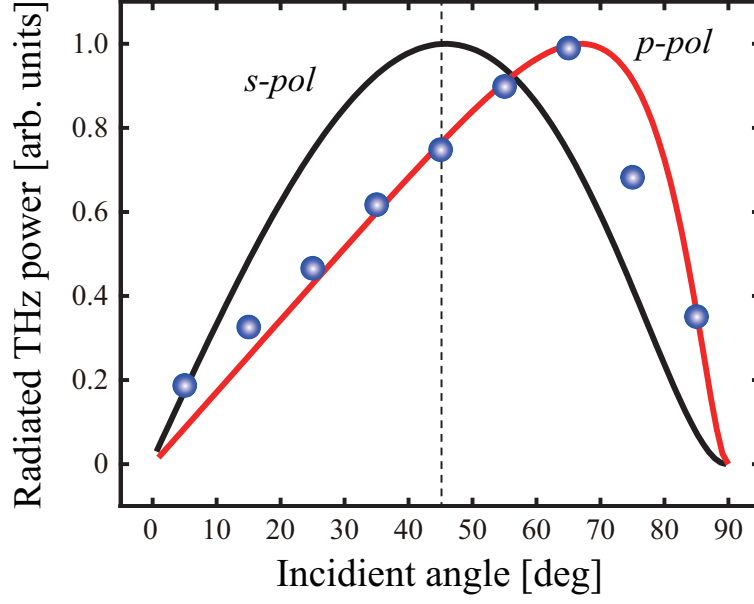


Figure 3.5: The incident angular dependence of radiated TM-THz power (circle) from thin InAs film for p -polarized optical excitation beam and calculated TM radiation field for p -polarized (red) and s -polarized (black) optical beam.

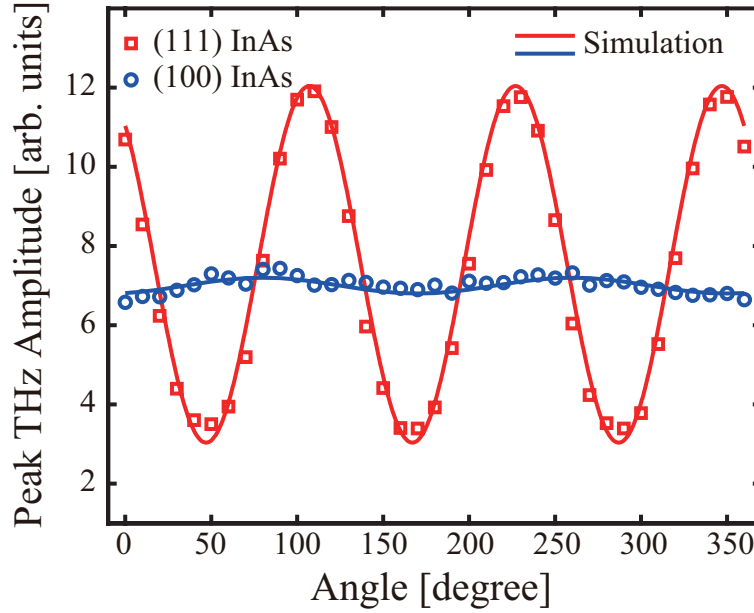


Figure 3.6: The azimuthal dependence of THz wave generation from differently-oriented InAs surfaces. The squares and circles represent the experimental measurements of THz wave amplitude from a (111) oriented n -type InAs with a doping concentration at $3 \times 10^{16} \text{cm}^{-3}$ and a (100) oriented p -type InAs with a doping concentration at $1 \times 10^{18} \text{cm}^{-3}$, respectively. The curves represent the fitting results by cosine equations.

Figure 3.6 shows the azimuthal dependence of THz wave radiation from a (100) *p*-type and (111) *n*-type InAs at a 45° incident angle. The dots and squares show the experimental data and the lines fit the experimental data with a cosine function. Both samples show azimuthally angle-dependent THz wave amplitude, which could be evaluated with $E_{\text{peak}} = E_{\text{Dember}} + E_{\text{opt rectification}} \cdot \cos(\omega\theta)$. It is clear to see that both the samples have an E_{Dember} component with nearly the same value due to the photo-Dember effect. The $E_{\text{opt rectification}} \cos(\omega\theta)$ is quite different between these two samples. The azimuthal dependence of THz radiation in (111) InAs is obvious with a period of $\pi/3$; while a (100) InAs has a slight azimuthal dependence with a period of $\pi/2$.

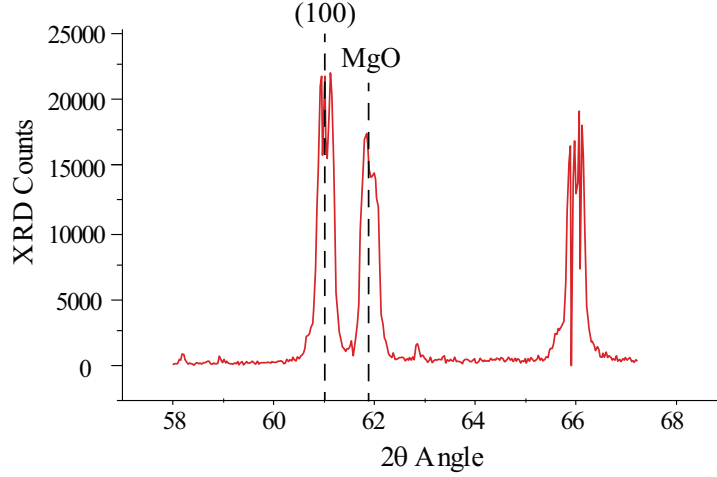


Figure 3.7: The result of X-ray Diffraction for MBE-grown (100) InAs film on MgO substrate.

Here, we manipulate a proper azimuthal angle, where the nonlinear contribution vanishes. The (100) crystal axis is chosen. The azimuthal dependency is almost null for all (100)-oriented samples. The 1- μm -thick (100) InAs thin film was grown by molecular beam epitaxy (MBE) on an AlAsSb buffered GaAs substrate. The thickness was optimized by considering effective Dember charge separation and absorption and resolution of THz pulses. Also, X-ray Diffraction are executed to check crystal axis of MBE-grown InAs film. The grown InAs sample was glued to a sapphire substrate and then the substrate and buffer layer were eliminated by lapping and chemical etching by phosphoric acid solution ($\text{H}_3\text{PO}_4 : \text{H}_2\text{O}_2 : \text{H}_2\text{O} = 1 : 8 : 80$, 1.3 $\mu\text{m}/\text{min}$ or $\text{H}_3\text{PO}_4 : \text{H}_2\text{O}_2 : \text{H}_2\text{O} = 1 : 1 : 5$, 1.2 $\mu\text{m}/\text{min}$).

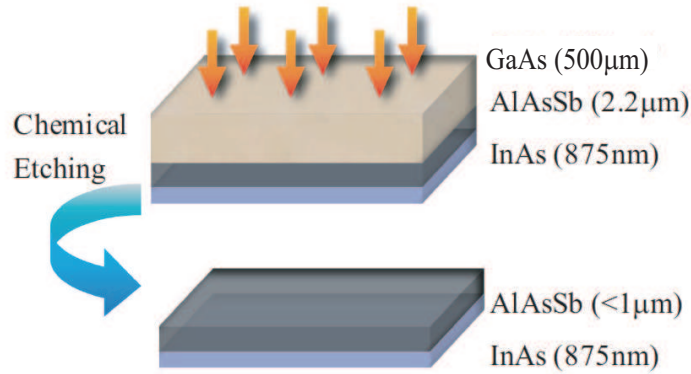


Figure 3.8: 1- μm -thick InAs thin film fabrication layout.

3.4.2 The resolution of THz pulse from thin InAs film

We construct a sub-wavelength THz emission microscope by using thin InAs film attached on the surface of sapphire wafer. For an experimental verification, we develop sub-wavelength THz emission microscope as shown in Fig. 3.9. The figure shows layout and schematic diagram of transmissive sub-wavelength THz emission microscope. Femtosecond Ti:sapphire optical laser system has used to generate THz pulses via the photo-Dember effect transmissively from a low band gap InAs film [74]. The THz pulses radiated from the InAs thin film were detected by a conventional photoconductive antenna (PCA) in conventional $4f$ imaging geometry with two off-axis parabolic mirror [75].

Typically measured temporal THz pulses and its spectrum up to 2 THz are shown Fig. 3.10. For sub-wavelength THz emission apertures, optical laser pulses are tightly focused by an objective lens with $f = 16.5$ mm. Focused beam waist is roughly $3.6 \mu\text{m}$. To check the resolution of radiated THz pulse, we have carried out knife-edge experiment. Measured THz-peak image of knife-edge method with half filled InAs film are illustrated. THz peak signal is detected at fixed temporal position. The edge response is how the system responds to a sharp straight discontinuity (an edge). The single parameter measurement used here is the distance required for the edge response to rise from 10% to 90%. The spatial resolution of the THz peak image is measured about $10 \mu\text{m}$ by the 10% - 90% method ($X_{10-90} = 2 \times 0.64w_x = 14 \mu\text{m}$).

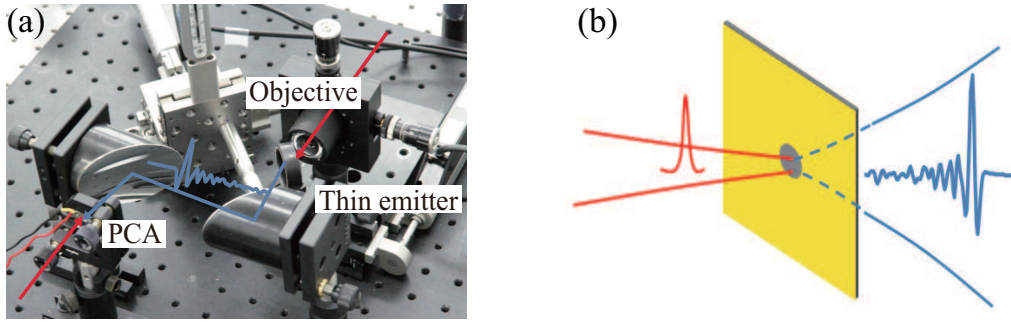


Figure 3.9: (a) Layout and (b) schematic diagram of transmissive sub-wavelength THz emission microscope.

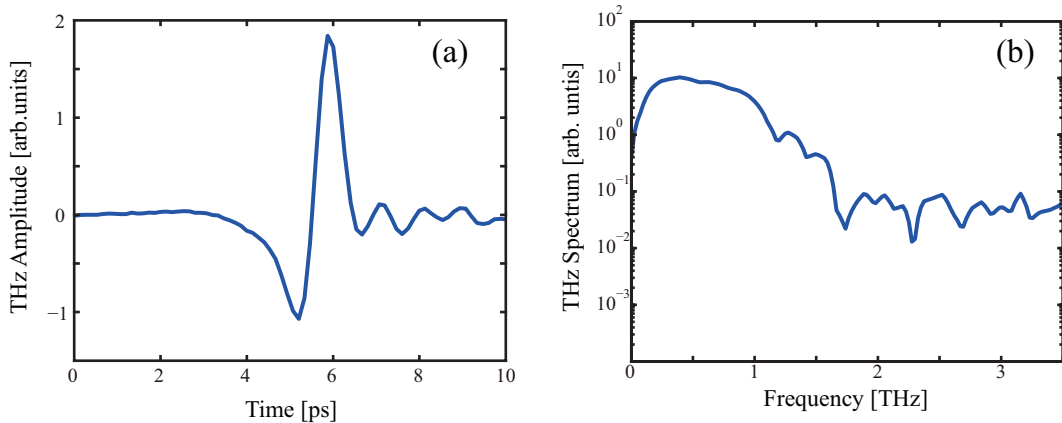


Figure 3.10: Measured temporal THz pulses and its spectrum up to 2 THz from sub-wavelength THz emission microscope with 1- μm -thick InAs film.

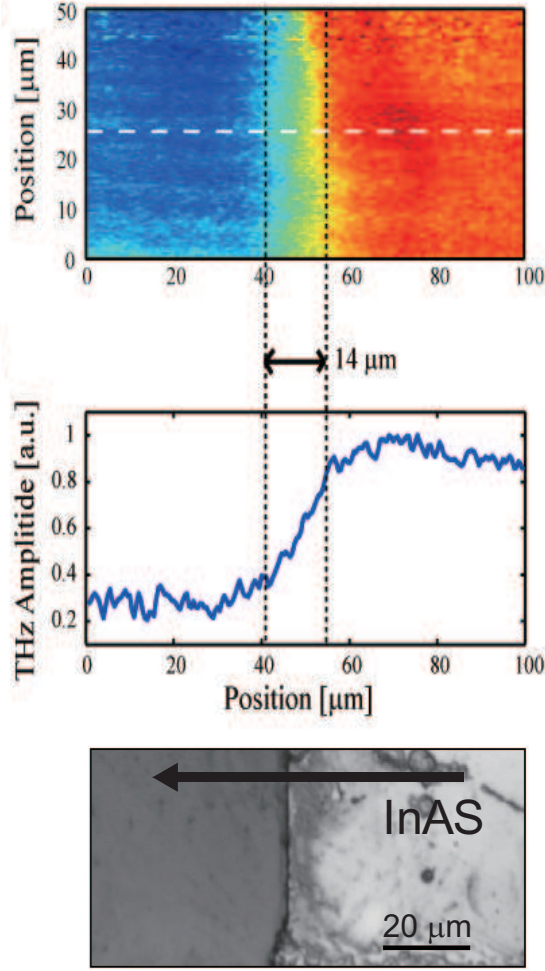


Figure 3.11: Measured THz-peak image of knife-edge experiment using half filled InAs film at fixed temporal position. The spatial resolution of the THz-peak image is measured about $10 \mu\text{m}$ by the 10% - 90% method ($X_{10-90} = 2 \times 0.64w_x = 14 \mu\text{m}$).

The $10\text{-}\mu\text{m}$ beam waist of radiated THz pulses on the surface of thin InAs film is about $\lambda_0/30$ ($\lambda_0 = 300 \mu\text{m}$, $300 \mu\text{m} = 1 \text{ THz}$). We have obtained highly focused THz pulses to resolve small object relatively smaller than the diffraction of THz pulse for near-field geometry. Next, Figure 3.12 shows the THz image of single mode optical fiber with $125\text{-}\mu\text{m}$ -diameter cladding, HP780 Nufern. Cladding diameter is slightly smaller than $\lambda_0/2$. As shown the figure, we can clearly recognize the cladding region of optical fiber. However, transmissive THz emission microscope do not resolve the core of optical fiber with $5.5 \mu\text{m}$, which is smaller than the resolution of developed THz microscope.

Let us check the resolution of each THz frequency components, we have measured THz temporal signal as a function of different spatial position scanning half-filled InAs film for edge response experiment. Each THz frequency components can be easily obtained by Fast Fourier Transform (FFT) of temporal THz profiles. Measured THz temporal shapes and their spectra are shown in Fig. 3.13. Gaussian beams propagating in the z -direction may be represented mathematically as:

$$E(r, z) = E_0 \frac{w_0}{w(z)} \exp\left(\frac{-r^2}{w^2(z)}\right) \exp\left(-ikz - ik\frac{r^2}{2R(z)} + i\zeta(z)\right). \quad (3.15)$$

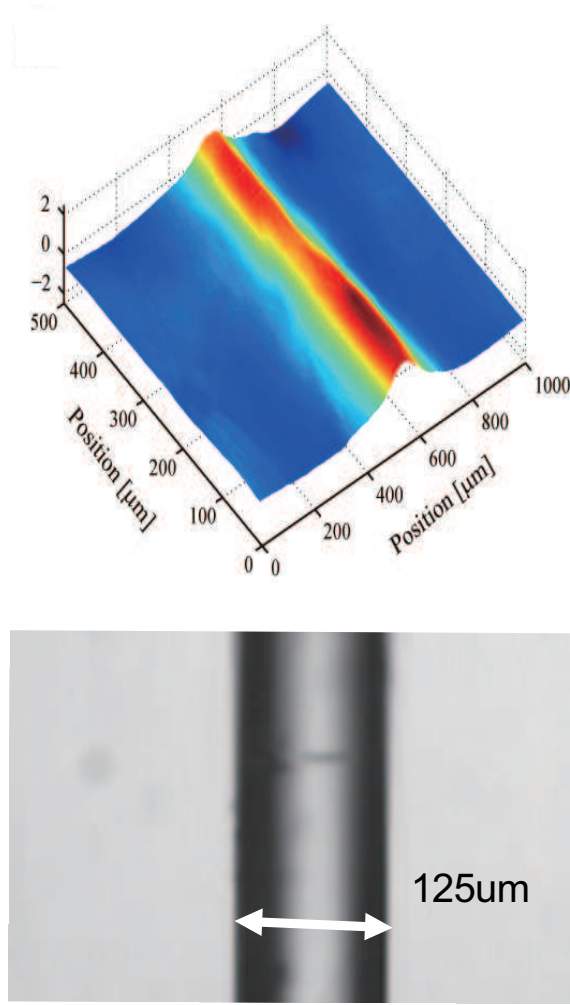


Figure 3.12: The THz-peak image of single mode optical fiber (HP780, Nufern) with 125- μm -diameter cladding. Cladding diameter is slightly smaller than $\lambda_0/2$. The image shows the cladding region of optical fiber and do not resolve the core of optical fiber with 5.5 μm , which is smaller than the resolution of developed THz microscope.

Here, r is the radial distance from the center axis of the beam path, z is the propagation distance from the smallest beam-size position, and $R(z)$ is the radius of curvature of the wavefronts. $\zeta(z)$ is the Gouy phase shift, an extra contribution to the phase that is seen in Gaussian beams and k is the wavenumber. Following above equation, the time-averaged intensity distribution for propagation distance z :

$$I(r, z) = I_0 \left(\frac{w_0}{w(z)} \right)^2 \exp \left(\frac{-2r^2}{w^2(z)} \right), \quad (3.16)$$

where, $w(z)$ is the radius at which the field amplitude and intensity drop to $1/e$ and $1/e^2$, respectively. The spot size $w(z)$ will be at a minimum value w_0 at one place along the beam axis. For a monochromatic wave λ at a distance z along the optical axis, the beam waist is given by

$$w(z) = w_0 \sqrt{1 + \left(\frac{z}{z_R} \right)^2}, \quad (3.17)$$

where $z_R = \pi w_0^2 / \lambda$ is the Rayleigh range. A common method for measuring a laser beam spot size is directing the intensity measurement of laser beam while scanning a knife edge across the beam. Measured

intensity profile are easily fitted to evaluate the laser beam waist [72]

$$S(X) = 1 - \frac{1}{2} \operatorname{erfc} \left[\frac{\sqrt{2}(X - X_0)}{w_z} \right], \quad (3.18)$$

where X is the position of the scanning knife edge, X_0 is the center of the beam, and w_z is the desired $1/e^2$ half-width at specific propagation position. Fig. 3.14 shows the profile of radiated THz beam size (circles) are taken using the translating edge response method. The red line are fitted by Eq. 3.18. In Table 3.2, we observe how the ratio between evaluated THz waist and THz wavelength for different frequency components. The ratio shows that lower frequency components exhibit marked near-field properties. This similar results have been reported [73]. The ratio (circles) are flowing the line of Gaussian beam case.

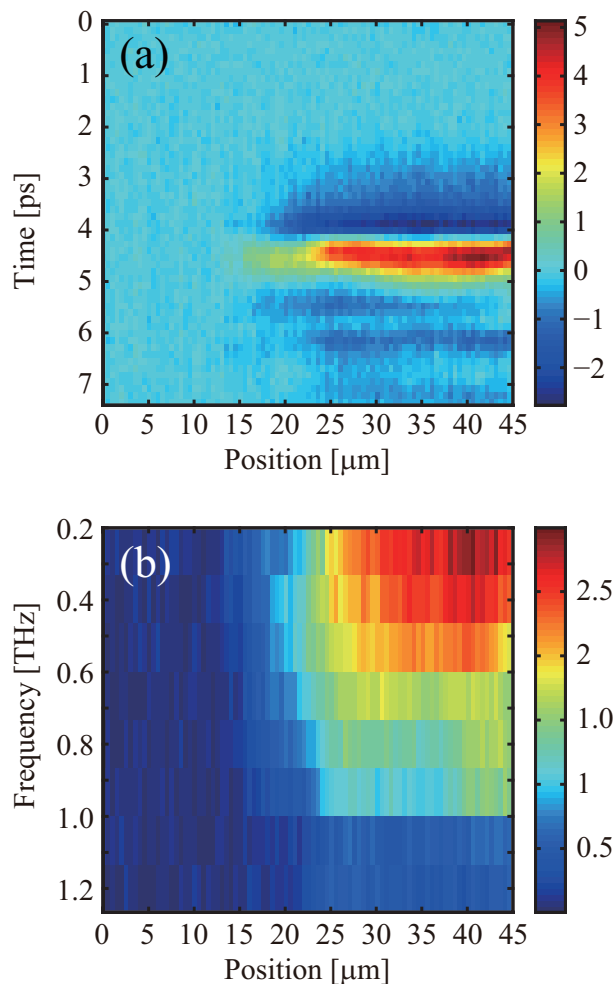


Figure 3.13: (a) Measured THz temporal signals and (b) their spectra as a function of different spatial position scanned on the surface of half-filled InAs film for edge response experiment

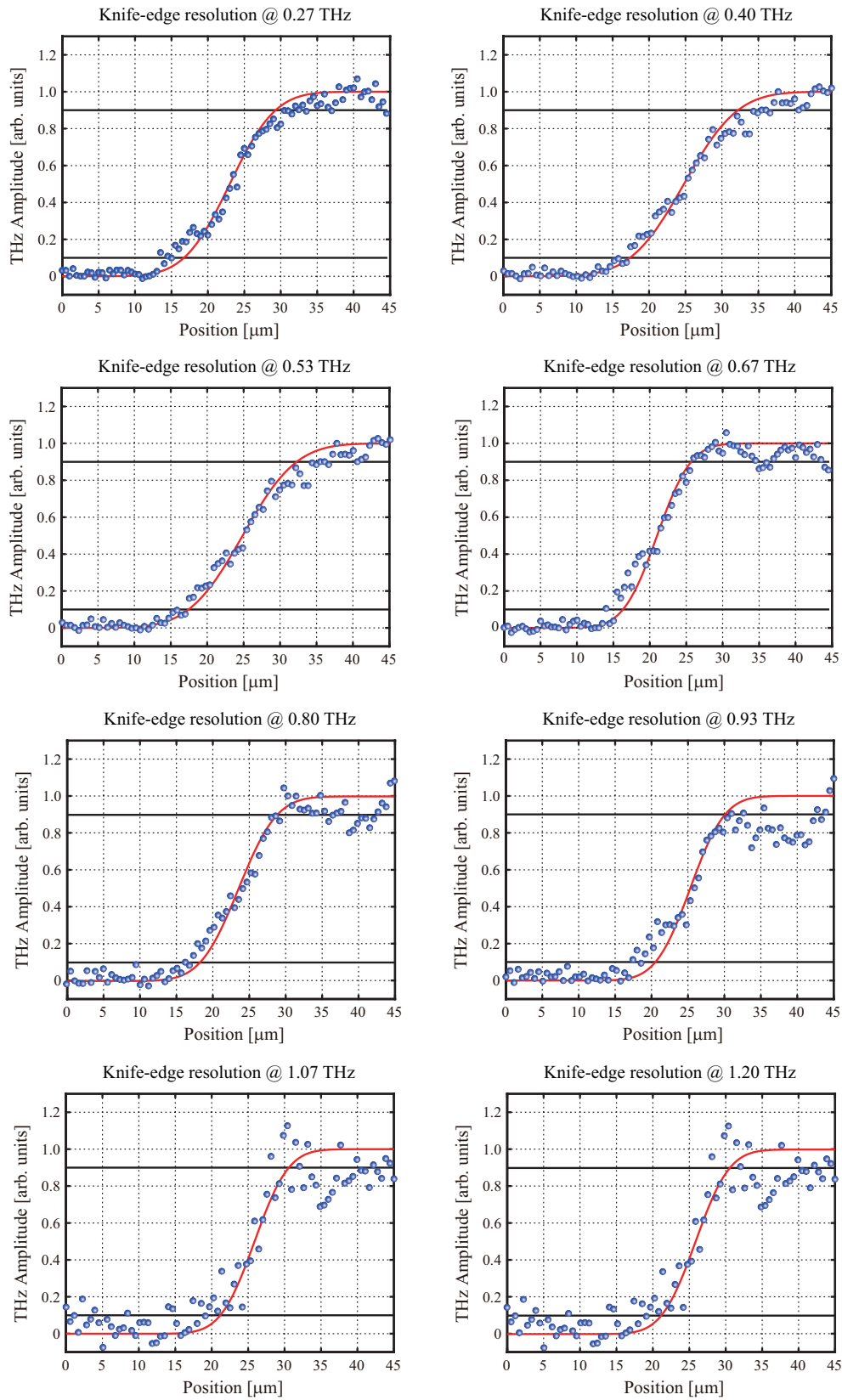


Figure 3.14: Radiated THz spectral amplitude profile (circles) taken using the translating edge response method. The red line are fitted by Eq. 3.18.

Table 3.2: Calculated waist, corresponding THz wavelength and fitted waist to wavelength ratio.

Frequency [THz]	Wavelength(λ_{THz}) [μm]	Beam waist(w_0) [μm]	$w_0/\lambda_{THz}[10^{-3}]$
0.267	1125.6	9.8	8.73
0.399	750.4	10.3	13.72
0.533	562.8	8.9	15.81
0.666	450.2	7.3	16.23
0.799	375.2	7.4	19.61
0.933	321.6	6.6	20.65
1.066	281.4	6.5	23.21
1.199	250.1	6.3	24.99

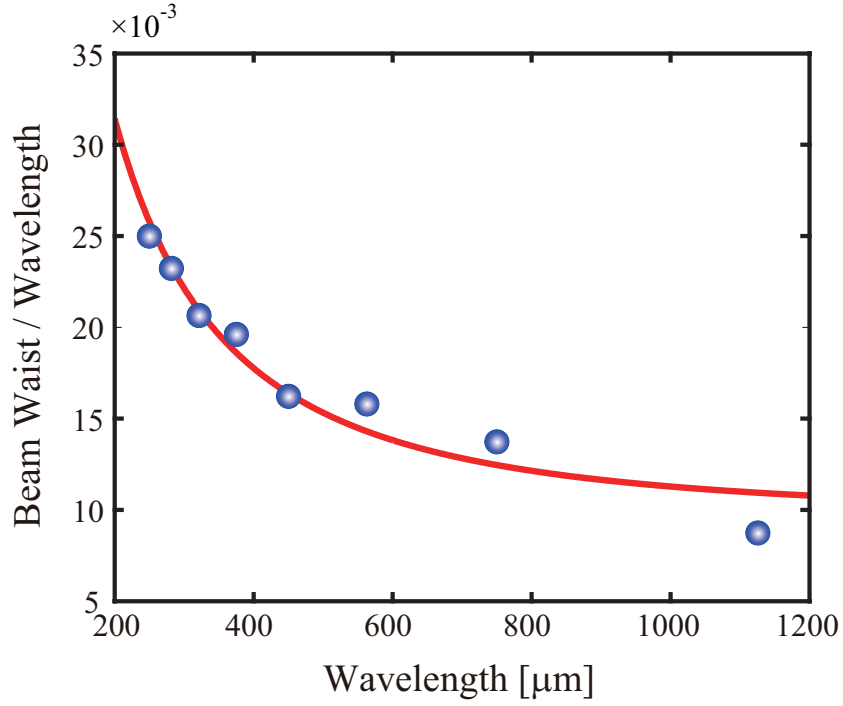


Figure 3.15: The ratio between evaluated THz waist and THz wavelength for different wavelength components. The ratio shows that longer wavelength components exhibit marked near-field properties.

Chapter 4. Terahertz phase microscopy in the sub-wavelength regime

4.1 Introduction

Technological advancement involved in THz frequency wave has attracted a great deal of interest in many different research areas of electromagnetic wave applications, such as material characterization, remote sensing, and biomedical imaging, to list a few [76, 77]. For example, THz imaging systems based on THz-TDS use either temporally- or spectrally-resolvable sample information obtained from transmissive or reflective THz signal. However, compared to the plentiful information of a broad-band THz pulse itself gained as a result of spectro-temporal response to a specific material the information used in conventional THz imaging methodologies is rather limited. Recently there have been attempts to use alternative information of THz pulses, and there are continuing efforts to discover unconventional usages of THz waves for more advanced and practical measurements for various imaging applications in THz frequency range [78, 79, 80, 81].

Phase microscope techniques are widely used for a specimen difficult to recognize in an ordinary light microscope [82, 83, 84]. In general, the spatial distribution of minute phase variation is translated into amplitude changes of optical waves that are transmitted through transparent and colorless objects. Quantitative phase microscopy (QPM), in particular, utilizes mathematically derived phase information of optical waves that are transmitted through transparent and colorless objects to visualize the phase profile of the sample [83, 84]. In an ordinary THz phase microscope, also known as THz time-of-flight microscopy, the time-delay difference of THz pulses is in correspondence with effective optical path length difference, and, therefore, the spatial phase information $\phi(x, y)$ that is quantified from a time-delay measurement $\Delta t(x, y)$ of THz pulses, as

$$\Delta t(x, y) = \frac{\Delta\phi(x, y)}{2\pi f}, \quad (4.1)$$

where f is the carrier frequency, could give the additional information to an ordinary THz amplitude image [85]. In this chapter, we report an observation of geometrically-induced phase shift of THz waves and its application to THz imaging of sub-wavelength-scale objects. In an experiment of THz wave generation from semiconducting InAs structure, we found that the pulses radiated from emitters of sub-wavelength scale are temporally shifted compared to the ones from larger scale emitters. With an imaging demonstration, we show that this size-dependent phase shift of diffracted THz waves can be used as a sensitive means to the recognition of sub-wavelength size structures.

4.2 Experimental description

For an experimental verification of the size-dependent phase shift of THz waves, we constructed a laser-THz emission microscope. Femtosecond optical laser pulses were used to generate THz pulses via the photo-Dember effect transmissively from a low-bandgap InAs film [74]. The InAs thin film of 1- μm thickness was grown by molecular beam epitaxy on an AlAsSb buffered GaAs substrate. The thickness

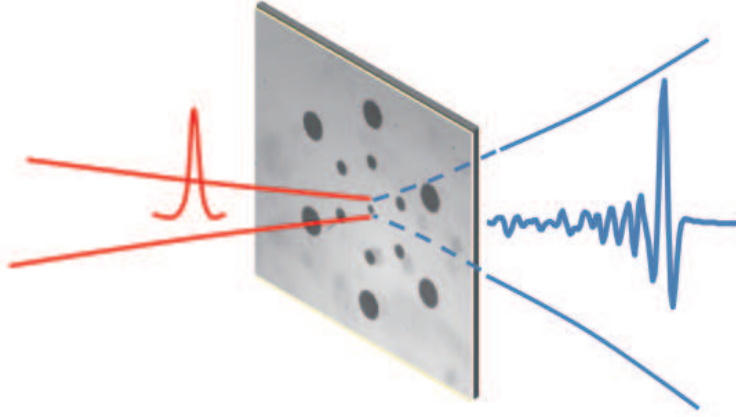


Figure 4.1: Schematic diagram of transmissive sub-wavelength THz phase microscope

was optimized by considering effective Dember charge separation and absorption and resolution of THz pulses. The as-grown InAs sample was glued to a sapphire substrate and then the substrate and buffer layer were eliminated by lapping and chemical etching by phosphoric acid solution ($\text{H}_3\text{PO}_4 : \text{H}_2\text{O}_2 : \text{H}_2\text{O} = 1 : 8 : 80, 1.3 \mu\text{m}/\text{min}$). The THz pulses radiated from the InAs thin film were detected by conventional $4f$ geometry and a conventional photoconductive antenna. For a variation of the diameter of excitation area, we patterned a metal screen with some circular holes on the surface of InAs. The aperture is formed in a 150 nm thick gold screen with 15-nm-thick Cr adhesion on a InAs surface by photolithographic methods. Figure 4.1 shows schematic diagram of transmissive sub-wavelength THz phase microscope.

Figure 4.2 shows measured THz temporal and spectral shapes for different size excitation InAs apertures which are varied from 30 to 200 μm when the excitation fluorescence of femtosecond laser pulses are fixed. As shown in the figure, smaller InAs aperture gives smaller THz emission area, so generated THz power is weaker. While decreasing the amplitude of generated THz pulses with smaller diameter apertures, a drastic change of the negative time delay is observed as a function of the diameter of excitation InAs aperture. This negative time delay is explained by the effective propagation constant of diffracted THz waves.

4.3 The Gouy phase shift of sub-wavelength emission aperture

In order to investigate the size-dependent phase shift of THz waves from sub-wavelength apertures, we first consider the Gouy phase shift, *which is size-independent*, formulated in the work done by Feng and Winful [86, 87]. The Gouy phase shift for single-cycle THz pulses passing through a focus was directly observed by the predicted polarity reversal [87].

The Gouy phase shift is originated from transverse spatial restriction of the wave and the uncertainty principle leads to the reduction of the longitudinal component of a propagation constant k . So, for a monochromatic wave propagating along z direction, the effective propagation constant \bar{k}_z is given by

$$\bar{k}_z = k - \frac{1}{k} \int \int (k_x^2 + k_y^2) |F(k_x, k_y)|^2 dk_x dk_y, \quad (4.2)$$

where k_x and k_y are the transverse spatial frequencies, or the vector components of the propagation constant k , (i.e., $k_x^2 + k_y^2 = k^2 - k_z^2$), and their distribution $F(k_x, k_y)$ is the Fourier transform of the

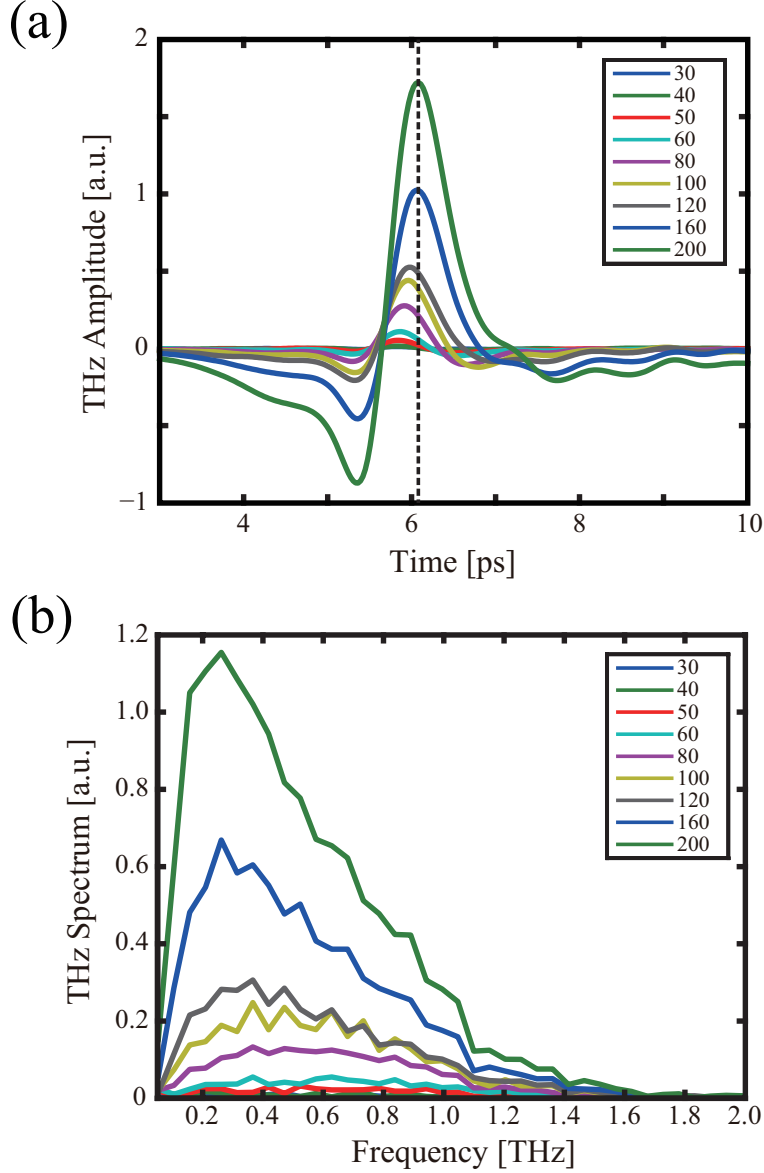


Figure 4.2: (a) Temporal and (b) spectral THz waveforms generated from InAs apertures varying the diameter from 30 to 200 μm .

spatial profile of the wave. Then, the Gouy phase shift ϕ_G^0 is given by

$$\phi_G^0 = \int (\bar{k}_z - k) dz. \quad (4.3)$$

For a Gaussian beam propagation from $-\infty$ to ∞ , a constant Gouy phase shift $\phi_G^0 = \pi$ is obtained, regardless of the size of the beam.

Now we suppose a situation when the spatial restriction is severe enough that a sub-wavelength size effect should be explicitly considered. If the transverse size of a beam is smaller than the wavelength, the extent of the spatial-frequency distribution $F(k_x, k_y)$ reaches outside the area of radius k . There, the longitudinal component k_z becomes imaginary, (i.e., $k_z = i\sqrt{k_x^2 + k_y^2 - k^2}$), and an evanescent wave is formed. So, in Eq. 4.2 the area of integration outside $k_x^2 + k_y^2 \leq k^2$ needs to be excluded from the calculation. Therefore, the effective propagation constant \bar{k}_z (real part only) becomes

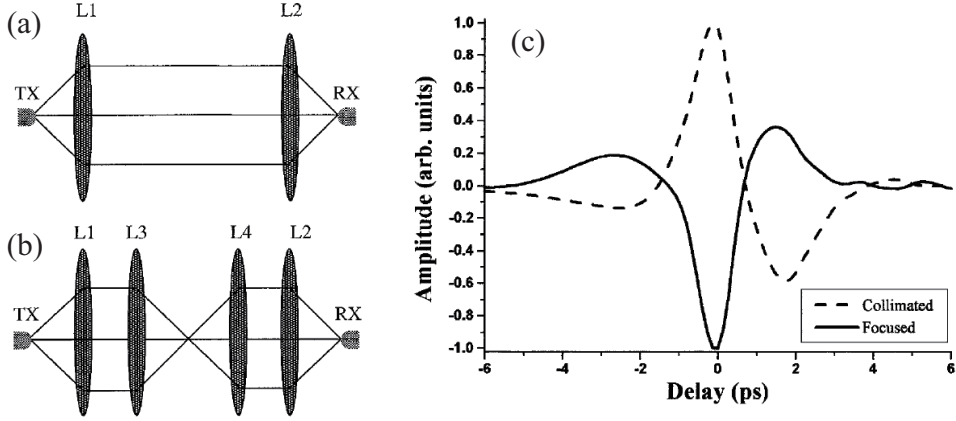


Figure 4.3: The schematic experimental setup for direct observation of Gouy phase shift showing the lens configurations: (a) collimated and (b) focused configuration. (c) Dashed and solid curve: measured THz pulse in the collimated configuration (a) and the focused configuration (b), respectively [87].

$$\overline{k_z} = k - k \int \int_{k_x^2 + k_y^2 > k^2} |F(k_x, k_y)|^2 dk_x dk_y - \frac{1}{k} \int \int_{k_x^2 + k_y^2 < k^2} (k_x^2 + k_y^2) |F(k_x, k_y)|^2 dk_x dk_y, \quad (4.4)$$

where the last two terms contribute to the Gouy phase shift. The given integral calculations are strongly influenced by the relative size of the propagation constant k compared to the inverse of the transverse spatial extent of the wave. For a beam of sub-wavelength waist w , it is straightforward to show that Eq. 4.4 leads to

$$\frac{d\phi_G}{dz} = -k \left(1 - \frac{w^2 k^2}{4} \right), \quad (4.5)$$

which is valid for $w^2 k^2 / 2 \ll 1$.

The numerically calculated Gouy phase shifts ϕ_G of THz pulses from sub-wavelength emission apertures of various sizes are summarized in Fig. 4.4. Compared to ϕ_G^0 (dashed line) of the one from a large-size aperture ($w = 2\lambda$), the Gouy phase shifts ϕ_G for three different-size apertures, $w_1 = \lambda/40$ (black), $w_2 = \lambda/20$ (red), and $w_3 = \lambda/40$ (blue), are plotted from top to bottom.

The THz waves under consideration are radiated from a sub-wavelength-size small emitter of beam waist w_0 located at $z = 0$, and we are interested in obtaining the w_0 -dependence on the phase shift (ϕ_G) of the THz pulse, measured at $z = \infty$, with respect to the phase of THz pulses from a large-size emitter. Using the chain rule of differentiation, we get

$$\frac{\delta\phi_G}{\delta w_0} = \frac{\partial}{\partial w_0} \int_{w_0}^{\infty} \frac{d\phi_G/dz}{dw/dz} dw = \frac{k}{\alpha}, \quad (4.6)$$

where w is the beam waist given as a function of z and its derivative becomes asymptotically a constant α before a sub-wavelength propagation (i.e., $z \ll \lambda$). It is noted that the sub-wavelength wave propagation accumulates negligible phase shift. As a result, the size-dependent Gouy phase shift is expected to be linear to the initial beam waist w_0 , at the sub-wavelength aperture limit.

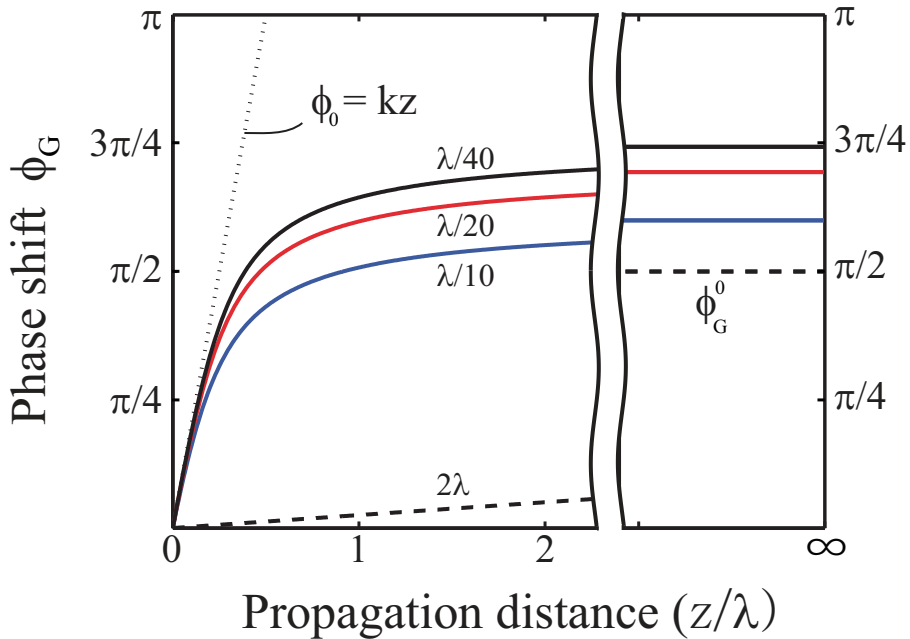


Figure 4.4: Calculated Gouy phase shifts ϕ_G of THz pulses radiated from sub-wavelength emission apertures. The Gouy phase shifts ϕ_G for three different-size apertures, $w_1 = \lambda/40$ (black), $w_2 = \lambda/20$ (red), and $w_3 = \lambda/10$ (blue) are plotted with ϕ_G^0 (dashed line) of the one from a large-size aperture ($w = 2\lambda$).

4.4 Terahertz sub-wavelength phase microscopy

In experiments, for the measurement of time delay, we used the first temporal moment, or the centroid time, defined as

$$\tau(x, y) = \frac{1}{I(x, y)} \int' (t(x, y) - t_0) E^2(x, y; t) dt, \quad (4.7)$$

where the summation (\int') is taken for positive temporal signal only, (i.e., $E(x, y; t) > 0$), over a finite time window, and t_0 is the reference time. The energy normalization is also given similarly as $I(x, y) = \int' E^2(x, y; t) dt$.

Figure 4.5 (b) shows the centroid time of radiated THz pulses are given as a function of the diameter of the InAs emission aperture. The diameter was varied from 30 to 200 μm and the excitation fluorescence of femtosecond laser pulses was kept constant. As shown in the figure, there is a drastic change of the negative time delay as a function of the diameter of the excitation InAs aperture. The THz pulses are further temporally advanced, shifted in the negative time direction, for smaller excitation apertures. Similar behavior has been reported in THz waveguide experiments through sub-wavelength apertures, but the phenomenological explanation in the context of an anomalous index change in waveguide coupling process has not successfully provided a clear picture for its physical origin [68, 88]. In our experiment, this temporal phase shift is explained by the geometrically-induced phase shift of radiated THz pulses which is dependent of the size of emission apertures. As mentioned above, the size-dependent Gouy phase shift is expected to be linear to the initial beam waist at the sub-wavelength aperture limit.

The geometrically-induced phase shift of THz waves can be extended to THz imaging of sub-wavelength-scale objects. For THz phase microscope imaging, we have patterned and tested a hexagram

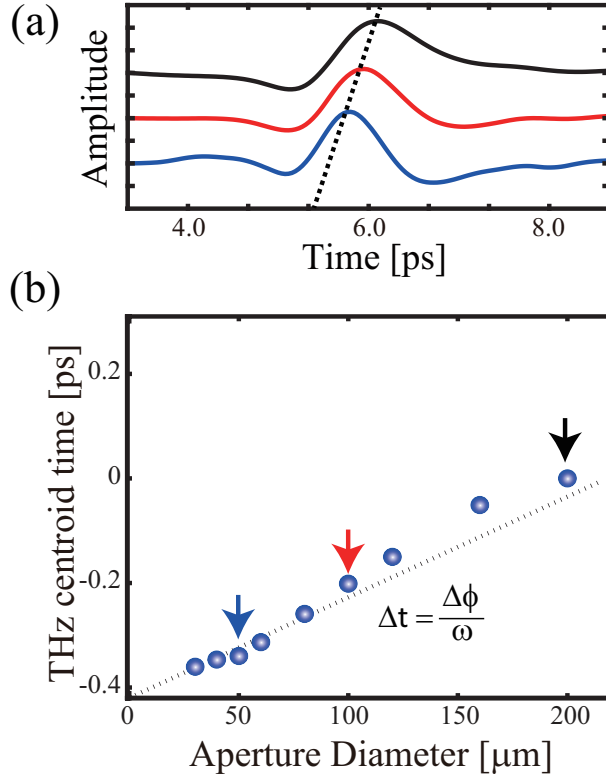


Figure 4.5: (a) Radiated THz pulses for three different-size InAs emission apertures; 50-(blue), 100-(red), and 200- μm (black) from bottom to top. (b) The centroid time of radiated THz pulses for various different-size InAs emission apertures from 30 to 200 μm (circle) and calculated temporal advancement of THz pulses (dashed line).

pattern. Figure 4.6 (a) shows the optical image of the sample. The hexagram consists of three different circular InAs apertures: 30, 50 and 100 μm . All the temporal THz signals were measured for all two-dimensional pixels scanned with 60- μm -diameter near-infrared pulses. A THz intensity image $I(x, y)$ of the hexagram is shown in Fig. 4.6 (b). The intensity image is not appropriate to resolve smallest hole due to weak THz signal. However, the temporal phase image resolve sub-wavelength 30- μm patterns by using the contrast of temporal phase difference as shown Fig 4.6 (c). As shown the Eq. (4.6) and Fig. 4.5 (b), the smaller the emission diameter is used and the earlier the centroid time of the radiated THz pulses occurs. We have experimentally confirmed that temporal phase image resolve sub-wavelength 30- μm patterns by using temporal phase difference due to difference arrival time of THz pulses.

4.5 Discussion

In summary, we have studied temporal characteristics of THz pulses generated from InAs apertures. Temporal phase advancement of THz pulses occurs when THz pulses is generated from sub-wavelength InAs emission apertures. This temporal phase shift is explained by the beam-waist-dependent Gouy phase shift, of which the physical origin is the sub-wavelength spatial confinement of the propagating wave. By using the geometrically-induced phase shift of radiated THz waves, we have explained the temporal phase shift when spatial frequency of the beam size is larger than k . This phase shift behavior can be applied to sensitive recognition of micrometer-size patterns smaller than the wavelength of THz pulses.

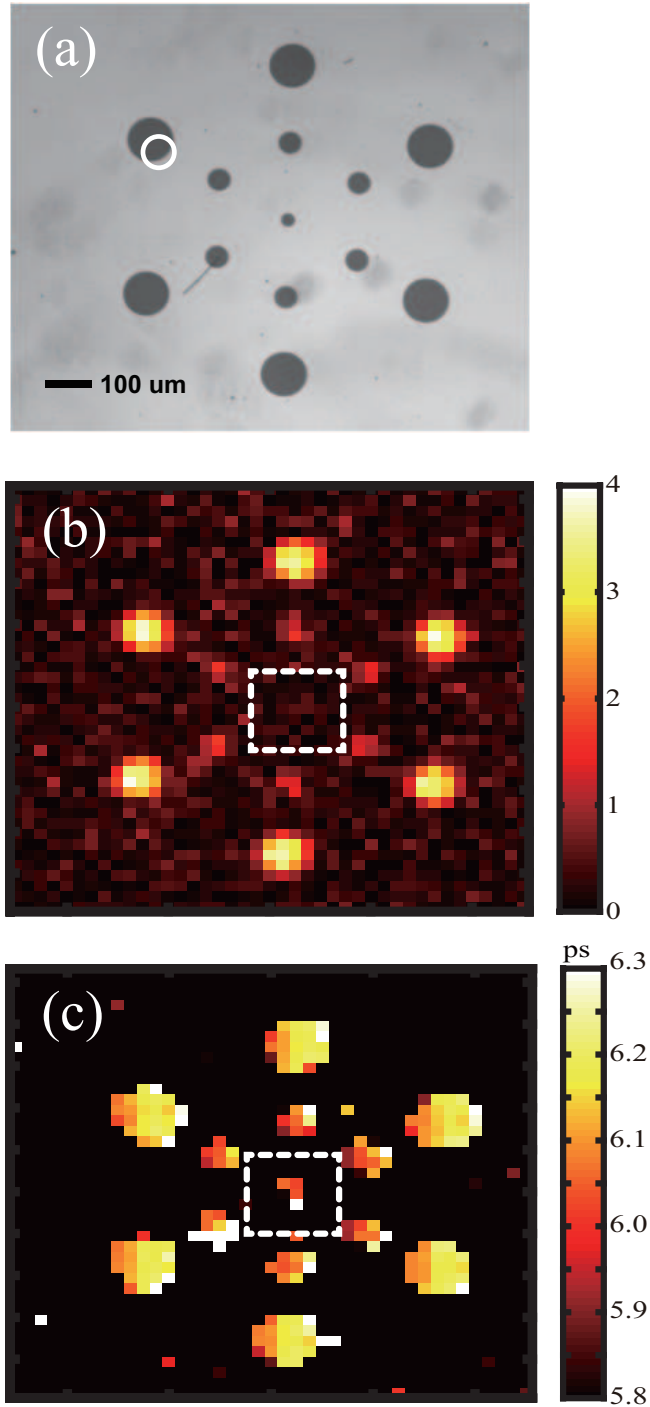


Figure 4.6: (a) The microscope image of hexagram which consists of 30-, 50- and 100- μm diameter InAs emission apertures. (b) Measured THz intensity image and (c) THz temporal phase image scanned with 60- μm -diameter NIR pulses.

In the proof-of-principle demonstration of THz phase imaging, we have verified that the temporal phase difference of THz waves can resolve small objects of sub-wavelength size. This effect of geometrically-induced phase shift is a generic wave property in the sub-wavelength regime and, therefore, further studies with other wave sources in various frequency range are warranted.

Chapter 5. Terahertz optical fiber emitter

5.1 Introduction

Technological advances in THz region have already made possible the development of spectroscopic imaging systems to obtain spatially and temporally resolvable sample information. The major technical obstacles for most THz imaging applications are absorption loss by water vapor, the difficulty in miniaturizing the system size, and the rather poorer imaging resolution than in the conventional spectral region.

In a generic THz imaging system based on passive optical components such as lenses and/or parabolic mirrors, the spatial image resolution is diffraction-limited to a few hundred microns. To overcome the diffraction limit, that is, to obtain a THz image of sub-wavelength scale, scanning near-field microscope techniques, also known as THz-SNOM, have been used [59, 60, 89, 90]. The resolution is then not limited by the wavelength of the illuminating electromagnetic source, but rather by geometrical parameters such as the size of an aperture or a scatterer. However, in a THz-SNOM the detected THz signal is small and bandwidth-limited [60, 91]. Many attempts have been made to improve the signal-to-noise ratio and also the bandwidth of the THz signal [59, 92]; one alternative approach is guiding the THz wave through a probing tip [65]. However, the low coupling efficiency and radial distribution of the guided THz signal make finding an easy-to-use application of this method difficult.

Additionally, sending THz waves through an elongated object, or THz waveguide, has been studied with metal wires [93], plates [94], and fibers [95, 96], and cables [97]. Even in those studies, because of attenuation and the bending losses, most of these waveguide methods are not viable in THz near-field spectroscopy and imaging [98]. The alternative is to generate and capture the THz signal near the sample by using an optical-fiber-coupled infrared (IR) pulse [99].

In this chapter, we have described an idea for emitting THz waves directly from a conventional optical fiber. The end facet of the optical fiber is polished at a specific angle and coated with an InAs thin film. An intense-field-density laser beam, guided through the optical-fiber core, illuminates the InAs film and generates the THz waves. In a proof-of-principle experiment using the alignment-free THz source, we have performed THz-TDS and near-field THz microscopy.

5.2 Experimental description

THz waves were generated via the photo-Dember effect, or electric dipole formation near the surface of a semiconducting material, during ultrafast photoabsorption [25]. The mobility difference between electrons and holes forms an effective charge separation along the surface normal. The direction of THz emission in the reflection geometry under a focusing condition of the excitation beam is along broadly 45 degree from the InAs surface normal [40]. The optical-fiber tip was therefore cut at an angle of 45 degrees to generate THz waves transmissively along the optical beam direction; see Fig. 5.1. The photo-Dember effect is relatively strong in narrow-band gap III-V semiconductors with high electron mobility, such as InAs and InSb, and therefore, they emit THz waves at an order of intensity magnitude higher than those of relatively wide band gap semiconductors such as InP and GaAs [40]. By using the intrinsic mobility

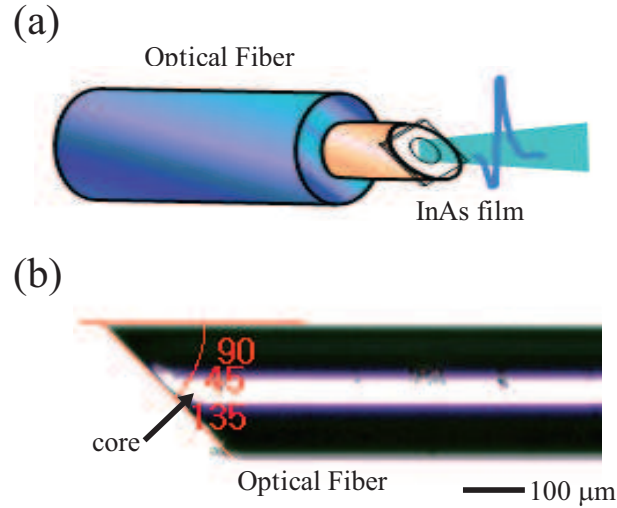


Figure 5.1: (a) Schematic diagram of the optical-fiber THz emitter and (b) microscopic photograph of 45-degree angle cut optical fiber.

of InAs ($30,000 \text{ cm}^2/(\text{V} \cdot \text{s})$), the excess energy (1.2 eV from a 1.55-eV photon) at room temperature, and the momentum relaxation time of 500 fs, the diffusion length is estimated as $1.3 \mu\text{m}$. Considering the THz absorption and effective Dember charge separation, we estimated that a $1\text{-}\mu\text{m}$ -thick InAs film would be optimal.

The (100)-oriented InAs thin film was grown by using molecular beam epitaxy on AlAsSb buffered semi-insulating GaAs (SI-GaAs) substrates. The AlAsSb buffer and the grown InAs film thicknesses were $2.2 \mu\text{m}$ and 875 nm , respectively. The SI-GaAs substrate is eliminated by lapping and chemical etching. The wet chemical etch process is enhanced by a phosphoric acid solution etchant ($\text{H}_3\text{PO}_4 : \text{H}_2\text{O}_2 : \text{H}_2\text{O} = 1 : 1 : 5$) with an etch rate of $\sim 1.12 \mu\text{m}/\text{min}$. The wet chemical etching layout for the InAs thin film is shown in Fig. 5.2. The InAs film was cut down to the size of the fiber facet and then glued to the optical-fiber tip with optical epoxy. The end facet of the optical fiber is polished at 45° angle. An intense femtosecond pulses are guided through the optical-fiber core and excite the InAs film to generate THz pulses. Figure 5.3 shows the constructed THz optical-fiber near-field microscope.

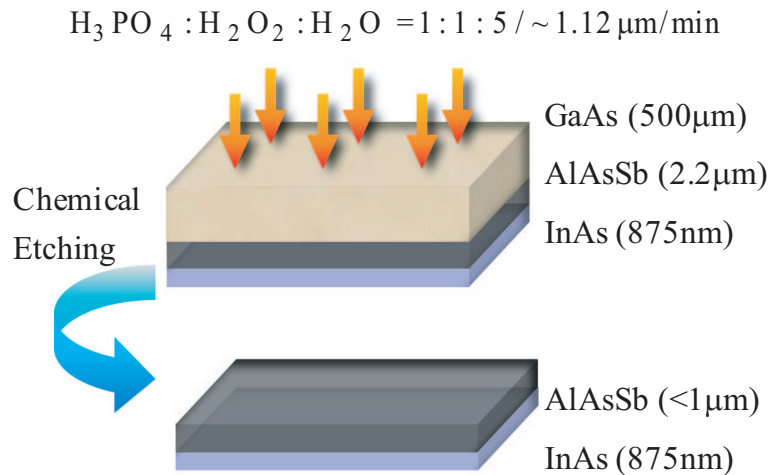


Figure 5.2: InAs film fabrication layout.

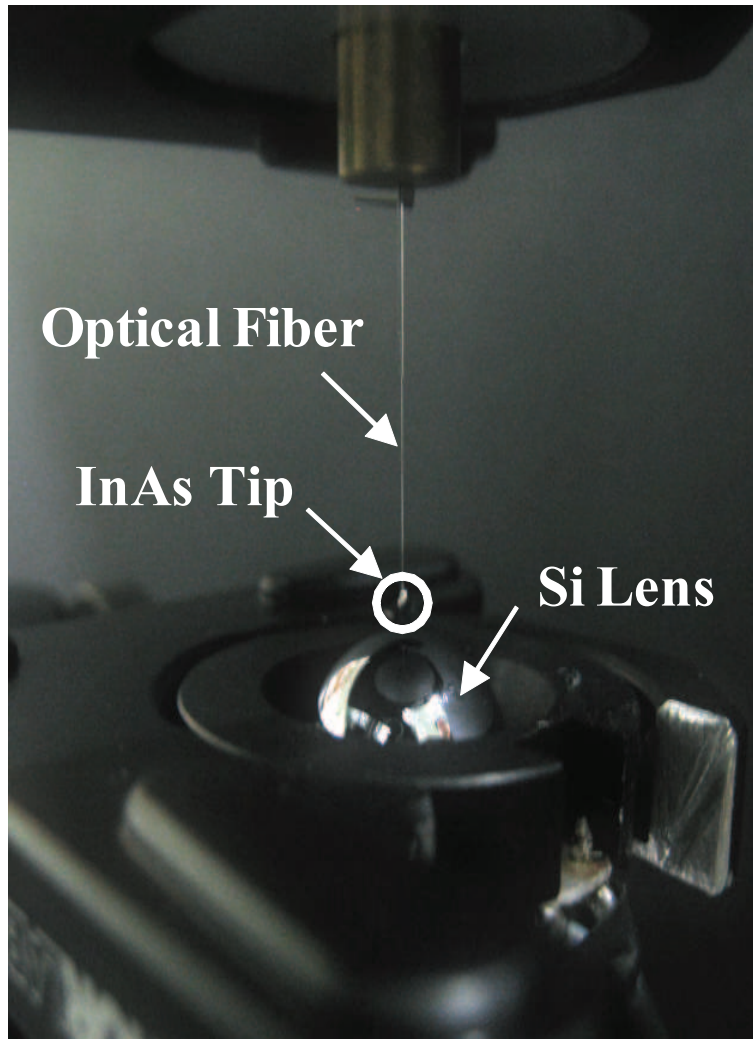


Figure 5.3: Setup photograph of the THz optical-fiber tip in a near-field microscope application.

In order to test the THz emission of this device, we used 1.55-eV photons in 70-fs ultrashort pulse trains produced in a Ti:sapphire laser oscillator at a repetition rate of 90 MHz. For the generation and optically-gated detection of the THz waves, the laser pulses were physically separated by a beam splitter and temporally shifted by a variable delay line. The optically pumped beam for the THz generation was then coupled to a 50- μm core diameter optical fiber. The 10-mW average laser pulses were then guided through a 20-cm-long optical fiber without dispersion compensation. The THz pulses radiated from the InAs thin film fixed on the polished optical-fiber tip were detected by a conventional photoconductive antenna (PCA) through a silicon lens. The time-delayed probe beam was focused on the PCA for temporal gating. Although the silicon lens in front of the PCA is assembled to optimally detect collimated incident THz waves, the fastly diverging THz signal emitted from the constructed fiber tip was readily detected in the experiment. The photocurrent measured from the PCA was proportional to the generated THz electric field amplitude. The measured THz temporal signal and its amplitude spectrum from the conceived THz emitter are shown in Fig. 5.4. The measured spectral bandwidth is nearly 2 THz.

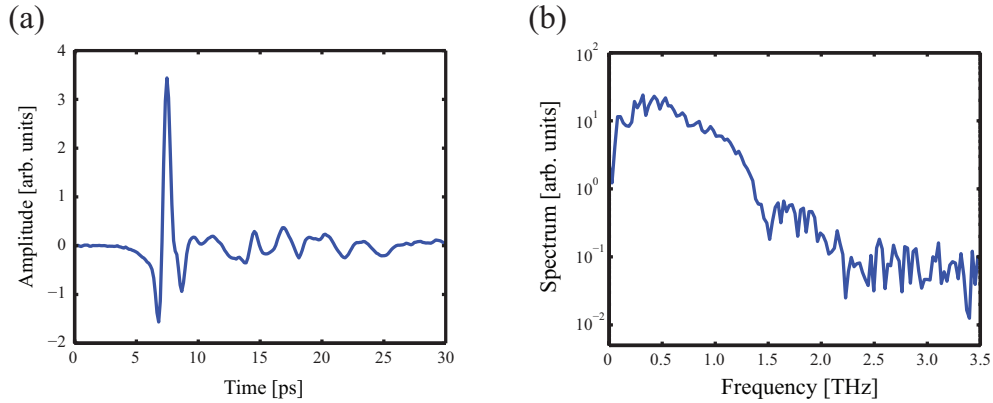


Figure 5.4: (a) Measured THz temporal waveform from the optical-fiber THz emitter and (b) The amplitude spectrum of the THz pulse shown in (a).

5.3 Terahertz optical fiber emitter and imaging

The mechanism of THz generation from InAs can be explained by both optical rectification and photo-Dember effect. Especially the THz waves from the optical rectification process has THz amplitude dependence on the polarization state of the pump beam. In our design of optical-fiber THz emitters, we have used (100)-oriented InAs from which the THz emission is dominated by the photo-Dember effect. Upon the pump beam incident being on the InAs surface, the gradient of the photoexcited electrons and holes is created due to the diffusion velocity mismatch between the electrons and holes. Then, the resulting photo-Dember current is polarized perpendicularly to the surface, and the generated THz pulse is p -polarized. Figure 5.5 shows the azimuthally angle-dependent amplitude of THz temporal waveforms measured as the optical fiber was rotated around the optical axis. The PCA detector recorded the horizontal polarization component of the THz waveforms as a function of time. The THz signals detected at three different times in Fig. 5.5 (a) show the sinusoidal pattern around the optical axis, as shown in Fig. 5.5 (b). This measurement shows that the measured THz signal is linearly polarized, as expected in THz generation process from the photo-Dember effect [100].

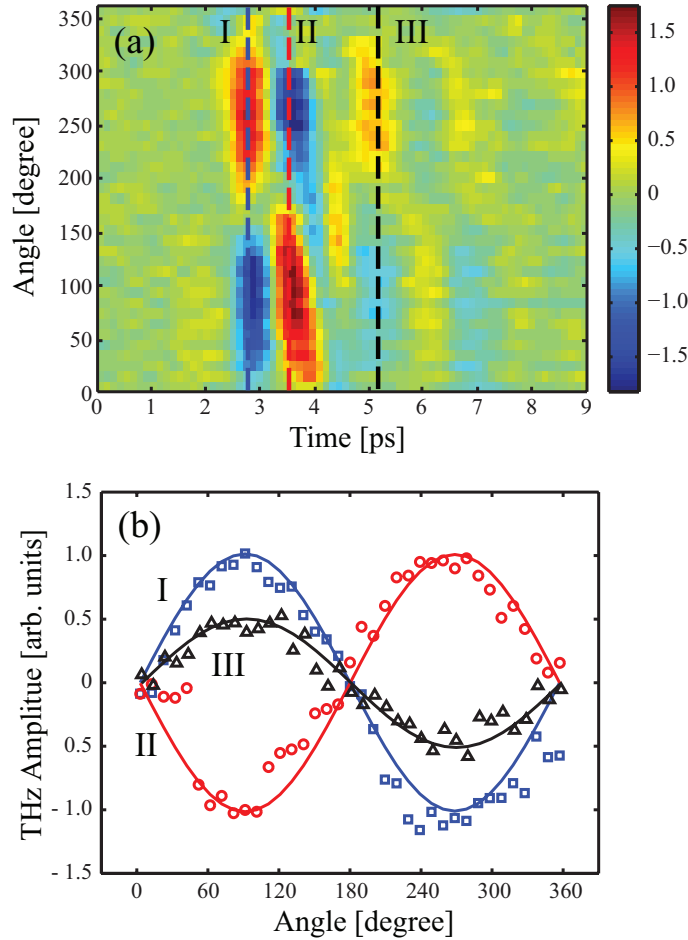


Figure 5.5: (a) Measured temporal THz image of horizontal components of the THz field emitted from the fiber tip as a function of rotation angle. (b) The sinusoidal angle dependence around the optical axis at three different times (dashed line) shown in (a).

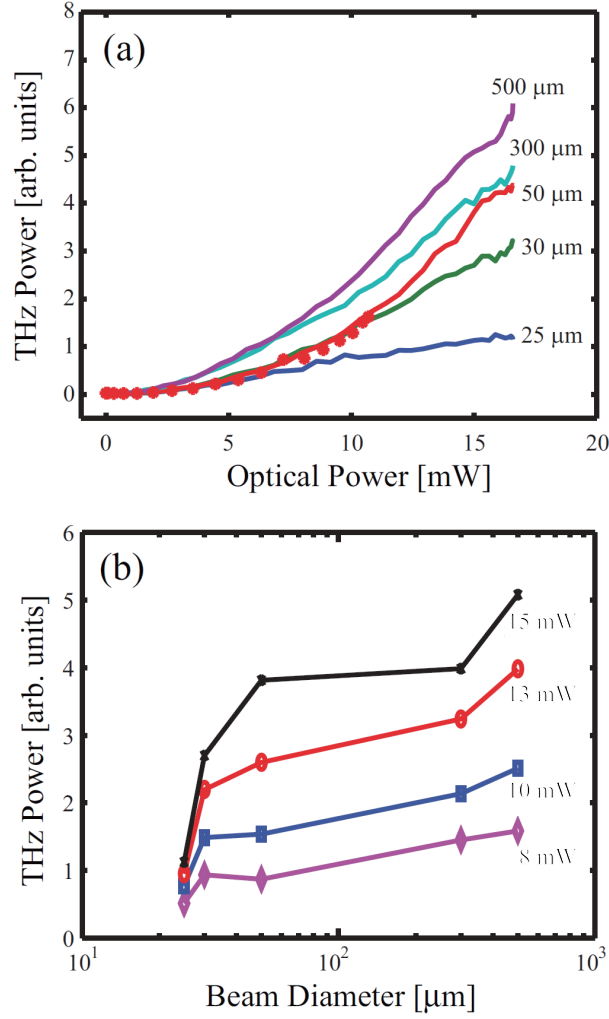


Figure 5.6: (a) Optical power dependence of measured THz pulses from the devised optical-fiber THz emitter (star) and a bare InAs film attached to a 500- μm -thick sapphire substrate (solid line). (b) The optical beam diameter dependence on measured THz power from the bare InAs film at some different optical power.

The 50- μm core diameter of the optical fiber was chosen because of the compatibility between generated THz power and resolution, which are simultaneously dependent on the core diameter. Figure 5.6 (a) shows the dependence of measured THz power on the incident optical power from the devised 50- μm core diameter THz emitter (star) and the bare InAs film on the 500- μm -thick sapphire substrate (solid lines). If a larger InAs area is excited by a given optical pulse under the saturation regime, greater THz power is obtained due to the increased induced photo-Dember field area. However, as the core size is increased, the resolution worsens because it relies on the size of the optical-fiber core. Therefore, to select the core diameter, we studied the dependence of the generated THz power on the optical beam diameter and incident optical power, which was applied to the sapphire substrate side. Two regimes must be dealt with: $D \geq \lambda_{\text{THz}}$, and $D \ll \lambda_{\text{THz}}$, where D is the diameter of the optical beam and λ_{THz} is the typical wavelength of a THz pulse ($\lambda_{\text{THz}} \sim 300 \mu\text{m}$). From the results shown in the Fig. 5.6 (b), we anticipate comparatively greater THz power with sub-wavelength resolution when the optical beam diameter has a 50- μm core fiber for $D \ll \lambda_{\text{THz}}$.

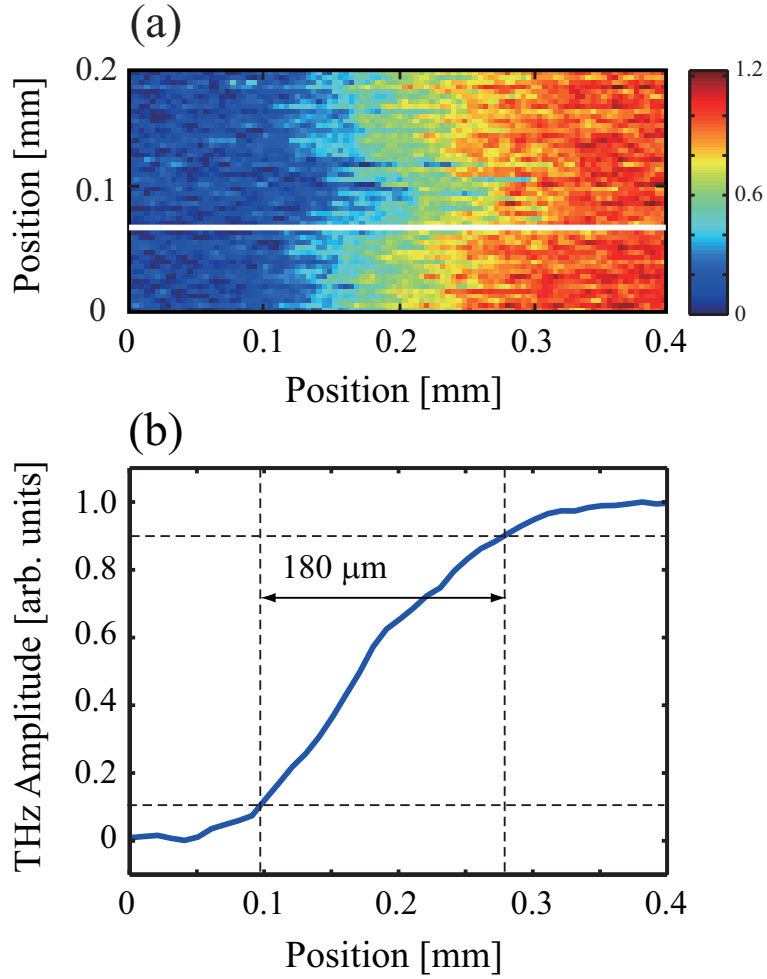


Figure 5.7: (a) A knife-edge THz image using an 18- μm -thick aluminum foil. (b) The lateral THz amplitude profile taken from a line as drawn in (a).

The spatial resolution of the THz emission fiber tip is demonstrated using a knife-edge method. The image target is an 18- μm -thick aluminum foil, placed at the distance of 100 μm from the optical-fiber core. This distance is due to the 45-degree-cut angle of the optical-fiber tip and the width of the fiber cladding. Keeping the relative time fixed at the THz pulse peak, we measured the THz amplitude using a $4f$ conventional THz-TDS system. Figures 5.7 (a) and (b) depict a knife-edge imaging. The edge of the foil was moved from left to right, and an area of $400 \times 200 \mu\text{m}^2$ was scanned. The resolution of the microscope tip is measured 180 μm , defined by the 10-90% criteria from the lateral profile taken from the line as drawn in the image in Fig. 5.7 (a). This resolution is three times bigger than the size of the fiber core diameter, because of the positional departure of the sample from the tip due to the slanted end facet of the fiber and the thickness of the optical epoxy and InAs film.

For a near-field imaging proof-of-principle experiment, a metal sieve pattern of sub-wavelength dimension ($200 \times 200 \mu\text{m}^2$ area open squares with 100- μm -wide metal wires) was measured. The optical image of the metal sieve is shown in Fig. 5.8 (a), and the result is shown in (b). A THz-emission microscope-tip image of this sieve, superimposed on an optical microscope image, is shown in Fig. 5.8 (b) and a plot of measured THz amplitude as a function of lateral position at dashed line in (b) is also shown in Fig. 5.8 (c). The spatially resolved THz-field image shows the pattern of the metal sieve. The

100- μm -wide metal wire lines and the open square area are apparently resolved. The slight blurring of the scanned image is attributed to the presence of the weaved shape in the real object as well as the distance between the source and the object. The distance between the fiber tip and the metal mesh was about 150- μm because of the tilted tip and cladding of the optical fiber. Using this method, the size of this THz emitter may be reduced to the size of an optical-fiber core, 1000 times smaller than previously considered PCA-based optical-fiber THz emitters. Furthermore, the fabrication of this kind of THz emitters is nearly a material coating process, not a device assembly. This type of THz fiber emitters can be used as a topographical scanning THz probe tip and also bundled for a large area THz emitter.

5.4 Discussion

In summary, we report a simple method of making an optical fiber emit THz waves. We have devised and demonstrated an optical-fiber THz emitter using a (100)-oriented InAs thin film placed on a 45-degree wedged optical-fiber tip. The THz wave generation mechanism from the optical-fiber tip is explained by the photo-Dember effect in a relatively low band gap semiconductor. In a proof-of-concept experiment using the alignment-free THz source for THz-TDS and THz imaging, we obtained a bandwidth of 2 THz and sub-wavelength spatial resolution. This spatial resolution is measured as 180 μm , three times the size of the optical-fiber core. Using this method, the THz imaging resolution is expected to be improved to the size of the optical-fiber core. The designed compact THz emission tip here can be extended to near-field imaging, spectroscopy, polarization studies, and remote sensing with sub-wavelength resolution.

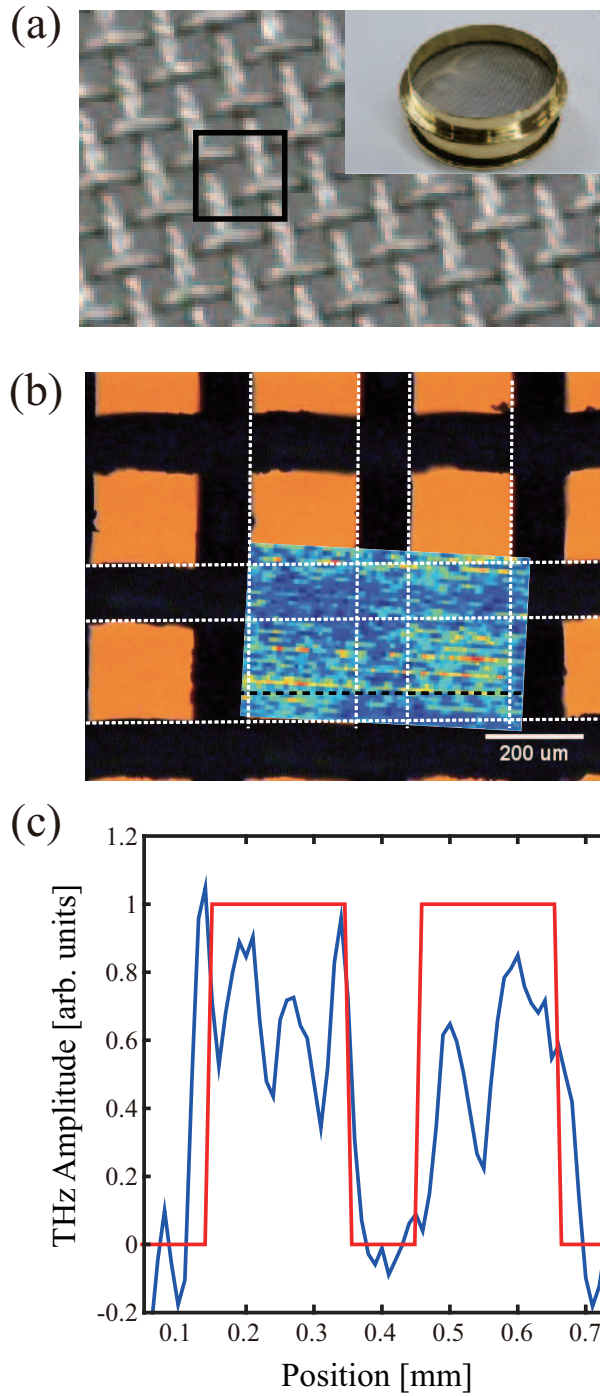


Figure 5.8: (a) Optically magnified photo of the metal sieve and an overall view (inset). (b) A THz near-field image superimposed on an optical microscope image. (c) Measured THz amplitude as a function of lateral position at dashed line in (b).

Chapter 6. Terahertz shaped pulse spectroscopy and imaging

6.1 Introduction

During the past several decades, technological advances in THz electromagnetic wave region have made a great deal of impact on a variety of research fields, including atomic and material physics, biomedical research, and organic and inorganic chemistry [76]. In particular, the application of THz waves to biological and medical imaging as well as nondestructive inspection has drawn keen attention of many researchers, because of its functional imaging capability in conjunction with THz-TDS [8].

THz-TDS utilizes temporal profile measurement of ultrafast THz pulses transmitted through a material and its Fourier transform results in the material's spectral response in broad frequency range in $0.1 \sim 10$ THz. However, as the temporal measurement of a picosecond-short THz pulse is not easily achievable in general, temporal scanning methods with optical gating are used for the amplitude measurement of THz waves, which take measurement time ranging from a few milliseconds even up to a few minutes, depending on the spectral resolution that is required [101]. In many situations of THz spectroscopic usage, one needs to identify an unknown material by comparing its THz response with its correlations to an archival set of THz spectra of known materials. In that regards, instead of the time-consuming temporal profile measurement, direct spectral correlation measurement, for example, by using predetermined shaped THz waveforms, may be enough. Therefore, in this paper, we consider waveform-shaping of THz frequency waves and its use for spectral correlation measurement, for the purpose of material classification.

As for the waveform shaping of short pulsed electromagnetic waves, there has been much interest in optical frequency domain, in part because of its applications in telecommunication and signal processing [102], and in part because of its usage as a new kind of optical means for selective control of electronic and vibrational responses of materials, for example, in high harmonic generation in gases [103], multi-photon absorption spectroscopy [104, 105, 106], and coherent control of molecular processes [107, 108]. The optical shaped pulses have been also used to investigate the physical phenomena occurring in THz frequency region, for example, selective excitations of phonon modes in molecular crystals [109], charge oscillations in semiconductor heterostructures [110, 111], and phonon-polaritons in a lithium tantalate [112] to list a few.

For the generation of arbitrary THz pulse shapes, several methods have been developed to extend the generation of arbitrary THz pulse shapes. Most of the methods are based on the generation of THz pulses from various types of emitters with spatially and/or temporally shaped optical pulses. Temporal pulse shaping methods via optical rectification [113, 114, 115, 116], ultrafast photo-excited carrier generation [117, 118], and spatial pulse shaping [119] have been studied. In addition, lithium niobate crystals [120] and air plasma breakdown phenomena [121] have been used to generate tunable THz waveforms by controlling spatial and temporal profiles of optical pulses. However, still there are few practical imaging methodologies which explicitly takes the full advantage of those elaborately shaped THz pulses.

In the rest of this chapter, we show a new possibility of selective THz functional imaging by using

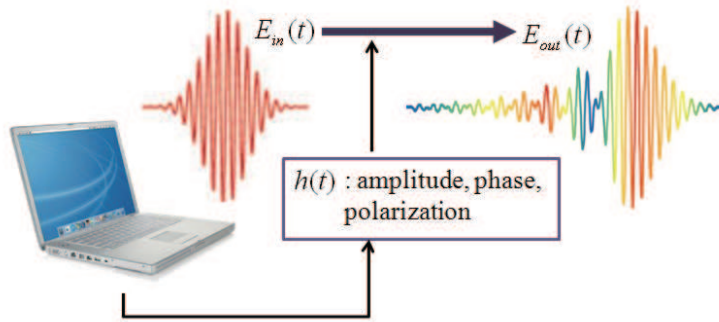


Figure 6.1: A concept of femtosecond laser pulse shaping.

temporally shaped THz pulses. We use spectral correlation measurements of an unknown material with a set of shaped THz waveforms pre-designed with a priori information of the material's spectral response. For this, we have developed adaptive THz pulse shaping technique and have produced tailored THz pulses with different sensitivity to the spectral response of a given set of materials. With this new THz classification method, we demonstrate the principle of functional THz imaging by enhancing the contrast of THz images.

6.2 Femtosecond optical pulse shaping

Femtosecond pulse shaping is a technique which manipulate the temporal profile of an ultrashort pulse from a laser. Pulse shaping can be used to shorten/elongate the duration of optical pulse, or to generate more designed complex pulses. For general optical pulse shaping, three parameters are manipulated. There are three manipulation parameters: (i) the amplitude of the envelope of the laser pulse, (ii) the phase of the pulse (the instantaneous frequency inside the laser pulse) and (iii) the polarization of the lase pulse;

$$E(t) = \vec{A}(t) \exp(i\omega t + i\phi(t)). \quad (6.1)$$

In general, we can manipulate the temporal shape of the laser pulse by using the linear signal filtering method. Linear filtering in the time domain is described by

$$E_{out}(t) = E_{in}(t) \otimes h(t), \quad (6.2)$$

$$\tilde{E}_{out}(\omega) = \tilde{E}_{in}(\omega) \tilde{h}(\omega), \quad (6.3)$$

where h is the linear filter function. If we manipulate the amplitude or phase of the laser pulse in this linear scheme, we have to use use a device or material. The device or material are required to have a very fast response in femtosecond time scale. However, that is almost impossible. Alternatively, we have to find that it is a product of the spectrum with a mask function in the spectral domain to carry out a Fourier transform. This idea was presented in the 1970s [122] and Weiner *et al.* demonstrated this kind of pulse shaping for the femtosecond laser pulse using a computer controlled spatial light modulator (SLM) [123].

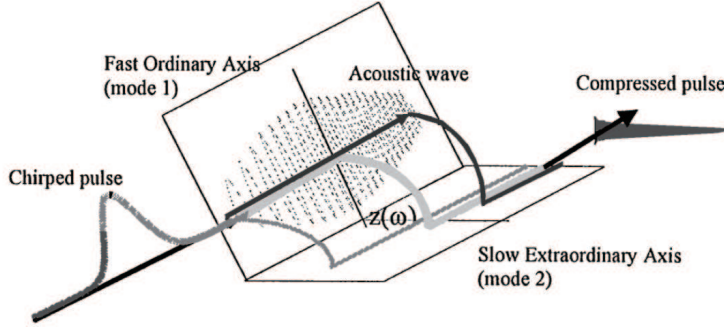


Figure 6.2: Concept diagram of the pulse shaping with an acousto-optic programmable dispersive filters [125].

6.2.1 Acousto-optic modulator

Recently, a new device based on an acousto-optic crystal was invented and it is now commercially available called acousto-optic programmable dispersive filter (AOPPDF) [124]. The AOPPDF was used in femtosecond pulse shaping [125, 126]. The AOPPDF is a single acousto-optic crystal such as TeO_2 and it has an ordinary axis and extraordinary axis in Fig. 6.2. When the original signal pulse is incident along the ordinary axis, the pulse interacts with the acoustic wave inside the crystal. If designed acoustic wave to generate a certain pulse shape is launched, diffraction occurs at some distance when the phase matching is satisfied between the \mathbf{k} vector of the light wave and the \mathbf{k} vector of the acoustic wave. Thus, the laser axis changes to the extraordinary axis. Since the group velocities are different, the total delay time depends on the position at which the spectral component diffracts inside the crystal. The alignment of AOPPDF is very simple because it is needed to combine the input pulse and acoustic wave.

The relation between the output optical pulse and the input optical pulse can be expressed with acoustic signal as [124]

$$E_{out}(t) = E_{in}(t) \otimes S(t/\alpha), \quad (6.4)$$

$$\tilde{E}_{out}(\omega) = \tilde{E}_{in}(\omega)S(\alpha\omega), \quad (6.5)$$

where the scaling factor $\alpha = \Delta n(V_a/c)$ is the ratio of the speed of sound to that of light times the difference between the refractive index of ordinary and extraordinary waves, $\Delta n = |n_e - n_o|$. Therefore, by generating a proper $S(t)$, one can achieve any desired waveform. Also, the AOPPDF can manipulate both phase and amplitude by using a single crystal. Since the repetition rate of the acoustic wave is low, the AOPPDF could not be applied to typical oscillator.

6.2.2 Liquid crystal modulator

The femtosecond optical pulse shaping with $4f$ -type pulse shaper was developed by Weiner *et al.* [109, 127]. The basic principle of $4f$ -pulse shaper is the same as as spectrometer, where the dispersed frequency components will arrive at the Fourier plane. In this Fourier plane, any desired modulation to each separated frequency component can be applied. The schematic of this grating and lens pulse-shaper is shown in Fig. 6.3. It consists of two lenses, two gratings and a modulator at the center of symmetry plane. A femtosecond pulse entering the pulse-shaper is first dispersed in space by the first grating by following an equation,

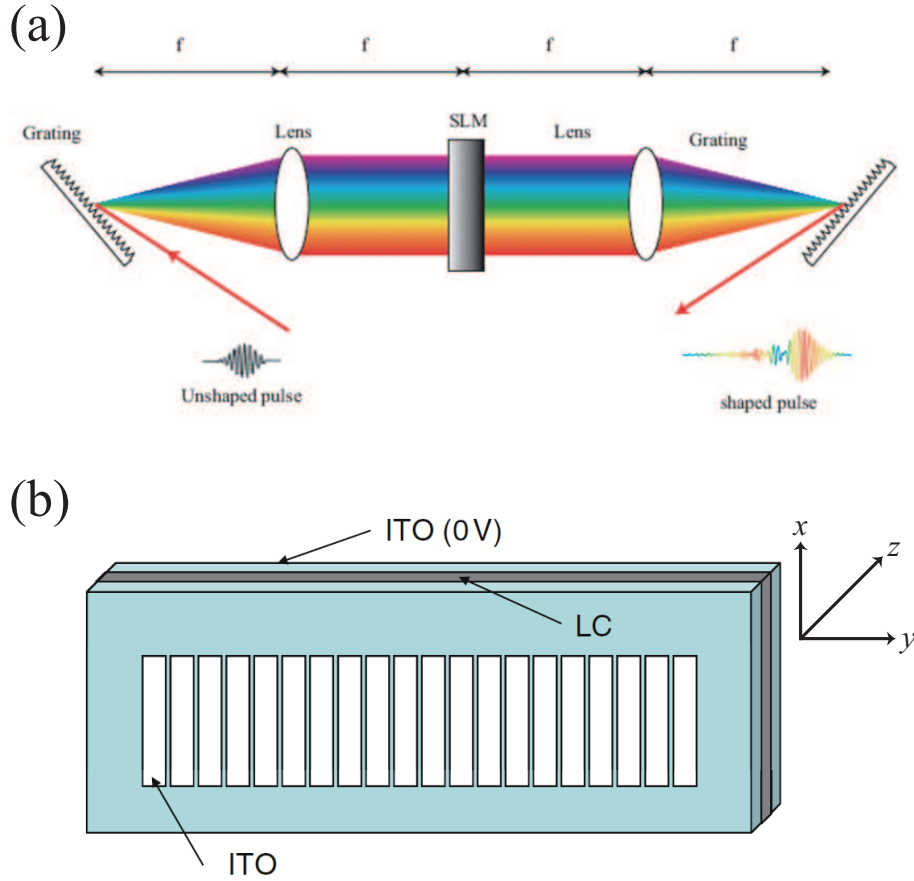


Figure 6.3: (a) $4f$ -type pulse shaper with a computer controlled spatial light modulator with two grating-lens and (b) Schematic diagram of a liquid crystal modulator.

$$\sin \theta_d(\lambda) - \sin \theta_i = \frac{\lambda}{d}, \quad (6.6)$$

where d is the grating groove period, λ is the frequency of the pulse, and $\theta_d(\lambda)$ and θ_i are the diffracted and incident angle of the beams, respectively. Here, we assume the use of order (+1) diffracted beam off the grating. The individual spectral components separated by the grating is then focused at the mask plane by a lens. At that plane, the separation between the spectral components of the pulses is at its maximum. After being modulated at the mask plane, spectral components are recombined by another lens and grating.

The output beam after the pulse-shaper has temporal profile of the Fourier transform of the filter function of the modulator, $H(\omega)$ as given in Eq. 6.7,

$$E_{out}(t) = \frac{1}{2\pi} \int d\omega e^{i\omega t} \tilde{H}(\omega) \int dt' e^{-i\omega t'} E_{in}(t'). \quad (6.7)$$

It should be noted that when there is no modulator, the output pulse is identical to the input pulse. As a modulator, both fixed masks fabricated on optical glass and programmable liquid crystal modulator arrays have been used. The programmable modulator consists of arrays of liquid crystal pixel. An electrical field manipulates the retardation for each segment and thus each segment can control each frequency mode of the ultrashort laser pulse. It has fast switching time between frames and it is also useful for low repetition rate femtosecond systems which typically involve an optical amplifier.

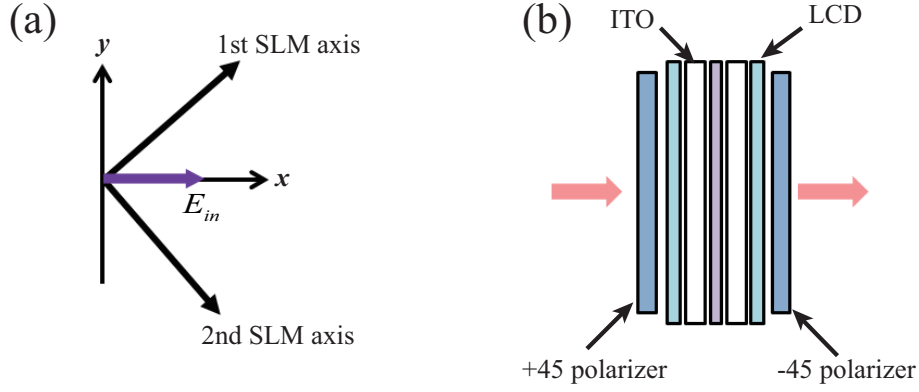


Figure 6.4: Dual modulator systems for shaping both spectral amplitude and phase. (a) Polarization of the incident laser pulse E_{in} relative to the liquid crystal axis of first and second SLM. (b) The structure of dual light modulator.

A basic liquid crystal modulator, spatial light modulator (SLM), consists of a thin layer of liquid crystal which is sandwiched between two glass slides. The inner surface of the slides are coated with transparent indium tin oxide (ITO) conducting films. An array of electrodes leaving small gap between them is lithographically patterned in the ITO at one side applying bias to individual pixels defined by the ITO electrodes. The ITO at the other side remains intact and is used as a ground plane. The molecules in the SLM are aligned to the y -direction under any zero bias. When the bias is applied, they tend to tilt to the direction of the bias field (z -direction) which is the direction of the optical beam path. When the orientation of the molecules is changed, the refractive index of the material along y -axis is changed while the refractive index along x -axis is not changed. If the y -axis polarized light passes through the SLM, the light experiences extra retardation due to the change in the refractive index. The phase-retardation of the light passing through the modulator is changed by controlling the voltage applied to the modulator array. Therefore, the phase-only modulation can be possible with a single SLM.

In general, the independent control of the phase and the amplitude modulation with a single SLM is not possible. This problem to modulate the phase and amplitude of light independently can be successfully solved by using two modulator arrays.

A schematic of a dual-SLM is shown in Figure 6.4. The dual modulator unit is positioned between two polarizers. The two light modulators are aligned to $\pm 45^\circ$ from x -axis in $x - y$ plane (the direction of light propagation is z -axis). For x -polarized light, the filter function H_n for pixel n is given by

$$\begin{aligned}
 H_n &= \frac{1}{2}[\exp(i\Delta\phi_n^{(1)}) + \exp(i\Delta\phi_n^{(2)})], \\
 &= \exp[i(\Delta\phi_n^{(1)} + \Delta\phi_n^{(2)})/2] \cos[(\Delta\phi_n^{(1)} - \Delta\phi_n^{(2)})/2],
 \end{aligned} \tag{6.8}$$

where $\Delta\phi_n^{(1)}$ and $\Delta\phi_n^{(2)}$ are the 1st and 2nd phase retardation for the modulator, respectively. The phase and amplitude can be independently controlled by By manipulating $\Delta\phi_n^{(1)}$ and $\Delta\phi_n^{(2)}$. For example, a phase only modulation is possible when $\Delta\phi^{(1)} = \Delta\phi^{(2)}$ is assumed. For an amplitude modulator, $\Delta\phi_n^{(1)} = -\Delta\phi_n^{(2)}$ is needed.

6.2.3 Phase-only Fourier-domain pulse shaping

Pulse shaper alignment

The single phase-only SLM was used in this research. The modulator was made by Cambridge Research and Instrumentation. It has 128 pixels of 5 mm height and 100 μm center-to-center separation with 2 μm gap between pixels. Operation over the range of 488–900 nm is possible. In order to use the modulator as the pulse-shaper, the relation between the phase retardation induced by SLM and the applied voltage is required for each multiple pixel element. A phase versus voltage calibration can be accomplished by using the array as an amplitude modulator for a continuous-wave laser. When the linearly polarized laser rotated 45° relative to the alignment direction of the liquid crystal passes through a liquid crystal modulator, the phase calibration is obtained by measuring the transmission through a subsequent crossed polarizer and using the relation;

$$T(V_i) = I/I_0 = \sin^2[(\phi_y(V_i) - \phi_x)/2], \quad (6.9)$$

where $T(V_i)$ is the fractional intensity transmission through the crossed polarizer, and V_i is the applied voltage on single pixel. Here ϕ_x corresponds to light polarized along the short axis of the liquid crystal molecules and is independent of the applied voltage, and $\phi_y(V_i)$ is the voltage-dependent phase.

Figure 6.5 shows the modulation and phase shift as a function of SLM drive at 775-nm continuous-wave Ti:sapphire laser. The drive level is given as a number of from 0 to 4095, with 0 corresponding to no drive voltage, and 4095 corresponding to the maximum drive voltage. In general, the relationship is:

$$V_i = \frac{D_i}{4096} \times V_{\text{ref}}, \quad (6.10)$$

where V_i is the voltage at pixel element i , and D_i is the digital drive level corresponding to that element and V_{ref} is the reference voltage, 10.0 V. Thus, drive resolution is 12 bits (2.44 mV steps). The required drive level to obtain intended phase retardation at each SLM pixel is easily estimated by using polynomial fitting for the drive level as a function of phase retardation.

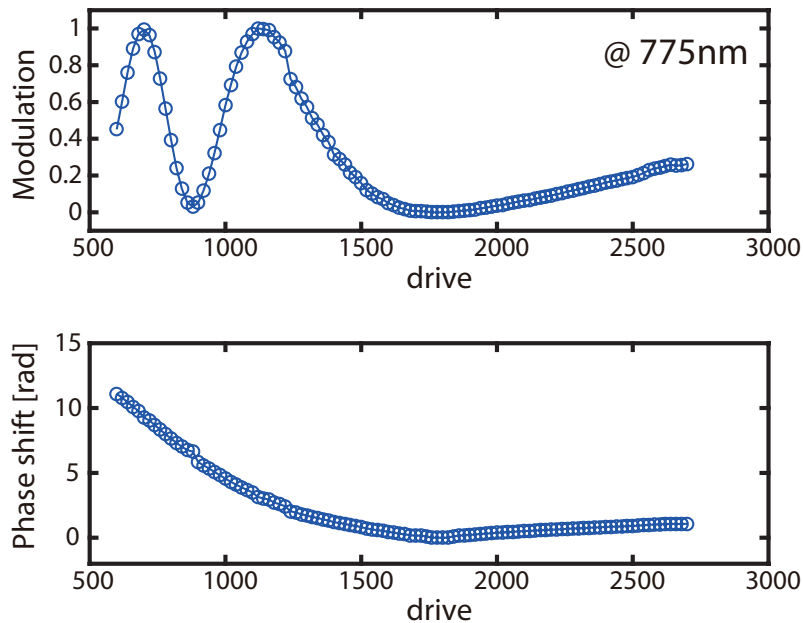


Figure 6.5: The modulation and phase shift as a function of SLM drive at 775 nm Ti:sapphire cw laser.

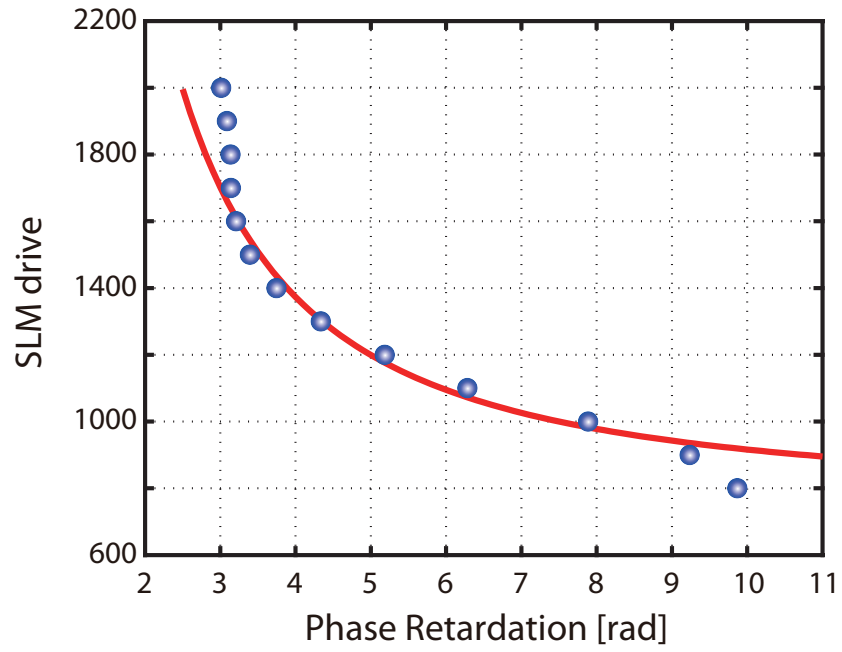


Figure 6.6: The required SLM drive as a function of intended phase retardation.

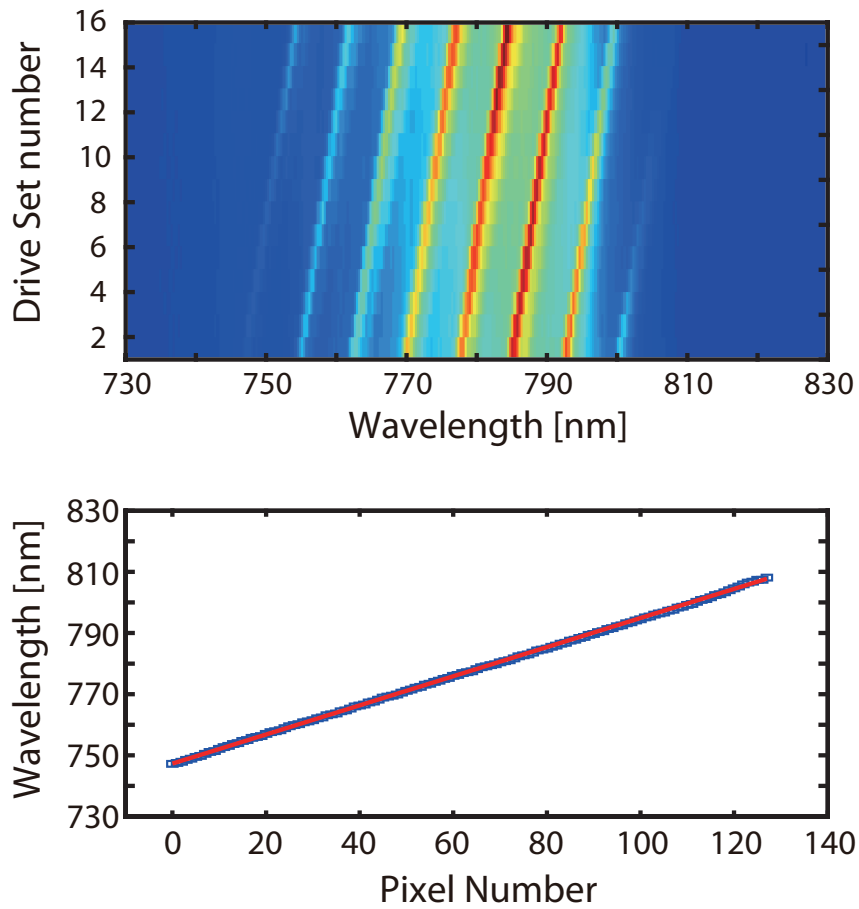


Figure 6.7: The pixel calibration map and the position of wavelength for each pixel number.

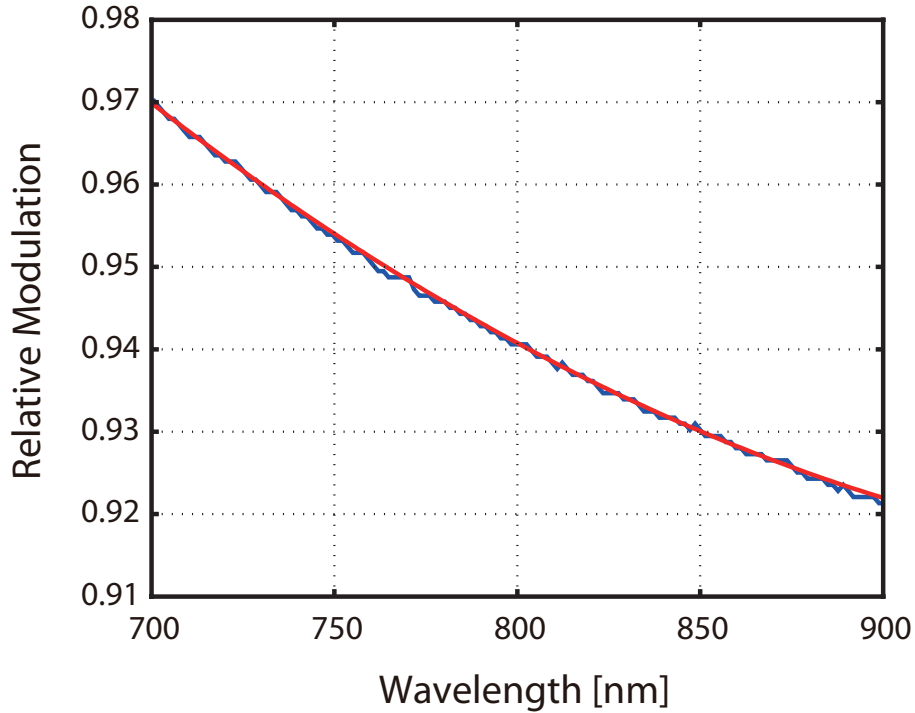


Figure 6.8: The relative modulation as a function of wavelength. The modulation is a unit at 633nm.

To determine which spectral component is focused on which pixel, the spectral components of laser pulse are spatially spread with zero dispersion expected from a grating-lens pair alignment [128]. Calibration curves for phase against drive voltage shown in Fig. 6.5 are used for finding each pixel position. Every a multiple of 8-th pixels are open and the others are blocked, which tell us an initial pixel position. After the initial determination of the peak position, the accuracy of the spectrum is improved by extrapolating the well-defined peak positions in the center of the spectrum to the less intense parts. In this way, an accurate determination of the wavelength per SLM pixel can be determined as shown in Fig. 6.7. As shown the figure, we obtain pixel calibration map. By using this figure, we obtain the position of wavelength as a function of pixel number.

For more accurate manipulation of phase retardation at other wavelength, the spectral dispersion response of liquid crystal material used in the SLM has to be considered. Figure 6.8 shows the relative modulation as a function of wavelength considering the spectral dispersion of liquid crystal. This shows the relative amount of modulation that is produced at a given wavelength, relative to what would be observed at 633 nm: $\Gamma(\lambda)/\Gamma(633\text{nm})$. After allowing for dispersion, one must further scale by wavelength λ to obtain the phase retardation in radians. Finally, separation of the frequencies that comprise the temporal pulse is achieved using a $4f$ -grating SLM pulse shaper.

If the manipulation of both spectral phase and amplitude with a SLM could be possible, the input spectrum for the target pulse are directly obtained from the laser system. The complex function of the shaping mask can be easily obtained without no ambiguity. However, the manipulation of amplitude results in the attenuation of pulse power. In order not to lose the laser pulse energy, phase-only masks are used to manipulate only the spectral phase to produce the desired output laser pulse. Numerous experiments have shown that phase-only filtering often yields an adequate match of the resultant shaped pulse intensity and target intensity profiles [129, 130, 131].

Given an input pulse spectrum and output-field target, the required complex filter mask can be

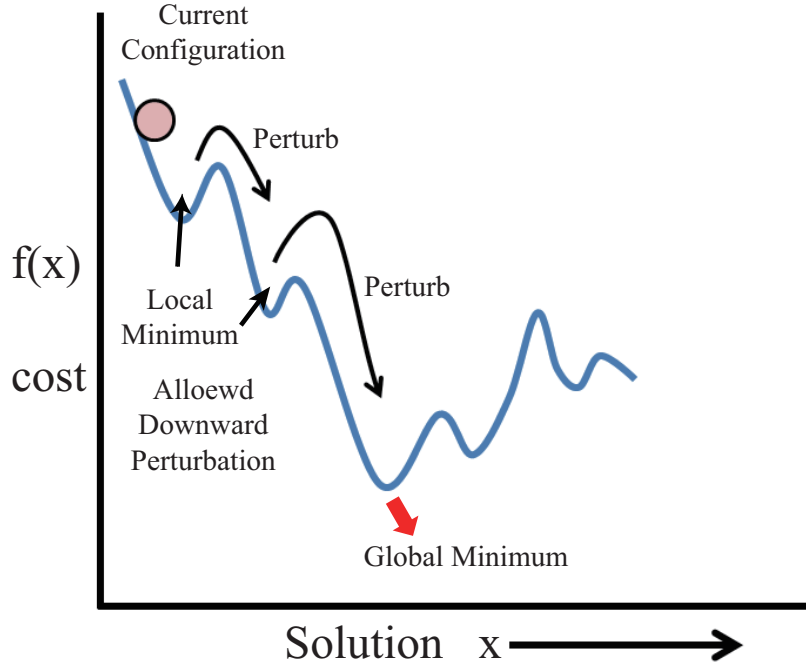


Figure 6.9: Design of phase-only shaping masks by simulated annealing algorithms.

found analytically. However if the spectral amplitude is unchanged, a solution for the phase-filter mask does not generally exist. In general, an optimal approximation of the shaped-pulse intensity profile is performed iteratively to obtain the best phase mask for the specified target. Designing an appropriate spectral phase mask typically results from the use of iterative global search algorithms with computer-assisted optimization process. There are several optimization algorithms such as simulated annealing, genetic (GA), evolutionary algorithms (EA), and Gerchberg–Saxton (GS) algorithm.

Simulated annealing shaping algorithm

The simulated-annealing method was used to design phase-only filters for producing shaped ultra-fast temporal pulses [129, 132]. Firstly, any spectral phase mask in which each pixel is randomly and independently set to a phase of 0 or π is loaded in a SLM. The minimization of C proceeds iteratively by flipping the phase of one randomly selected pixel at a time. Here, a cost function C provides a measure of the deviation between the temporal pulse shape, $E^{(i)}(t)$ generated by the phase filter $M(\omega)$ and the target pulse $E_{\text{target}}(t)$. A series of partial cost functions C_i is used to control differently generated waveform. One partial cost function could explore to minimize the maximum deviation of the generated intensity from that of the target over a specific time interval as follows:

$$C_i = \text{Max} \left| |E^{(i)}(t)|^2 - |E_{\text{target}}(t)|^2 \right|, \quad |t| < T_0. \quad (6.11)$$

The partial cost functions are weighted and summed to give the total cost function $C = \sum \omega_i C_i$. The weights ω can be chosen to permit optimization of specific features of the generated pulse, and the change in the cost function ΔC resulting from the phase change is evaluated. The new filter is always accepted if $\Delta C < 0$. For a positive ΔC , the change is accepted with the probability, $\exp(-\Delta C/T)$. The acceptance of positive ΔC with the probability could be possible to avoid settling into a local minimum of the cost function.

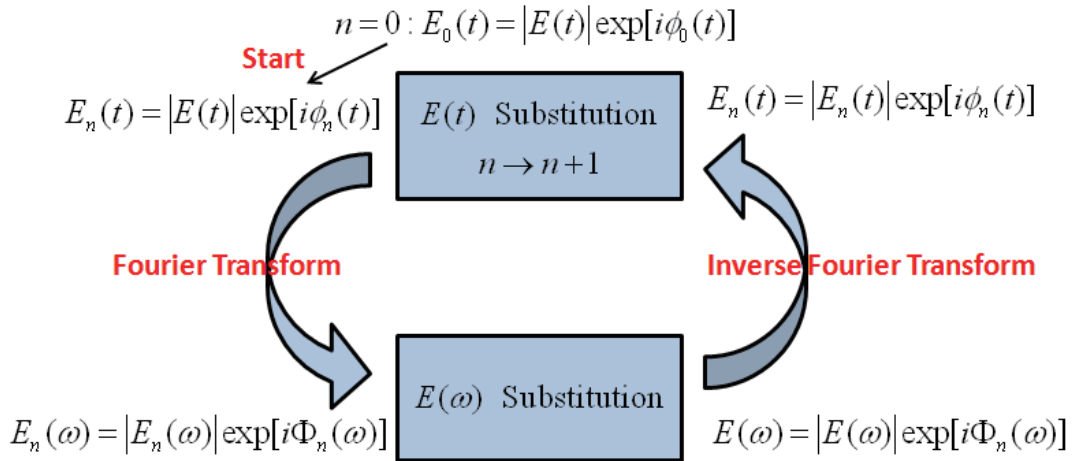


Figure 6.10: Operation of the GS algorithm. The two constraints of the problem are applied sequentially in time and frequency domains.

Gerchberg–Saxton shaping algorithm

The central application of the Gerchberg–Saxton (GS) algorithm and its modifications is found in some phase-retrieval problems: astronomy, holography, crystallography and optical shaping [131, 133]. Phase information is obtained from the intensity measurements in two conjugate Fourier domains of an image by iterating between the two [134]. The problem consists of finding a particular spectral phase function which results in a shaped temporal intensity profile as close to the target as possible. The GS algorithm makes use of the two constraints (invariants) in two conjugate domains: (i) the unaffected input pulse spectrum, and (ii) the temporal intensity target. On every iteration, the two constraints of the problem are applied sequentially in time and frequency domains.

The algorithm begins with a fast Fourier transform (FFT) of the experimentally measured intensity pulse spectrum with assumed random phase in the time domain. The amplitude is replaced with the target while the phase is unchanged. An inverse FFT back to the frequency domain is then performed in which the spectral amplitude is replaced with the input pulse spectrum and the phase is again unchanged. On the last iteration, this phase constitutes the desired phase mask. The i -th iteration can be mathematically expressed as

$$\begin{aligned} E_{(i)}(t) &= |E_{(i)}(t)| \exp[i\psi_{(i)}(t)] = \text{FFT}^{-1}\{\tilde{E}_{(i)}(\omega)\}, \\ E'_{(i)}(t) &= |E_{\text{target}}(t)| \exp[i\psi_{(i)}(t)], \end{aligned} \quad (6.12)$$

$$\begin{aligned} \tilde{E}'_{(i)}(\omega) &= |\tilde{E}'_{(i)}(\omega)| \exp[i\phi'_{(i)}(\omega)] = \text{FFT}\{E'_{(i)}(t)\} \\ E'_{(i+1)}(\omega) &= |\tilde{E}_{\text{meas}}(\omega)| \exp[i\phi_{(i+1)}(\omega)], \end{aligned} \quad (6.13)$$

where $\phi_{(i+1)}(\omega) = \phi'_{(i)}(\omega)$ is the new spectral phase, $E'_{(i)}(t)$ is an estimated target pulse, and $\tilde{E}_{(i)}(\omega)$ is an measured intensity spectrum. The use of one-dimensional FFTs decreases the converge time of the algorithm and there are no cost functions, weight factors, or parameters to optimize. In general, the algorithm converges in a few iterations although some more complicated waveforms are required for hundreds of iterations.

6.3 Experimental description

A schematic experimental diagram is shown in Fig.6.11. The experimental setup is similar to general THz spectroscopy system. The optical pulses generated by Ti:Sapphire oscillator is split into two beams. One of them inputs into the pulse shaper geometry and acts as the pump to excite a photoconductive antenna while the other is used to gate generated THz waveforms into a 2-mm thick $\langle 110 \rangle$ ZnTe [18]. For pulse shaping, we put a grating pair and spatial light modulator (SLM) in the pump beam path. The pulse shaping apparatus consists of a pair of 1800 lines/mm placed at the focal planes of a pair of cylindrical lens and a programmable liquid crystal modulator with 128 pixels at the Fourier plane of the shaper. In this Fourier plane, the spectral components of the optical pulse are spatially distributed from each other, and the frequency-dependent phase delay could be changed by controlling the refractive index of the liquid crystal at the position to set the driving voltage of each modulator element. The cross correlation, measured via second harmonic generation with BBO crystal, between shaped optical pulses and unshaped reference pulses informs the intensity profile of intended shaped optical pulses. The shaped optical pulses are focused on the transmitting photoconductive antenna. Intended THz waveforms from a photoconductive antenna are generated via spectral shaping of pump beam pulses in a phase-only pulse shaper, a programmable liquid crystal modulator. The generated THz radiation pulses are collimated and refocused by four parabolic mirrors in free space. The sampler ZnTe is used to detect the far-field radiation.

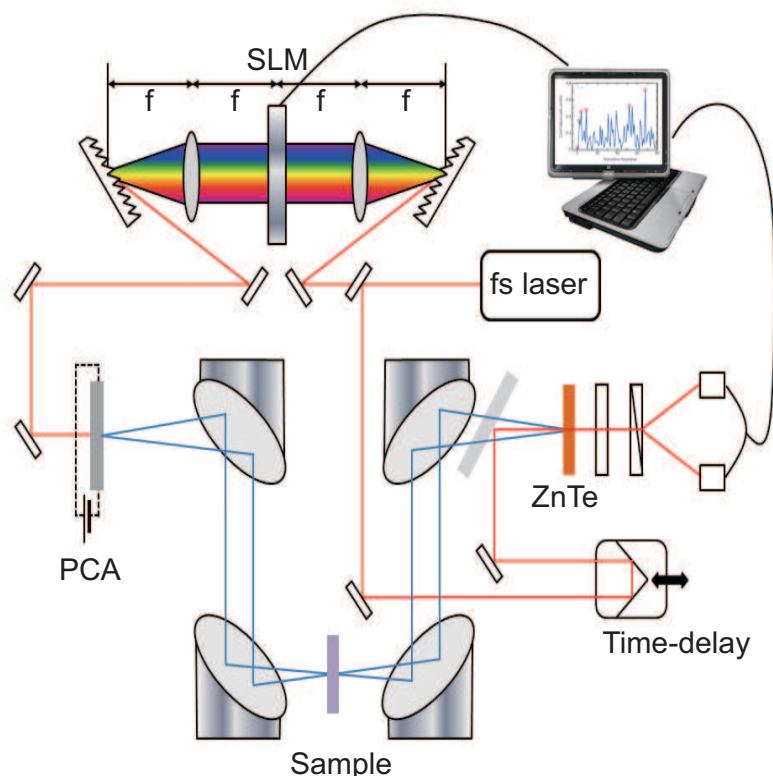


Figure 6.11: A schematic experimental diagram. A grating pair and a spatial light modulator (SLM) in the pump beam path is used for optical pulse shaping. The pulse shaping apparatus consists of a pair of 1800 lines/mm placed at the focal planes of a pair of cylindrical lens and a programmable liquid crystal modulator with 128 pixels at the Fourier plane of the shaper. The other probe beam is used to gate generated THz waveforms into the $\langle 110 \rangle$ ZnTe sampler.

6.4 Linear response function for shaped terahertz pulses

Intended THz waveforms are generated by temporally shaped optical pulses in a phase-only pulse shaper. For phase-only shaping, an approximate method is implemented by using the Gerchberg-Saxton (GS) algorithm [131]. The simplicity of the GS algorithm and its short execution time will make it possible to nearly real-time compute optimal phase profile. The phase information is obtained from the intensity measurements in two conjugate Fourier domains of an image by iterating between the two. Here, we demonstrate some examples of THz synthesis waveform via temporally different optical pulses.

The principle of THz waveform synthesis is to control the radiation field by changing the optical pulse shape. The desired optical pulse shapes are generated by a femtosecond pulse shaper and after used to excite a photoconductive antenna. The THz pulses are generated from the transient photocurrent induced by the optical pulses via optical pulse shaping. The measured THz field is given by the convolution of the optical pulse intensity and the THz system response due to the linear response.

The response function of THz system consists of the transmitter response, the propagation response function which involve the effect of frequency and geometry dependent coupling from transmitter to sampler, and the sampler response. Firstly, the radiated THz field is related to the transient photocurrent induced by the optical pulse by a frequency-dependent antenna response, $\tilde{R}_T(\omega)$. $I(t)$ is the exciting optical pulse intensity on the transmitter and $R_j(t)$ is the photocurrent response function of the transmitter under any saturation region. The radiation field can be written as

$$\tilde{E}_{rad}(\omega) = \tilde{R}_T(\omega)\tilde{R}_j(\omega)\tilde{I}(\omega). \quad (6.14)$$

When the radiated THz field propagates, the response of THz system is unified by $\tilde{P}(\omega)$. The propagation response of THz system consists of the effect of frequency and geometry dependent coupling from transmitter to sampler,

$$\tilde{E}_{pro}(\omega) = \tilde{P}(\omega)\tilde{E}_{rad}(\omega) = \tilde{P}(\omega)\tilde{R}_T(\omega)\tilde{R}_j(\omega)\tilde{I}(\omega). \quad (6.15)$$

Freely propagating THz pulses are sampled in electrooptic crystals by the measurement of the phase retardation of a near-infrared femtosecond probe pulse. In general, when no primitive phase retardation occurs in the crystal and the differential phase retardation due to THz field in $\langle 110 \rangle$ ZnTe, the total phase retardation temporarily varying spatial overlap of the probe and the THz pulses integrating over the crystal length L can be written as

$$\Gamma_{ZnTe}(t) = \frac{2\pi}{\lambda}n_0^3Lr_{41}E_{pro}(t). \quad (6.16)$$

Considering all response function of THz system, the measured THz field consists of the response function of THz system including the transmitter response, the propagation response, and the sampler response, $\tilde{R}_s(\omega)$. The measured THz field is

$$\tilde{E}_{THz}(\omega) \sim \tilde{R}_s(\omega)\tilde{P}(\omega)\tilde{R}_T(\omega)\tilde{R}_j(\omega)\tilde{I}(\omega). \quad (6.17)$$

Finally, the measured THz field in Fourier domain and temporal domain, $\tilde{E}_{THz}(\omega)$ and $E_{THz}(t)$, can be written as

$$\tilde{E}_{THz}(\omega) = \tilde{H}(\omega)\tilde{I}(\omega), E_{THz}(t) = H(t) \otimes I(t), \quad (6.18)$$

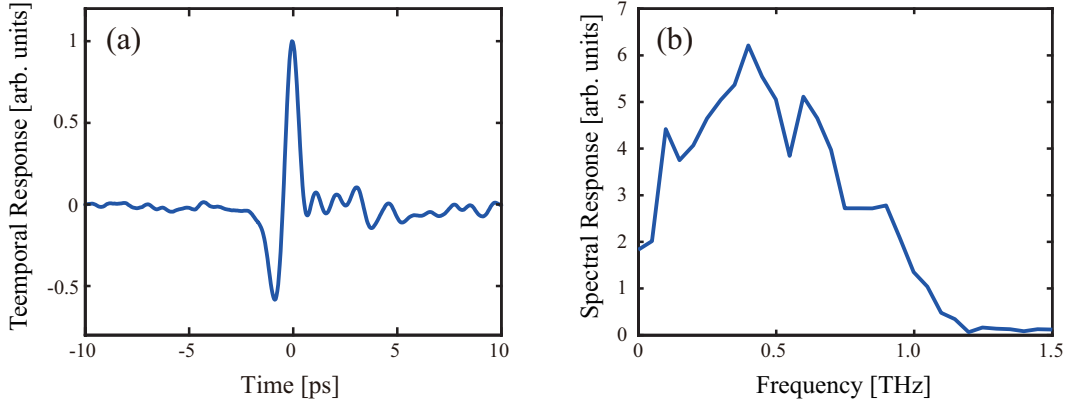


Figure 6.12: The total response functions of THz system in temporal and spectral domain, $H(t)$ and $|\tilde{H}(\omega)|$. These response functions are empirically measured by using unshaped optical pulses and used to anticipate shaped THz pulses from shaped optical pulses via phase-only pulse shaping.

where $\tilde{H}(\omega)$ and $H(t)$ are the total response functions of THz system in spectral and temporal domain, respectively. These response functions are empirically measured by using unshaped optical pulses and used to anticipate shaped THz pulses from shaped optical pulses via phase-only pulse shaping. The calculated THz waveforms from target optical pulse are shown in Fig. 6.13 and 6.14. The target optical pulse is optimized by GS algorithm.

As the first example, we demonstrate the control of temporal spacing between two optical pulses. We manipulate temporal spacing from zero to 3 ps with 1-ps step. The measured cross correlations (star) with numerical target pulses (red) are also shown in the left panel of Fig. 6.15. The temporal (middle) and spectral (right) shaped THz pulses from different two optical pulses with different temporal spacing are also shown. Also, we have shown the implementation of four different shaped optical intensity profiles and designed THz pulses with multiple peaks from one to four pulses. The cross correlation signal (left), and temporal(middle) and spectral(right) THz waveforms are shown in Fig. 6.16. All experimental results are well matched to calculation results based on total response function, $|\tilde{H}(\omega)|$.

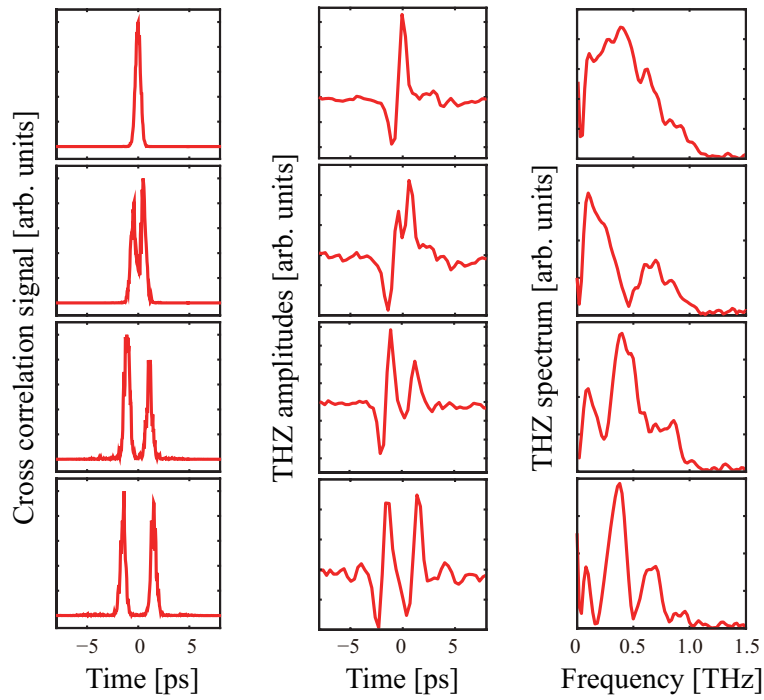


Figure 6.13: Calculated temporal (middle) and spectral (right) THz pulses from different two optical pulses with different temporal spacing.

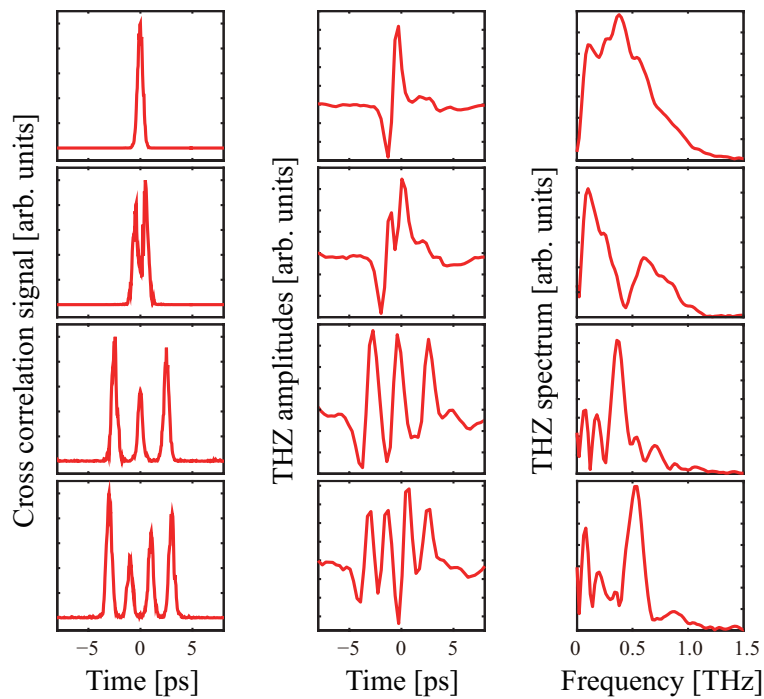


Figure 6.14: Demonstration of four different shaped optical intensity profiles and calculated THz pulses with multiple peaks from one to four pulses. The intended optical pulse (left), and temporal (middle) and spectral (right) THz waveforms are shown.

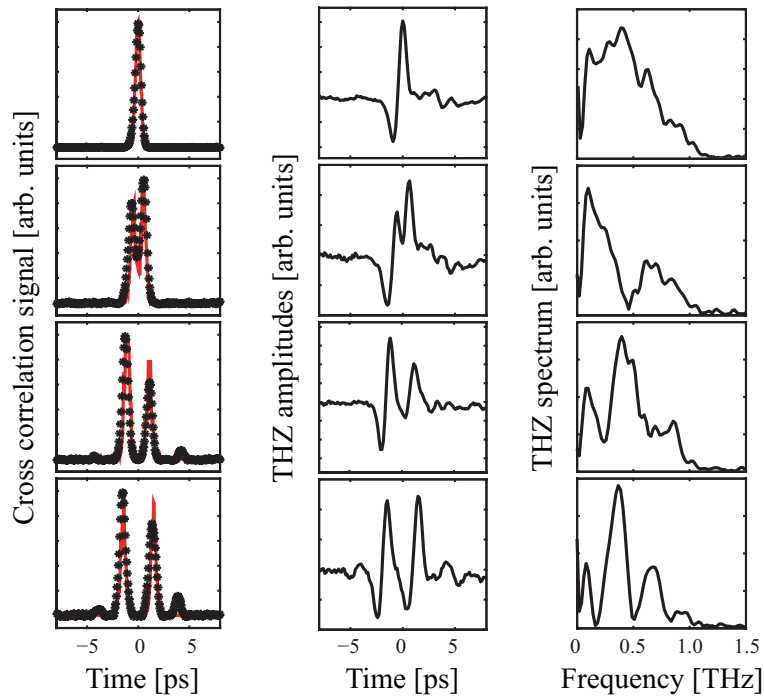


Figure 6.15: Measured temporal (middle) and spectral (right) THz pulses from different two optical pulses with different temporal spacing. The measured cross correlations (star) with numerical target pulse (red) are also shown in the left panel.

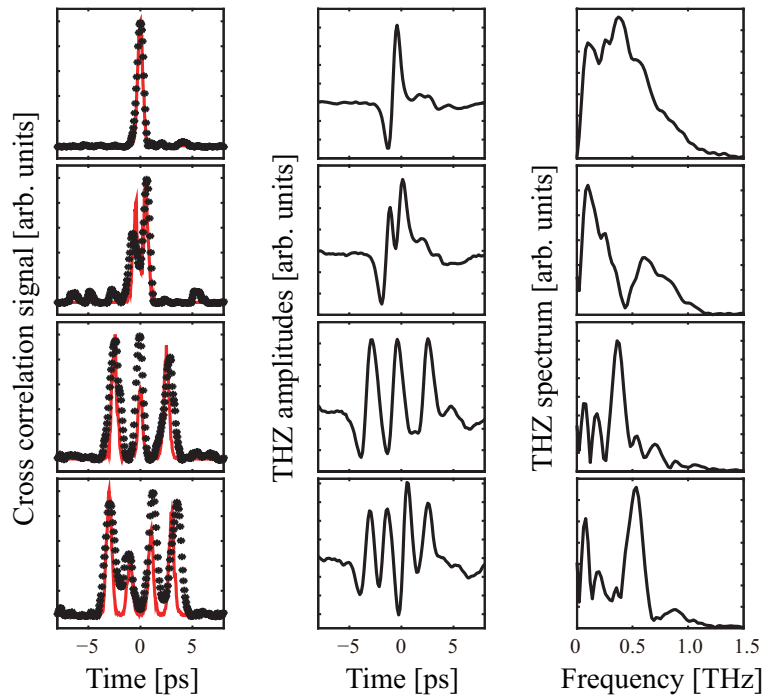


Figure 6.16: Experimental results of four different shaped optical intensity profiles and designed THz pulses with multiple peaks from one to four pulses. The cross correlation signal (left), and temporal (middle) and spectral(right) THz waveforms are shown.

6.5 Adaptive terahertz pulse shaping

We use THz pulse shaping technique to maximize the spectral correlation difference between two materials in THz frequency, where the THz spectral correlation difference $C_{1,2}(\{E(\omega)\})$ is defined, for an arbitrary THz pulse of amplitude spectral function $E(\omega)$ as

$$C_{1,2}(\{E(\omega)\}) = \int (|t_1(\omega)E(\omega)|^2 - |t_2(\omega)E(\omega)|^2) d\omega, \quad (6.19)$$

where $t_{1,2}(\omega)$ are the amplitude transmission coefficients of the materials $i = 1$ and 2 , respectively. So, a pre-designed THz waveform $E(\omega)$ which maximizes (minimizes) $C_{1,2}(\{E(\omega)\})$ is used to detect the first (the second) among the two. Likewise, this method can be generalized for a bigger set of material substances than two: Finding the i^{th} material among N different materials can be achieved by maximizing the correlation function, for example, $C_i(\{E(\omega)\})$ which is defined as

$$C_i(\{E(\omega)\}) = 2 \int |t_i(\omega)E(\omega)|^2 d\omega - \sum_{j=1}^N \int |t_j(\omega)E(\omega)|^2 d\omega, \quad (6.20)$$

where $t_i(\omega)$ is the amplitude transmission coefficient of the i^{th} material.

As the spectral correlation $C_{1,2}(\{E(\omega)\})$, or $C_i(\{E(\omega)\})$, is given linear to each spectral intensity $|E(\omega)|^2$, designing an optimal THz pulse shape $\{E(\omega)\}$ is mathematically straightforward. For example, the maximum of $C_{1,2}(\{E(\omega)\})$ in Eq. (6.19) can be obtained by maximizing the spectral intensity $|E(\omega)|^2$ for those spectral components that satisfy $|t_1(\omega)|^2 > |t_2(\omega)|^2$ and, at the same time, by minimizing $|E(\omega)|^2$ for $|t_1(\omega)|^2 < |t_2(\omega)|^2$. However, as the pulse shaping procedure of THz waveforms is indirectly processed via temporal pulse shaping of optical pulses in a phase-only shaper, there exist practical limitations to the capability of precise shaping of THz pulses. We alternatively use an adaptive search procedure for the designing optimal THz pulse shapes by sequential increasing $\Delta C_{1,2}(\{E(\omega)\})$.

An optimization method is implemented by using adaptive THz pulse shaping in a feed-back loop system. Adaptive THz pulse shaping requires a dynamic programmable pulse shaper and a feed-back THz pulse measurement. In general, an active feed-back method is used to optimize certain measurement outcome, which is the correlation in our case, that expresses the adequacy of the output pulse to achieve an intended goal. In our adaptive THz pulse shaping, the input THz pulse is given without phase modulation and the THz pulse is iteratively and adaptively modified to increase the correlation.

Experimental demonstration was performed in a THz-TDS with pulse-shaping capability. The schematic diagram for the experimental setup is shown in Fig. 6.11. We used ultrafast optical pulses generated from a Ti:sapphire mode-locked laser oscillator. The optical pulses were first pulse-shaped and then used to generate programmed THz pulses. After the transmissive response of the samples in THz frequency range was measured by the THz-TDS, the result was adaptively fed back to design a new optical pulse shape. The flow chart describing the design procedure of the optical pulses is shown in Fig. 6.17. In a more detailed explanation, the optical pulse shaping was carried out by a spatial light modulator (SLM) being placed in the Fourier plane of a $4f$ geometry Martinez zero-dispersion stretcher [128]. The SLM consisted of 128 liquid crystal pixels, and the 128 spectral phase components spanning the wavelength range between $750 \sim 810$ nm were individually changed from $-\pi$ to π . For the spectral arrangement of the optical pulses, a pair of holographic grating of 1800 lines/mm groove density were used as well as a pair of cylindrical lens of focal length of 150 mm [113]. In this Fourier plane, the spectral components of the optical pulse were spatially distributed from each other, and the frequency-dependent phase delay was changed by controlling the refractive index of the liquid crystal at

the position to set the driving voltage of each modulator element. Then, the shaped optical pulses were focused on to the transmitting photoconductive antenna to generate shaped THz pulses. The generated THz radiation pulses were then collimated and focused at the sample with a pair of off-axis parabolic mirrors, before the transmissive THz pulses were again collimated and refocused by another set of off-axis parabolic mirrors to a 2-mm thick (110) ZnTe crystal in the far-field region, where the measurement of the temporal profile of the THz pulses were carried out.

Figure 6.17 shows the optimization procedure of adaptive THz pulse shaping. We first started with the zero phase modulation, and the iteration searched for better phase-mask values which could produce optical pulses that maximized the difference between two transmitted THz signals. The optimization procedure started by setting the predetermined number of total iteration N , and by designating a zero phase delay to an initial phase-mask array $\phi^{(0)}$. In each iteration a random phase change $\Delta\phi^{(i)}$ was assigned according to

$$\Delta\phi^{(i)} = \alpha \left(1 - \frac{i}{N}\right) r, \quad (6.21)$$

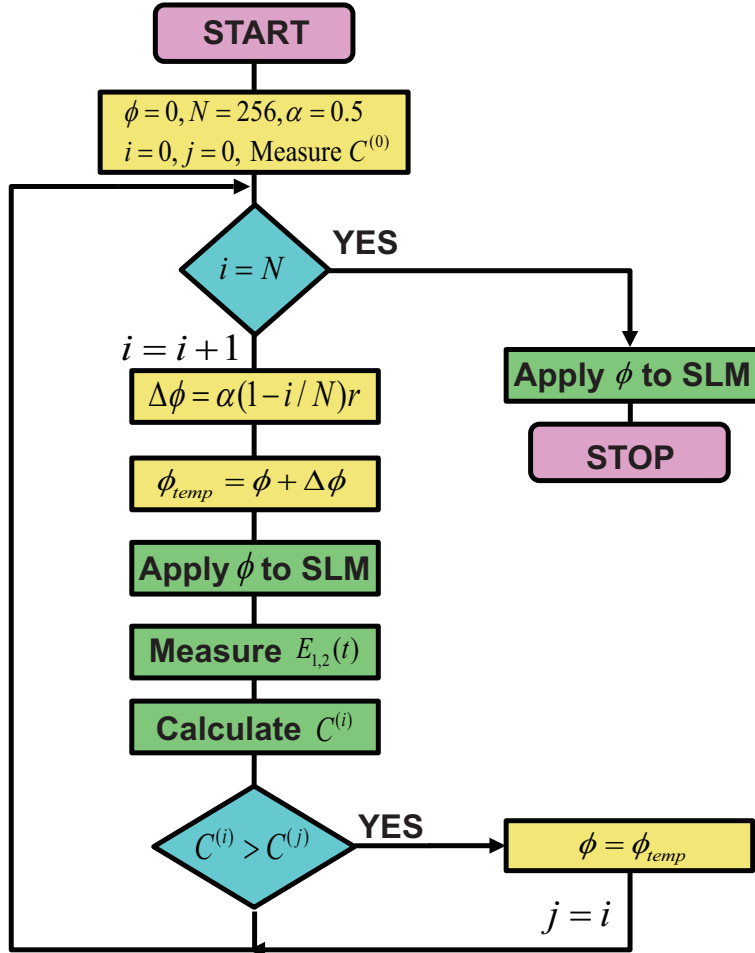


Figure 6.17: Optimization procedure for adaptive THz pulse shaping. In each iteration a random phase change array is generated and added to the current phase-mask to to optimize the spectral correlation. After the output shaped THz pulses are measured to calculate the spectral correlation, the change in the phase mask array is accepted if the correlation change is larger than that of the last accepted change, and rejected otherwise.

where i was the iteration number, r was a random variable array whose elements were randomly distributed between $-\pi$ and π , and α was an adjustable constant parameter. Every phase element was treated individually, and the both N and α were set to maximize the correlation evaluation. Then, the random phase-mask array $\Delta\phi^{(i)}$ was added to the current phase vector $\phi^{(i-1)}$ to form a new trial phase vector $\phi^{(i)}$, and this phase-mask array was applied to the liquid crystal pulse shaper to generate the shaped output THz pulses. When the output shaped THz pulse was measured, the correlation in Eq. (6.19) was calculated, and the change was accepted if the change of the correlation was positive and bigger than that of the last accepted change, and was rejected otherwise.

6.6 Shaped terahertz pulses sensitive to spectral response materials

For the test of material classification based on THz pulse shaping and correlation measurement, we chose samples of noticeable spectral feature in THz frequency range. We considered electrically resonant metamaterials (ETMs). For a brief introduction to ETMs, these dielectric and conducting materials can control the electric component of electromagnetic fields with a designed response, and have been rapidly and widely studied in recent years. In particular, among many classes of electromagnetic metamaterials, ETMs suppress the magnetic response using symmetry, and thus one can construct a purely electrically resonant response [135]. Figure 6.18 shows the design of the two ETMs (ETM1 and ETM2) and their spectral response in THz frequency range. The norm of the electric field at resonance frequency and calculated THz spectral profiles for two ETMs are displaced, where the red region in the gap indicates strong local field enhancement. As the capacitance C of ETM1 is about two-times larger than that of ETM2, while their inductance L are about the same, the resonance frequency, given as $\omega_o = 1/\sqrt{LC}$ for an RLC circuit, of ETM1 is red-shifted compared to that of ETM2. The designed resonance frequencies ETM1 and ETM1 are 0.47 and 0.77 THz, respectively as shown in Fig. 6.18(c).

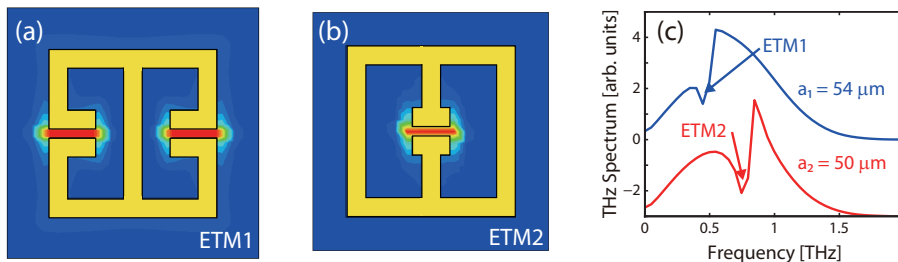


Figure 6.18: (a, b) The norm of the electric field at resonance frequency, and (c) the calculated THz spectral profiles for two ETMs. The red region in the gap indicates strong local field enhancement. ETM1 and ETM1 have the resonance characteristics at 0.47 and 0.77 THz, respectively.

We used a conventional photolithographic method to fabricate the designed ETMs in a planar array, which consisted of 150-nm-thick gold stripes with a 15-nm-thick adhesion layer of titanium on silicon substrate of 500 μm thickness. The distance of the unit cells of each ETM was tuned so that the same amount of the square sum of the transmitted unshaped THz pulse with zero phase modulation passed through the two ETMs. The absorption by ETMs is calculated by the simple description only considering absorption and transmission of THz pulses. Firstly, we measured three different THz signals for reference, $E_{\text{Si}}(t)$, and two ETMs, $E_{1,2}(t)$, with the same unit-cell distance ($a_{1,2} = 50 \mu\text{m}$). Then,

the absorption of ETMs, $A_{1,2}$, by two thin electrical resonant gold structures are simply considered that $R_0 - A_{1,2} = T_{1,2}$, where R_0 and $T_{1,2}$ are measured THz power through only silicon substrate and two ETMs which are defined by $R_0 = \int |E_{Si}(t)|^2 dt$ and $T_{1,2} = \int |E_{1,2}(t)|^2 dt$. To get similar THz power between two substances ($T'_1 \sim T_2$), the predicted unit-cell distance of ETM1 is simply calculated by $a'_1 = a_1 \sqrt{[(R_0 - T_1)/(R_0 - T'_1)]}$. The calculated THz power, T'_1 , changing a unit-cell distance of ETM1, a'_1 , is plotted as a red line in Fig. 6.19(b). Figure 6.19 shows the fabricated ETMs in (a), their power measurement of transmitted THz signals in (b), and their temporal and spectral characteristics in (c) and (d), respectively. For the incident THz pulses of perpendicular polarization, the resonance mode of each ETM is excited as shown shown in the arrow in the Fig. 6.19(a). The power of THz signals through ETM1 material is plotted in Fig. 6.19(b), measured as a function of unit-cell distance of ETM1 (a_1), which shows that with a bigger distance of the unit cell, the density of the electric resonant pattern becomes lower, and, as a result, the THz signal attenuates more. When the distance of unit cell for ETM1 and ETM2 are 54 and 50 μm , respectively, the power of measured THz signal of transmitted THz signals through the two ETMs are the same within the measurement error. Figure 6.19(c) shows the temporal characteristics of unshaped THz pulses though the ETM1 ($a_1 = 50$ and 54 μm , blue and red) and ETM2 ($a_2 = 50 \mu m$, black), respectively, and their spectral behavior in Fig. 6.19(d) confirm the electrical resonances at 0.5 and 0.8 THz for ETM1 and ETM2, respectively.

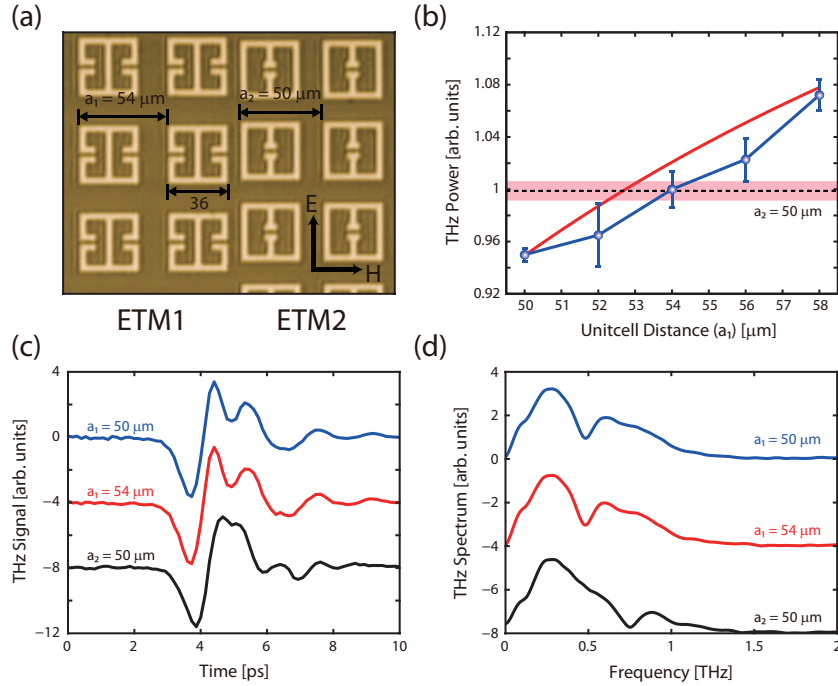


Figure 6.19: (a) The photographs of electric THz metamaterials used in this experiment. (b) The power of measured THz signals through ETM1 materials as a function of unit-cell distance of ETM1 (a_1). The unit-cell distance of ETM2 are fixed while that of ETM1 are changed to manipulate the sum of squared THz signal. By considering the measurement error, the measured power of transmitted THz signals through two ETMs are similar when the distance of unit cell for ETM1 and ETM2 are 54 and 50 μm , respectively. The temporal (c) and spectral (d) characteristics of those materials passing unshaped THz pulses for ETM1 ($a_1 = 50$ and 54 μm , blue and red) and ETM2 ($a_2 = 50 \mu m$, black). There exist electrical resonances for 0.5 (ETM1) and 0.8 THz (ETM2), respectively.

Figure 6.20(a) shows the iterative measurement of the correlation function during the optimization procedure. Among the total 80 iterations, with predetermined $N = 256$ and $\alpha = 0.5$, five times of meaningful increase in the spectral correlation are observed. If we define the evolution number as the sum of meaningful iterations when the current correlation value is larger than the previous highest correlation, as the evolution number increases, the measured correlation value increases monotonically. Figure 6.20(b) shows the normalized correlation value with the error level from the initial measurement with unshaped, plotted as a function of the evolution number. The observed correlation enhancement is about 25 times compared to the initial error level.

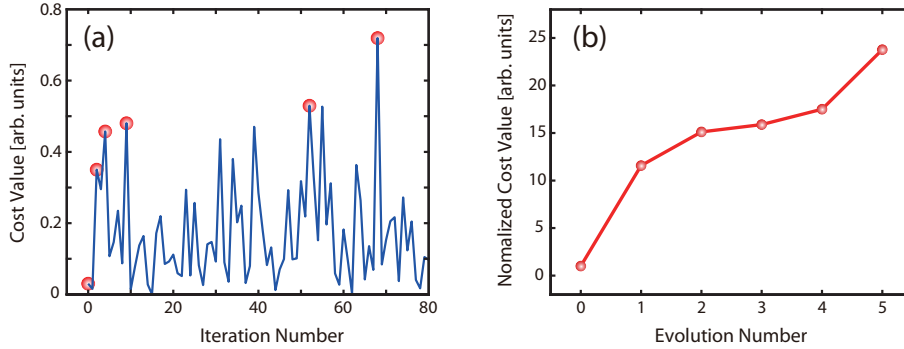


Figure 6.20: (a) The maximization of measured cost function as a function of iteration number for the optimization procedure. Circles denote the fitness values found during the optimization procedure. During the procedure, total five correlation evolution are observed. (b) The normalized correlation value divided by the initial value measured by zero phase modulation as a function of the evolution number. The observed correlation enhancement is about 25 times compared to the initial error level.

Figure 6.21 show the experimentally measured THz waveforms and their THz spectra, from the first to the fifth evolution numbers, which are generated by the adaptive THz pulse shaping. When unshaped THz pulses with zero phase modulation (the zeroth-evolution THz pulse) pass through the ETM1 and ETM2, measured THz pulses are attenuated by the resonance of ETM substances. As the evolution number increases, both the adaptively found THz waveforms and their spectra significantly change as shown in Fig. 6.21. These spectral change results in the absorption change when shaped THz pulses transmit through each ETM, which reflects the change of correlation value in each evolution generation. Therefore, the increase of correlation value makes it possible to distinguish between the two target materials. The shaped THz pulses with the third evolution phase-mask array have an interesting frequency characteristic. That is relatively more sensitive around 0.8 THz due to the absorption by ETM2. However, the sensitiveness of the absorption by ETM1 is low since the generated THz spectrum amplitude around 0.5 THz decreases. In contrast, for the fifth evolution number, the optimally shaped THz pulse generated by adaptive THz shaping method has different sensitiveness between the two ETMs. That one is highly sensitive around 0.5 THz by the attenuation and relatively nonsensitive around 0.8 THz, inversely. This last phase-mask array gives the largest correlation value, which means that the difference of measured THz powers through the two ETMs is the largest, as shown in Fig. 6.20(b).

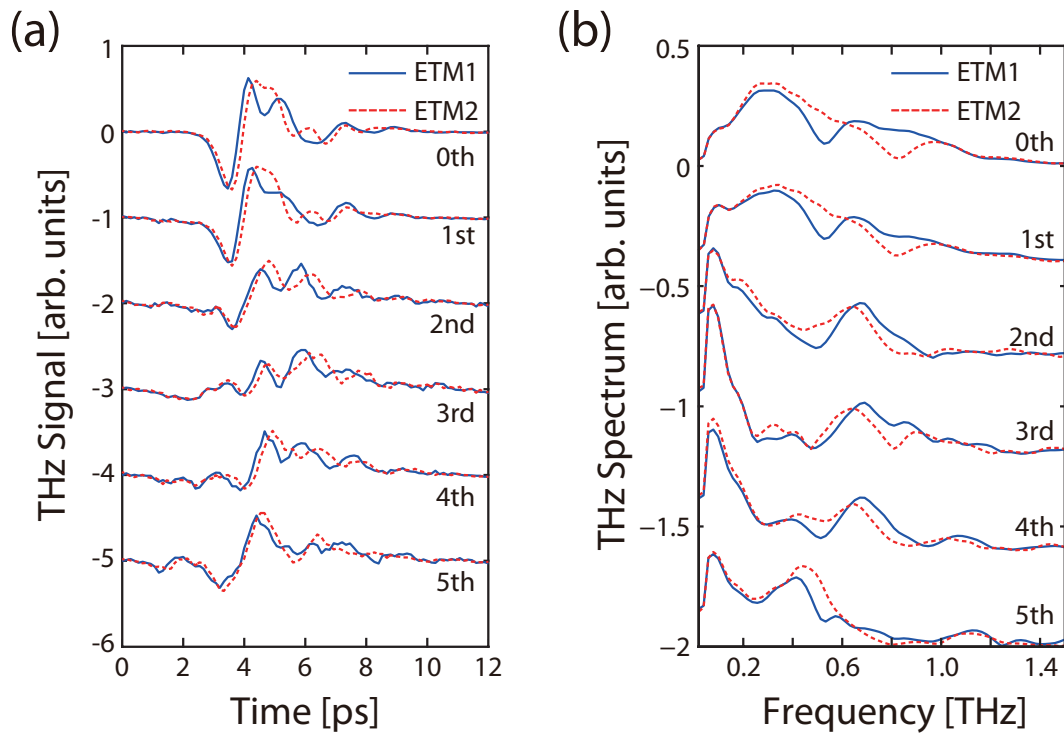


Figure 6.21: (a) Measured THz waveforms and (b) their THz spectra tailored by the adaptive THz pulse shaping from the zeroth to the fifth evolution number. With an increase in the evolution number, measured THz waveforms and spectra are significantly change. These spectral change results on the change in absorption when shaped THz pulses transmit through two ETMs. For the fifth evolution, the optimally shaped THz pulse is highly sensitive around 0.5 THz by the attenuation and relatively nonsensitive around 0.8 THz, inversely.

6.7 Terahertz spectral correlation imaging

Finally, we perform an imaging experiment with the adaptively found THz waveforms. An imaging target consists of two different THz metamaterials, where the left half circle is filled with ETM1 of 0.5 THz resonance frequency and the right half with the other with 0.8 THz as shown in Fig. 6.22(a). The figure shows the THz power imaging results with two different THz pulses for the zeroth and fifth evolution phase-mask arrays. The contrast of image with unshaped THz pulses, the zeroth-evolution THz pulses, is lower than other THz images because the amount of power absorption is similar between the two THz electrical resonant regions. The initial THz pulses has the smallest correlation value among the all evolutions. With the increase of the evolution number, the higher contrast THz power image than others is anticipated, which is clearly seen in Figs. 6.22(c). As shown the fifth-evolution phase pattern results in Fig. 6.22(c), the maximally optimized THz pulse has highly sensitive attenuation around 0.5 THz and the left half circle is dark due to the absorption by ETM1. This last phase-mask array found with the largest correlation value as shown in Fig. 6.20(b) results in the highest contrast THz image. Therefore, the two ETM regions unresolved by unshaped THz pulses are clearly distinguished as a result of adaptive THz pulse shaping. It is noted that the pulse-shaping scheme for selective substances microscopy has been previously demonstrated in optical domain, with the name of coherent control microscopy, where the non-linear nature of two-photon fluorescence has been used [136].

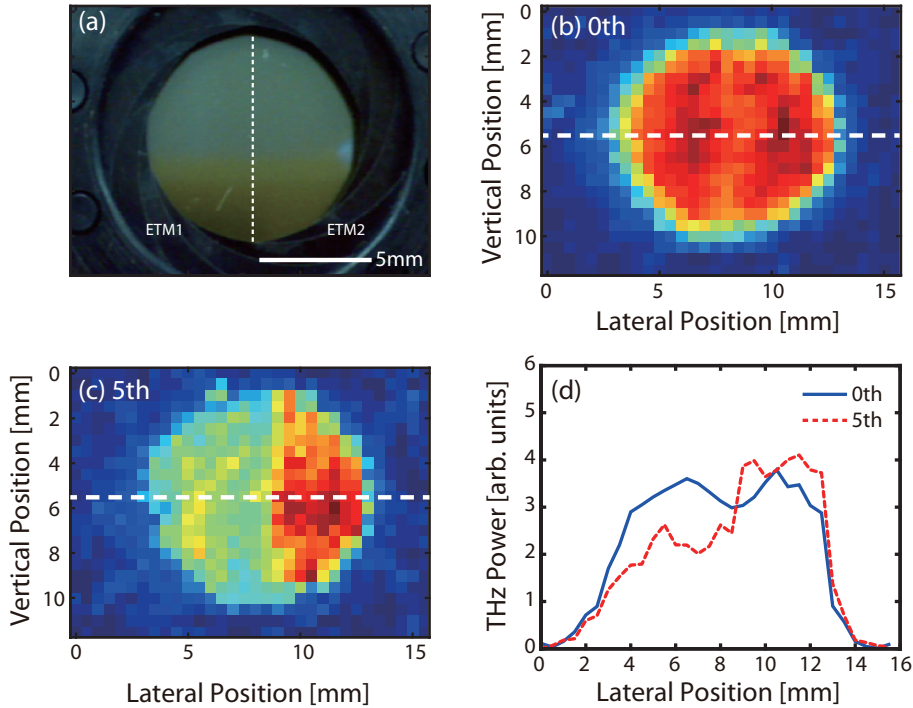


Figure 6.22: (a) An imaging target consists of two different THz metamaterials, where the left half circle is filled with ETM1 of 0.5 THz resonance frequency and the right half with the other with 0.8 THz. (b, c) Measured THz power images with different THz pulses for the zeroth- and fifth-evolution phase-mask array, respectively. A shaped THz pulse image with fifth-evolution phase pattern shows the highest contrast than others since this last phase-mask array has the largest cost value. (d) Measured THz power as function of lateral x -position at dashed line in (b) and (c). This plot shows the relative contrast of THz images for initial (0th-) and final (5th-) evolution THz pulses.

Figure 6.22(d) shows measured THz power as a function of lateral x -position at dashed line in Fig. 6.22 (b) and (c). This plot shows the relative contrast of THz images for two different THz pulses. The contrast of image with zeroth-evolution THz pulses is lower and measured THz power is similar between two different ETMs. As can be expected through Fig. 6.22(c), the maximally optimized THz pulse with fifth-evolution phase pattern, which has the highest cost function results in the THz image with highly increased contrast.

6.8 Discussion

In this chapter, we have demonstrated the usage of shaped THz pulses for functional THz imaging by using adaptively shaped THz pulses via optical pulse shaping technique. Spectral phase modulations in a spatial light pulse shaper in Fourier domain produce intentionally shaped THz pulses with different spectral characteristics. For the generation of tailored THz pulses highly sensitive to spectral response substances, the quantity of defined correlation value is compared with each iteration step. The observed correlation enhancement is about 25 times compared to the initial error level. We have also performed pulsed THz spectroscopic imaging with the adaptively found THz waveforms. The shaped THz pulse imaging system enhances the contrast of THz image since an intentionally shaped THz pulse has the sensitive attenuation to specific spectrum. It is hoped that this method could be extended to frequency-dependent functional biological and medical imaging, and nondestructive inspection in THz frequency region.

Chapter 7. Conclusion

7.1 Summary

In this dissertation, we have studied and demonstrated new methods of displaying temporal phase information of THz pulses for sub-wavelength imaging. Firstly, a semiconductor film with diffraction apertures is illuminated by ultrafast laser pulses to produce THz waves so that temporal phase advancement of THz pulses occurs when THz pulses is generated from sub-wavelength InAs emission apertures. This temporal phase shift is explained by transverse of spatial confinement of sub-wavelength THz radiation InAs thin apertures. The geometrically phase shift of radiated THz waves has been induced when the spatial frequency of the beam size is larger than k . This phase shift behavior can be applied to sensitive recognition of micrometer-size patterns smaller than the wavelength of THz pulses. The imaging results show that temporal phase difference in the time-delay domain can resolve small objects.

Secondly, we have shown a simple method of making an optical fiber emit THz waves. We have devised and demonstrated an optical-fiber THz emitter using a (100)-oriented InAs thin film placed on a 45-degree wedged optical-fiber tip. The THz wave generation mechanism from the optical-fiber tip is explained by the photo-Dember effect in a relatively low band gap semiconductor. In a proof-of-concept experiment using the alignment-free THz source for THz-TDS and THz imaging, we obtained a bandwidth of 2 THz and sub-wavelength spatial resolution. This spatial resolution is measured as 180 μm , three times smaller than the size of the optical-fiber core which is comparable $\lambda_0/2$ ($\lambda_0 = 300 \mu\text{m} = 1 \text{ THz}$). Using this method, the THz imaging resolution is expected to be improved to the size of the optical-fiber core. The designed compact THz emission tip here can be extended to near-field imaging, spectroscopy, polarization studies, and remote sensing with sub-wavelength resolution.

Additionally, we have shown the developed functional THz pulse imaging system by using intendedly shaped THz pulses via optical pulse shaping technique. Adaptively pre-designed THz pulses with the evaluation of cost function for material spectral response have enabled THz pulsed spectroscopy and imaging since spectral phase modulations in a spatial light pulse shaper on Fourier domain produce tailored THz pulses with different sensitiveness. As a result, we have acquired THz functional images by elaborately shaped THz pulses. This shaped THz pulse imaging system enhances the contrast of THz image. This developed spectroscopic and imaging method with designed THz pulses for material spectral response will rapidly enable pulsed THz spectroscopy and imaging without temporal or spectral scanning if direct THz power measurement is used.

7.2 Future work

The near-field characteristics of metamaterials and biological samples

In Chapter 3-5, we demonstrated and constructed new methods of sub-wavelength THz emission microscope system by using thin InAs film. At this stage, it will be obtained the resolution of an order of micro-meter by using above mentioned laser THz emission near-field microscope and optical-fiber THz emitter based on thin InAs film and we will study direct measurements of the electric near-field of metamaterial split ring resonators at THz frequencies using highly focused THz emission apertures. The

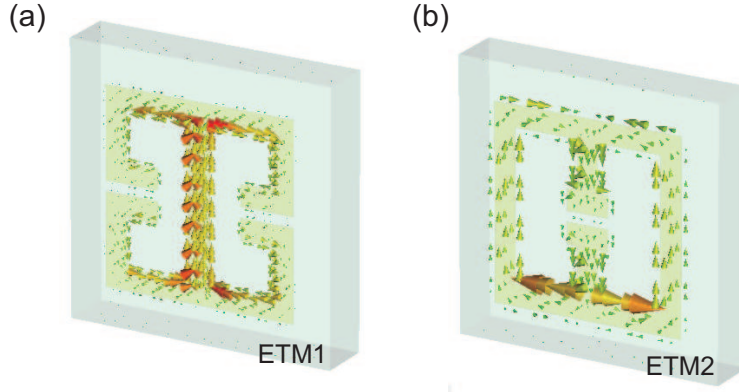


Figure 7.1: Simulation of the near-field current density distribution for THz electrical resonance materials (ETM1 and ETM2).

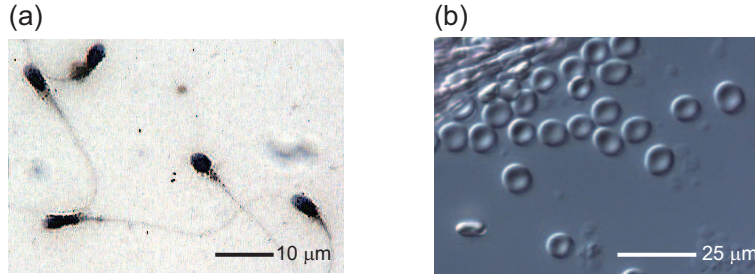


Figure 7.2: Optical microscope images of (a) sperms and (b) red blood cells (Image courtesy of University of Kansas Medical Center and Exploratorium).

frequency-dependent resonance behavior of THz metamaterials could be studied when sub-wavelength THz pulses locally excite the resonance mode of THz metamaterials. So far, artificial sub-wavelength metamaterials are mostly studied and characterized by far-field measurements. While the far-field measurement provides important information about the characteristic resonances and the macroscopic properties ϵ_{eff} and μ_{eff} , this do not provide direct insight into the formation and dynamics of the microscopic internal fields. Experimental studies of the electromagnetic near-fields in metamaterials have not been extensively studied due to the difficulties involved in measuring electric and in particular magnetic field components with the required sub-wavelength spatial resolution. We will employ sub-wavelength THz emission microscope to investigate the complex resonant characteristics of a planar metamaterial and show their localized electric and magnetic near-field response. The thin-film method provides spatially resolved measurements of the amplitude, phase and polarization of the electric field from which we show the microscopic near-field traces in a planar metamaterial at THz region. Also, we will acquire sub-wavelength THz spectroscopic imaging by the developed sub-wavelength THz emission microscope. Even with THz metamaterials, we will show that sub-wavelength THz emission microscope based on the surface of thin InAs film spatially and spectrally resolves small fragment materials and biological samples with the size of several micrometers. THz imaging of sub-wavelength biological samples e.g. sperm and red blood cell have not yet been reported. These samples has the size of several micrometers from 4 to 10 μm ($\sim \lambda/30$). The constructed thin film-InAs-based THz emission microscope in this dissertation is expected to simply simply obtain the sub-wavelength THz imaging for real target samples attaching on the back side of thin film InAs.

THz radiation from lateral dipole on the surface of thin-film semiconductor

THz emission from the surface of semiconductors is typically detected in free space. However, the radiation is generated from a dipole within a semiconductor with refractive index $n \sim 3.5$ and must be transmitted into a medium of refractive index $n_0 = 1.0$ in order to be measured. It is clear that any radiation generated outside a radiation cone of about $\theta < 17^\circ$ will be totally internally reflected by the Snell's law. The direction of radiation cone is modulated to decrease the internal reflection and increase measured radiation component by tilting the normal direction of semiconductor surface. The slanted thin InAs emitter result in the distortion of obtained THz images due to slanted angle of THz emitter. So, we will be possible to obtain sub-wavelength THz image without the distortion when the angle between femtosecond laser pulses and the normal surface of thin InAs film is zero. The lateral dipole can be created by patterning slanted metal structures on the surface of semiconductor and directly carving slanted surface in semiconductor. It can be laterally changed the distribution of photoexcited carriers by patterning slanted metal structures and carving slanted surface in semiconductor.

Liquid crystal THz phase shifter

The applications of THz spectroscopy and imaging for solid-state materials, chemicals, explosives and bio-medical samples have been explored. For these research and applications, passive optical devices such as waveplates and polarizers are required necessary components. At visible region, liquid crystal materials are widely used for signal processing, communications, tunable optical elements, and beam steering because they commonly have large birefringence and the orientation of the liquid crystals can be externally controlled by electric devices. Despite the wide application of liquid crystals in visible region, their properties in the THz region have not yet been extensively investigated. In this manner, we will investigate various liquid crystal materials using THz-TDS and find some materials with high birefringence and small absorption characteristics in THz region for the development of fast, efficient and transmissive THz liquid crystal devices. The difference phase shift for liquid crystal is calculated by the following equation;

$$\delta = 2\pi d\Delta n/\lambda, \quad (7.1)$$

where the phase shift δ , the thickness d and the birefringence (Δn) of liquid crystal are expressed for a particular wavelength λ . Therefore, a phase shift of π at 1 THz ($\lambda = 300 \mu\text{m}$) for a typical birefringence of 0.15 would require the 1-mm-thick liquid crystal layer. In comparison, the same phase shift at visible frequencies (e.g. HeNe laser, 633 nm) requires only a 2.1- μm -thick liquid crystal layer. As a result, the absorption of liquid crystal layer should be considered for THz phase modulator. Liquid crystal layer with relatively small absorption for THz region are required. With positive dielectric anisotropy, liquid crystal molecules are reoriented toward the applied electric field beyond the threshold voltage V_{th} . The threshold voltage is $V_{th} = \pi(L/d)\sqrt{k_3/\epsilon_a\epsilon_0}$, where L is the distance between two electrodes, d is the thickness of liquid crystal layer, and k_3 , $\epsilon_a = \epsilon_{\parallel} - \epsilon_{\perp}$, ϵ_0 are the bend elastic constant, dielectric anisotropy, and the vacuum permittivity, respectively. For $V > V_{th}$, the angle of liquid crystal molecules is reoriented from the original orientation along the propagation direction of the THz beam. The reoriented angle θ at any point z along the propagation direction can be calculated by using the relation [137]

$$\frac{z}{d} = \frac{V_{th}}{\pi V} \int_0^\theta \left(\frac{1 + q \sin^2 \theta}{\sin^2 \theta_m - \sin^2 \theta} \right)^{1/2} d\theta, \quad (7.2)$$

where $q = (k_1 - k_3)/k_3$ and k_1 is the splay elastic constant of liquid crystal. The angle θ_m is the maximum reorientation angle located at $z = d/2$. This equation allows us to expect the profile of liquid crystal molecular orientation in the cell for a given applied voltage.

In Chapter 6, we have demonstrated and developed the THz pulse shaping apparatus for THz spectral correlation imaging. However, shaped THz pulses are indirectly manipulated and radiated by the techniques of femtosecond optical pulse shaping. If we develop the phase modulator in THz region, we could directly radiate optimally designed THz pulses for spectral correlation. We will construct and demonstrate THz devices such as phase modulators, Fabry-Perot filters, and polarizers based on liquid crystals.

References

- [1] H. Rubens and B. W. Snow, “On the reflection of rays of great wavelength in rock salt, sylvine and fluorite,” *Phil. Mag.* **35**, 35-45 (1893).
- [2] M. F. Kimmitt, “Reststrahlen to T-Rays-100 years of terahertz radiation,” *Journal of Biological Physics* **29**, 77-85 (2003).
- [3] P. R. Smith, D. H. Auston, and M. C. Nuss, “Subpicosecond photoconducting dipole antennas,” *IEEE J. Quantum Electron.* **24**, 255-260 (1988).
- [4] T. J. Carrig, G. Rodriguez, T. Sharp Clement, A. J. Taylor, and K. R. Stewart, “Scaling of terahertz radiation via optical rectification in electro-optic crystals,” *Appl. Phys. Lett.* **66**, 121-123 (1995).
- [5] L. B. Braly, J. D. Cruzan, K. Liu, R. S. Fellers, and R. J. Saykally, “Terahertz laser spectroscopy of the water dimer intermolecular vibrations. I. (D₂O)₂,” *J. Chem. Phys.* **112**, 10293-10313 (2000).
- [6] B. B. Jin, P. Kuzel, F. Kadlec, T. Dahm, J. M. Redwing, A. V. Pogrebnyakov, X. X. Xi, and N. Klein, “Terahertz surface impedance of epitaxial MgB₂ thin film,” *Appl. Phys. Lett.* **87**, 092503 (2005).
- [7] F. N. Keutsch, M. G. Brown, P. B. Petersen, R. J. Saykally, M. Geleijns, and A. V. D. Avoird, “Terahertz vibration–rotation–tunneling spectroscopy of water clusters in the translational band region of liquid water,” *J. Chem. Phys.* **114**, 3994-4004 (2001).
- [8] K. Kawase, Y. Ogawa, Y. Watanabe, and H. Inoue, “Non-destructive terahertz imaging of illicit drugs using spectral fingerprints,” *Opt. Express* **11**, 2549-2554 (2003).
- [9] J. B. Jackson, M. Mourou, J. F. Whitaker, I. N. Duling III, S. L. Williamson, M. Menu, and G. A. Mourou, “Terahertz imaging for non-destructive evaluation of mural paintings,” *Opt. Commun.* **281**, 527-532 (2008).
- [10] B. B. Hu and M. C. Nuss, “Imaging with terahertz waves,” *Opt. Lett.* **20**, 1716-1718 (1995).
- [11] T. Löffler, T. Bauer, K. Siebert, H. Roskos, A. Fitzgerald, and S. Czasch, “Terahertz dark-field imaging of biomedical tissue,” *Opt. Express* **9**, 616-621 (2001).
- [12] H. R. Hertz, “Electric waves: being researches on the propagation of electric action with finite velocity through space,” Cornell University Library, (1893).
- [13] A. Leitenstorfer, S. Hunsche, J. Shah, M. C. Nuss, and W. H. Knox, “Femtosecond Charge Transport in Polar Semiconductors,” *Phys. Rev. Lett.* **82**, 5140–5143 (1999).
- [14] A. Dreyhaupt, S. Winnerl, T. Dekorsy, and M. Helm, “High-intensity terahertz radiation from a microstructured large-area photoconductor,” *Appl. Phys. Lett.* **86**, 121114 (2005).
- [15] M. Bass, P. A. Franken, J. F. Ward, and G. Weinreich, “Optical Rectification,” *Phys. Rev. Lett.* **9**, 446–448 (1962).

- [16] X. F. Ma and X.-C. Zhang, “Determination of ratios between nonlinear-optical coefficients by using subpicosecond optical rectification,” *J. Opt. Soc. Am. B* **10**, 1175-1179 (1993).
- [17] A. Rice, Y. Jin, X. F. Ma, X.C. Zhang, D. Bliss, J. Larkin, and M. Alexander, “Terahertz optical rectification from $\langle 110 \rangle$ zinblende crystals,” *Appl. Phys. Lett.* **64**, 1324-1326 (1994).
- [18] A. Nahata, A. S. Weling, and T. F. Heinz, “A wideband coherent terahertz spectroscopy system using optical rectification and electrooptic sampling,” *Appl. Phys. Lett.* **69**, 2321-2323 (1996).
- [19] L. Xu, X.-C. Zhang, and D. H. Auston, “Terahertz beam generation by femtosecond optical pulses in eletro-optic materials,” *Appl. Phys. Lett.* **61**, 1784-1786 (1992).
- [20] G. Chang, C. J. Divin, C.-H. Liu, S. L. Williamson, A. Galvanauskas, and T. B. Norris, “Power scalable compact THz system based on an ultrafast Yb-doped fiber amplifier,” *Opt. Express* **14**, 7909-7913 (2006).
- [21] T. J. Carrig, G. Rodriguez, T. S. Clement, A. J. Taylor, and K. R. Stewart, “Generation of terahertz radiation using electrooptic crystal mosaics,” *Appl. Phys. Lett.* **66**, 10-12 (1995).
- [22] A. M. Sinyukov, M. R. Leahy, L. M. Hayden, M. Haller, J. Luo, A. K-Y. Jen, and L. R. Dalton, “Resonance enhanced THz generation in electro-optic polymers near the absorpction maximum,” *Appl. Phys. Lett.* **85**, 5827-5826 (2004).
- [23] F. Kadlec, P. Kužel, and J.-L. Coutaz, “Optical rectification at metal surfaces,” *Opt. Lett.* **29**, 2674-2676 (2004).
- [24] T. Dekorsy, H. Auer, H. J. Bakker, H. G. Roskos, and H. Kurz, “THz electromagnetic emission by coherent infrared-active phonons,” *Phys. Rev. B* **53**, 4005–4014 (1996).
- [25] K. Liu, J. Xu, T. Yuan, and X.-C. Zhang, “Terahertz radiation from InAs induced by carrier diffusion and drift,” *Phys. Rev. B* **73**, 155330 (2006).
- [26] S. Izumida, S. Ono, Z. Liu, H. Ohtake, and N. Sarukura, “Spectrum control of THz radiation from InAs in a magnetic field by duration and frequency chirp of the excitation pulses,” *Appl. Phys. Lett.* **75**, 451-453 (1999).
- [27] D. H. Auston and M. C. Nuss, “Electrooptical generation and detection of femtosecond electrical transients,” *IEEE J. Quantum Electron.* **24**, 184-197 (1988).
- [28] A. Nahata, D. H. Auston, T. F. Heinz, and C. Wu, “Coherent detection of freely propagating terahertz radiation by electro-optic sampling,” *App. Phys. Lett.* **68**, 150–152 (1996).
- [29] P. C. Planken, H. K. Nienhuys, H. J. Bakker, and T. Wenckebach, “Measurement and calculation of the orientation dependence of terahertz pulse detection in ZnTe,” *J. Opt. Soc. Am. B* **18**, 313-317 (2001).
- [30] T. Yasui, E. Saneyoshi, and T. Araki, “Asynchronous optical sampling terahertz time-domain spectroscopy for ultrahigh spectral resolution and rapid data acquisition,” *Appl. Phys. Lett.* **87**, 061101 (2005).

- [31] A. Bartels, R. Cerna, C. Kistner, A. Thoma, F. Hudert, C. Janke, and T. Dekorsy, “Ultrafast time-domain spectroscopy based on high-speed asynchronous optical sampling,” *Rev. Sci. Instrum.* **78**, 035107 (2007).
- [32] Y. Kim, D.-S. Yee, M. Yi, and J. Ahn, “High-Speed High-Resolution Terahertz Spectrometers,” *J. Kor. Phys. Soc.* **56**, 255-261 (2010).
- [33] D. H. Auston, K. P. Cheung, J. A. Valdmanis, and D. A. Kleinman, “Cherenkov Radiation from Femtosecond Optical Pulses in Electro-Optic Media,” *Phys. Rev. Lett.* **53**, 1555–1558 (1984).
- [34] Ch. Fattinger and D. Grischkowsky, “Point source terahertz optics,” *Appl. Phys. Lett.* **53**, 1480-1482 (1988).
- [35] N. Sarukura, H. Ohtake, S. Izumida, and Z. Liu, “High average-power THz radiation from femtosecond laser-irradiated InAs in a magnetic field and its elliptical polarization characteristics,” *J. Appl. Phys.* **84**, 654-656 (1998).
- [36] M. Migita and M. Hangyo, “Pump-power dependence of THz radiation from InAs surfaces under magnetic fields excited by ultrashort laser pulses,” *Appl. Phys. Lett.* **79**, 3437-3439 (2001).
- [37] M. Levinstein, S. Rumyantsev, and M. Shur, *Handbook Series on Semiconductor Parameters*, World Scientific, London, 1996).
- [38] <http://www.ioffe.rssi.ru/SVA/NSM/Semicond/>
- [39] X. C. Zhang, Y. Jin, K. Ware, X. F. Ma, A. Rice, D. Bliss, J. Larkin, and M. Alexander, “Difference-frequency generation and sum-frequency generation near the band gap of zincblende crystals,” *Appl. Phys. Lett.* **64**, 622-624 (1994).
- [40] P. Gu, M. Tani, S. Kono, K. Sakai, and X.-C. Zhang, “Study of terahertz radiation from InAs and InSb,” *J. Appl. Phys.* **91**, 5533-5537 (2002).
- [41] X. C. Zhang and D. H. Auston, “Optoelectronic measurement of semiconductor surfaces and interfaces with femtosecond optics,” *J. Appl. Phys.* **71**, 326-338 (1992).
- [42] M. B. Johnston, D. M. Whittaker, A. Corchia, A. G. Davies, and E. H. Linfield, “Simulation of terahertz generation at semiconductor surfaces,” *Phys. Rev. B* **65**, 1653011 (2002).
- [43] S. Kono, P. Gu, M. Tani and K. Sakai, “Temperature dependence of terahertz radiation from *n*-type InSb and *n*-type InAs surfaces,” *Appl. Phys. B* **71**, 901-904 (2000).
- [44] W. Mönch, *Semiconductor surfaces and interfaces* (Springer, Berlin, 3rd. 2001).
- [45] T. S. Hartwick, D. T. Hodges, D. H. Barker, and F. B. Foote, “Far infrared imagery,” *Appl. Opt.* **15**, 1919-1922 (1976).
- [46] E. Budiarto, N.-W. Pu, S. Jeong, and J. Bokor, “Near-field propagation of terahertz pulses from a large-aperture antenna,” *Opt. Lett.* **23**, 213-215 (1998).
- [47] S. Hunsche, M. Koch, I. Brener, and M. C. Nuss, “THz near-field imaging,” *Opt. Commun.* **150**, 22–26 (1998).

- [48] D. Courjon, *Near-Field Microscopy and Near-Field Optics* (World Scientific Publishing Company, 2003).
- [49] B. T. Rosner, D. W. van der Weide, “High-frequency near-field microscopy,” *Rev. Sci. Instrum.* **73**, 2505-2525 (2002).
- [50] H. A. Bethe, “Theory of diffraction by small holes,” *Phys. Rev.* **66**, 163–182 (1944).
- [51] O. Mitrofanov, I. Brener, R. Harel, J. D. Wynn, L. N. Pfeiffer, K. W. West, and J. Federici, “Terahertz near-field microscopy based on a collection mode detector,” *Appl. Phys. Lett.* **77**, 3496–3498 (2000).
- [52] S. Mair, B. Gompf, and M. Dressel, “Spatial and spectral behavior of the optical near field studied by a terahertz near-field spectrometer,” *Appl. Phys. Lett.* **84**, 1219-1221 (2004).
- [53] F. Keilmann, “FIR microscopy,” *Infrared Physics & Technology* **36**, 217-224 (1995).
- [54] U. Schade, K. Holldack, P. Kuske, G. Wustefeld, and H. Hubers, “THz near-field imaging employing synchrotron radiation,” *Appl. Phys. Lett.* **84**, 1422–1424 (2004).
- [55] G. Staats, L. Fernandez, K. Holldack, U. Schade, and D. Schondelmaier, “Coupling structures for terahertz near-field microspectroscopy,” *Infrared Physics & Technology* **49**, 122-127 (2006).
- [56] E. A. Ash and G. Nicholls, “Super-resolution aperture scanning microscope,” *Nature (London)* **237**, 510–512 (1972).
- [57] N. Klein, P. Lahl, U. Poppe, F. Kadlec, and P. Kužel, “A metal-dielectric antenna for terahertz near-field imaging,” *J. Appl. Phys.* **98**, 014910 (2005); M. Berta, *Development and applications of near-field imaging methods in the terahertz spectral domain* (Charles University in Prague, 2011).
- [58] M. M. Awad and R. A. Cheville, “Transmission terahertz waveguide-based imaging below the diffraction limit,” *Appl. Phys. Lett.* **86**, 221107 (2005).
- [59] M. Wächter, M. Nagel, and H. Kurz, “Tapered photoconductive terahertz field probe tip with subwavelength spatial resolution,” *Appl. Phys. Lett.* **95**, 041112 (2009).
- [60] H. Chen, R. Kersting, and G. C. Cho, “Terahertz imaging with nanometer resolution,” *Appl. Phys. Lett.* **83**, 3009–3011 (2003).
- [61] G. C. Cho, H. Chen, S. Kraatz, N. Karpowicz, and R. Kersting, “Apertureless terahertz near-field microscopy,” *Semiconductor Science and Technology* **20**, S286–S292 (2005).
- [62] F. Buergens, R. Kersting, and H. Chen, “Terahertz microscopy of charge carriers in semiconductors,” *Appl. Phys. Lett.* **88**, 112115 (2006).
- [63] F. Buergens, G. Acuna, C. H. Lang, S. I. Potrebic, S. Manus, and R. Kersting, “Shear force control for a terahertz near field microscope,” *Rev. Sci. Instrum.* **78**, 113701 (2007).
- [64] A. J. Huber, F. Keilmann, J. Wittborn, J. Aizpurua, and R. Hillenbrand, “Terahertz near-field nanoscopy of mobile carriers in single semiconductor nanodevices,” *Nano Letters* **8**, 3766–3770 (2008).

- [65] M. Awad, M. Nagel, and H. Kurz, “Tapered Sommerfeld wire terahertz near-field imaging,” *Appl. Phys. Lett.* **94**, 051107 (2009).
- [66] K. Wang, A. Barkan, and D. M. Mittleman, “Propagation effects in apertureless near-field optical antennas,” *Appl. Phys. Lett.* **84**, 305-307 (2004).
- [67] P. C. M. Planken and N. C. J. van der Valk, “Spot-size reduction in terahertz apertureless near-field imaging,” *Opt. Lett.* **29**, 2306-2308 (2004).
- [68] K. Wynne and D. Jaroszynski, “Superluminal terahertz pulses,” *Opt. Lett.* **24**, 25-27 (1999).
- [69] R. Lecaque, S. Gresillon, and C. Boccara, “THz emission microscopy with sub-wavelength broadband source,” *Opt. Express* **16**, 4731-4738 (2008).
- [70] T. Kiwa, M. Tonouchi, M. Yamashita, and K. Kawase, “Laser terahertz-emission microscope for inspecting electrical faults in integrated circuits,” *Opt. Lett.* **28**, 2058-2060 (2003).
- [71] A. J. L. Adam, J. M. Brok, M. A. Seo, K. J. Ahn, D. S. Kim, J. H. Kang, Q. H. Park, M. Nagel, and P. C. M. Planken, “Advanced terahertz electric near-field measurements at sub-wavelength diameter metallic apertures,” *Opt. Express* **16**, 7407-7419 (2008).
- [72] G. Veshapidze, M. L. Trachy, M. H. Shah, and B. D. DePaola, “Reducing the uncertainty in laser beam size measurement with a scanning edge method,” *Appl. Opt.* **45**, 8197-8199 (2006).
- [73] X. Wang, Y. Cui, D. Hu, W. Sun, J. Ye, and Y. Zhang, “Terahertz quasi-near-field real-time imaging,” *Opt. Comm.* **282**, 4683-4687 (2009).
- [74] M. Yi, K. Lee, J. Lim, Y. Hong, Y.-D. Jho, and J. Ahn, “Terahertz Waves Emitted from an Optical Fiber,” *Opt. Express* **18**, 13693-13699 (2010).
- [75] M. van Exter and D. Grischkowsky, “Optical and Electronic Properties of Doped Silicon from 0.1 to 2 THz,” *Appl. Phys. Lett.* **56**, 1694-1696 (1990).
- [76] Y.-S. Lee, *Principles of Terahertz Science and Technology* (Springer, New York, USA, 2009).
- [77] W. L. Chan, J. Deibel, D. M. Mittleman, “Imaging with terahertz radiation,” *Rep. Prog. Phys.* **70**, 1325-1379 (2007).
- [78] X.-C. Zhang, “Three-dimensional terahertz wave imaging,” *Phil. Trans. R. Soc. Lond. A* **362**, 283-299 (2004).
- [79] K. McClatchey, M. T. Reiten, and R. A. Cheville, “Time Resolved synthetic aperture terahertz impulse imaging,” *Appl. Phys. Lett.* **79**, 4485-4487 (2001).
- [80] K. Lee, K. H. Jin, J. C. Ye, and J. Ahn, “Coherent Optical Computing for T-ray Imaging,” *Opt. Lett.* **35**, 508-510 (2010).
- [81] K. Lee and J. Ahn, “Single Pixel Coherent Diffraction Imaging,” *Appl. Phys. Lett.* **97**, 241101 (2010).
- [82] F. Zernike, “Beugungstheorie des Schneidenverfahrens und seiner verbesserten Form, der Phasenkontrastmethode,” *Physica* **1**, 689-704 (1934).

- [83] D. Paganin and K. A. Nugent, “Non-interferometric phase imaging with partially coherent light,” *Phys. Rev. Lett.* **80**, 2586-2589 (1998).
- [84] E. D. Barone-Nugent, A. Barty, K. A. Nugent, “Quantitative phase-amplitude microscopy I: optical microscopy,” *J. of Microscopy* **206**, 194-203 (2002).
- [85] Y. Wang, Z. Zhao, Z. Chen, L. Zhang, K. Kang, J. Deng, “Continuous-wave terahertz phase imaging using a far-infrared laser interferometer,” *Appl. Opt.* **50**, 6452-6460 (2011)
- [86] S. Feng and H. G. Winful, “Physical origin of the Gouy phase shift,” *Opt. Lett.* **26**, 485-487 (2001).
- [87] A. B. Ruffin, J. V. Rudd, J. F. Whitaker, S. Feng, and H. G. Winful, “Direct Observation of the Gouy Phase Shift with Single-Cycle Terahertz Pulses,” *Phys. Rev. Lett.* **83**, 3410–3413 (1999).
- [88] Oleg Mitrofanov, M. Lee, J. W. P. Hsu, L. N. Pfeiffer, K. W. West, J. D. Wynn, and J. F. Federici, “Terahertz pulse propagation through small apertures,” *Appl. Phys. Lett.* **79**, 907-909 (2001).
- [89] Q. Chen, Z. Jiang, G. X. Xu, and X.-C. Zhang, “Near-field terahertz imaging with a dynamic aperture,” *Opt. Lett.* **25**, 1122-1124 (2000).
- [90] A. J. L. Adam, N. C. J. Van der Valk, and P. C. M. Planken, “Measurement and calculation of the near field of a terahertz apertureless scanning optical microscope,” *J. Opt. Soc. Am. B* **24**, 1080-1090 (2007).
- [91] J. Bromage, S. Radic, G. P. Agrawal, C. R. Stroud, P. M. Fauchet, and R. Sobolewski, “Spatiotemporal shaping of half-cycle terahertz pulses by diffraction through conductive apertures of finite thickness,” *J. Opt. Soc. Am. B* **15**, 1399-1405 (1988).
- [92] N. C. J. van der Valk and P. C. M. Planken, “Electro-optic detection of subwavelength terahertz spot sizes in the near field of a metal tip,” *Appl. Phys. Lett.* **81**, 1558-1560 (2002).
- [93] K. Wang and D. M. Mittleman, “Metal wires for terahertz wave guiding,” *Nature (London)* **432**, 376-379 (2004).
- [94] A. Bingham, Y. Zhao, and D. Grischkowsky, “THz parallel plate photonic waveguides,” *Appl. Phys. Lett.* **87**, 051101 (2005).
- [95] S. P. Jamison, R.W. McGowan, and D. Grischkowsky, “Single-mode waveguide propagation and reshaping of sub-ps terahertz pulses in sapphire fibers,” *Appl. Phys. Lett.* **76**, 1987-1989 (2000).
- [96] L.-J. Chen, H.-W. Chen, T.-F. Kao, J.-Y. Lu, and C.-K. Sun, “Low-loss subwavelength plastic fiber for terahertz waveguiding,” *Opt. Lett.* **31**, 308-310 (2006).
- [97] T.-I. Jeon, and D. Grischkowsky, “Direct optoelectronic generation and detection of sub-ps-electrical pulses on sub-mm-coaxial transmission lines,” *Appl. Phys. Lett.* **85**, 6092-6094 (2004).
- [98] M. Mbonye, R. Mendis, and D. M. Mittleman, “A terahertz two-wire waveguide with low bending loss,” *Appl. Phys. Lett.* **95**, 233506 (2009).
- [99] S. A. Crooker, “Fiber-coupled antennas for ultrafast coherent terahertz spectroscopy in low temperatures and high magnetic fields,” *Rev. Sci. Instrum.* **73**, 3258-3264 (2002).

- [100] R. Adomavičius, A. Urbanowicz, G. Molis, A. Krotkus, and E. Šatkovskis, “Terahertz emission from p-InAs due to the instantaneous polarization,” *Appl. Phys. Lett.* **85**, 2463-2465 (2004).
- [101] J. R. Higgins, *Sampling Theory in Fourier and Signal Analysis: Vol. 1: Foundations* (Oxford University Press, USA, 1996)
- [102] A. M. Weiner, J. P. Heritage, and J. A. Salehi, “Encoding and decoding of femtosecond pulses,” *Opt. Lett.* **13**, 300-302 (1988).
- [103] R. Bartels, S. Backus, E. Zeek, L. Misoguti, G. Vdovin, I. P. Christov, M. M. Murnane, and H. C. Kapteyn, “Shaped pulse optimization of coherent emission of high-harmonic soft X-rays,” *Nature (London)* **406**, 164–166 (2000).
- [104] D. Meshulach and Y. Silberberg, “Coherent quantum control of two-photon transitions by a femtosecond laser pulse,” *Nature (London)* **396**, 239-242 (1998).
- [105] S. Lee, J. Lim, J. Ahn, V. Hakobyan, and S. Guerin, “Strong-field two-level two-photon transition by phase shaping,” *Phys. Rev. A* **82**, 023408 (2010).
- [106] J. Lim, H.-g. Lee, S. Lee, and J. Ahn, “Quantum control in two-dimensional Fourier transform spectroscopy,” *Phys. Rev. A* **84**, 013425 (2011).
- [107] J. Ahn, D. N. Hutchinson, C. Rangan, and P. H. Bucksbaum, “Quantum Phase Retrieval of a Rydberg Wave packet using a Half-cycle Pulse,” *Phys. Rev. Lett.* **86**, 1179-1182 (2001).
- [108] D. Weidinger and M. Gruebele, “Simulations of quantum computation with a molecular ion,” *Chem. Phys.* **350**, 139–144 (2008).
- [109] A. M. Weiner, D. E. Leaird, G. P. Wiederrecht, and K. A. Nelson, “Femtosecond pulse sequences used for optical manipulation of molecular motion,” *Science* **247**, 1317-1319 (1990).
- [110] I. Brener, P. C. M. Planken, M. C. Nuss, L. Pfeiffer, D. E. Leaird, and A. M. Weiner, “Repetitive excitation of charge oscillations in semiconductor heterostructures,” *Appl. Phys. Lett.* **63**, 2213–2215 (1993).
- [111] P. C. M. Planken, I. Brener, M. C. Nuss, M. S. C. Luo, and S. L. Chuang, “Coherent control of terahertz charge oscillations in a coupled quantum well using phase-locked optical pulses,” *Phys. Rev. B* **48**, 4903-4906 (1993).
- [112] T. Feurer, J. C. Vaughan, and K. A. Nelson, “Spatiotemporal coherent control of lattice vibrational waves,” *Science* **299**, 374-377 (2003).
- [113] J. Ahn, A. Efimov, R. Averitt, and A. Taylor, “Terahertz waveform synthesis via optical rectification of shaped ultrafast laser pulses,” *Opt. Express* **11**, 2486-2496 (2003).
- [114] K. K. Kohli, A. Vaupel, S. Chatterjee, and W. W. Rühle, “Adaptive shaping of THz-pulses generated in <110> ZnTe crystals,” *J. Opt. Soc. Am. B* **26**, A74-A78 (2009).
- [115] S. Vidal, J. Degert, J. Oberlè, and E. Freysz, “Femtosecond optical pulse shaping for tunable terahertz pulse generation,” *J. Opt. Soc. Am. B* **27**, 1044-1050 (2010).

- [116] M. Yi, K. Hee Lee, I. Maeng, J.-H. Son, R. D. Averitt, and J. Ahn, "Tailoring the Spectra of Terahertz Emission from CdTe and ZnTe Electro-Optic Crystals," *Jpn. J. Appl. Phys.* **47**, 202-204 (2008).
- [117] Y. Liu, S.-G. Park, and A. M. Weiner, "Terahertz waveform synthesis via optical pulse shaping," *IEEE J. Sel. Top. Quantum Electron.* **2**, 709-719 (1996).
- [118] J. Y. Sohn, Y. H. Ahn, D. J. Park, E. Oh, and D. S. Kim, "Tunable terahertz generation using femtosecond pulse shaping," *Appl. Phys. Lett.* **81**, 13-15 (2002).
- [119] C. D'Amico, M. Tondusson, J. Degert, and E. Freysz, "Tuning and focusing THz pulses by shaping the pump laser beam profile in a nonlinear crystal," *Opt. Express* **17**, 592-597 (2009).
- [120] Y.-S. Lee, N. Amer, and W. C. Hurlbut, "Terahertz pulse shaping via optical rectification in poled lithium niobate," *Appl. Phys. Lett.* **82**, 170-172 (2003).
- [121] M. Yamaguchi and J. Das, "Terahertz wave generation in nitrogen gas using shaped optical pulses," *J. Opt. Soc. Am. B* **26**, A90-A94 (2009).
- [122] J. Desbois, F. Gires, and P. Tournois, "A new approach to picosecond laser pulse analysis, shaping and coding," *IEEE J. Quantum Electron.* **QE-9**, 213-218 (1973).
- [123] A. M. Weiner, D. E. Leaird, D. H. Reitze, and E. G. Paek, "Femtosecond Spectral Holography," *IEEE J. Quantum Electron.* **28**, 2251-2261 (1992).
- [124] P. Tournois, "Acousto-optic programmable dispersion filter for adaptive compensation of group delay time dispersion in laser systems," *Opt. Commun.* **140**, 245-249 (1997).
- [125] F. Verluise, V. Laude, Z. Cheng, Ch. Spielmann, and P. Tournois, "Amplitude and phase control of ultrashort pulses by use of an acousto-optic programmable dispersive filter: pulse compression and shaping," *Opt. Lett.* **25**, 575-577 (2000).
- [126] K. Ohno, T. Tanabe, and F. Kannari, "Adaptive pulse shaping of phase and amplitude of an amplified femtosecond pulse laser by direct reference to frequency-resolved optical gating traces," *J. Opt. Soc. Am. B* **19**, 2781-2790 (2002).
- [127] A. M. Weiner, D. E. Leaird, J. S. Patel, and J. R. Wullert, "Programmable shaping of femtosecond optical pulses by use of 128-element liquid crystal phase modulator," *IEEE J. Quantum Electron.* **28**, 908-920 (1992).
- [128] A. M. Weiner, "Femtosecond pulse shaping using spatial light modulators," *Rev. Sci. Instrum.* **71**, 1929-1960 (2000).
- [129] A. M. Weiner, S. Oudin, D. E. Leaird, and D. H. Reitze, "Shaping of femtosecond pulses using phase-only filters designed by simulated annealing," *J. Opt. Soc. Am. A* **10**, 1112-1120 (1993).
- [130] M. M. Wefers and K. A. Nelson, "Analysis of programmable ultrashort waveform generation using liquid-crystal spatial light modulators," *J. Opt. Soc. Am. B* **12**, 1343-1362 (1995).
- [131] A. Rundquist, A. Efimov, and D. H. Reitze, "Pulse shaping with the Gerchberg-Saxton algorithm," *J. Opt. Soc. Am. B* **19**, 2468-2478 (2002).

- [132] S. Kirkpatrick, C. D. Gelatt, and M. P. Vecchi, “Optimization by simulated annealing,” *Science* **220**, 671-680 (1983).
- [133] R. W. Gerchberg and W. O. Saxton, “A practical algorithm for the determination of the phase from image and diffraction plane pictures,” *Optik* **35**, 237-250 (1972).
- [134] J. R. Fienup, “Phase retrieval algorithms: a comparison,” *Appl. Opt.* **21**, 2758–2769 (1982).
- [135] W. J. Padilla, M. T. Aronsson, C. Highstrete, Mark Lee, A. J. Taylor and R. D. Averitt, “Electrically resonant terahertz metamaterials: Theoretical and experimental investigations,” *Phys. Rev. B* **75**, 041102(R) (2007).
- [136] J. P. Ogilvie, D. Débarre, X. Solinas, J.-L. Martin, E. Beaurepaire, and M. Joffre, “Use of coherent control for selective two-photon fluorescence microscopy in live organisms,” *Opt. Express* **14**, 759-766 (2006).
- [137] S. Chandrasekhar, *Liquid Crystal*, 2nd ed. (Cambridge, 1992).

Summary

Terahertz wave generation from semiconductor thin films and its applications

펄스 형태의 테라헤르츠 기술은 펨토초 레이저에 기반을 둔 광원개발과 검출기술의 개발의 도움으로 광범위하게 연구되어왔다. 특히 분광학 및 보안검사, 생물학적/화학적 식별과 영상, 그리고 결함검사와 같은 분야에서 연구되고 있다. 그러나 테라헤르츠 기술은 공기 중에서 수증기에 의한 흡수, 소형화에 따른 어려움과 상대적으로 긴 파장으로 인한 낮은 분해능과 같이 극복되어야 문제점들이 있다. 특히, 낮은 신호 대 잡음비를 극복하기 위한 더 큰 파워의 테라헤르츠 신호를 얻기 위하여 다양한 반도체 물질들이 연구되었고 이러한 반도체 물질을 이용한 테라헤르츠 기술이 함께 연구되었다. 이러한 물질 중에서 낮은 밴드갭을 갖고 있는 InAs 물질이 테라헤르츠 발생 측면에서 널리 이용되고 있다. InAs의 물질에서 테라헤르츠 발생은 펨토초 레이저에 의해 여기된 정공과 전자의 반도체 표면에서의 이동도 차이에 의한 photo-Dember 효과로 설명될 수 있다. 이와 함께, 수 백 마이크로미터의 길이를 갖는 테라헤르츠 파장은 수 십 마이크로미터의 크기를 갖는 세포영상기술에 적용되기 어려움점이 있다. 이러한 단점을 극복하기 위하여 광학적 대역에서 이용되는 근접장 기술들이 테라헤르츠 기술에 채용되어왔는데 작은 개구를 이용하거나 파장보다 작은 팁 또는 집속된 레이저 펄스를 이용한 방식 등이 연구되고 있다. 이러한 측면에서 테라헤르츠 근접장 연구를 위하여 MBE에서 성장된 InAs 박막을 이용하여 파장이하의 크기에서 집속된 레이저 펄스를 이용한 파장이하 테라헤르츠 발생 분광기 및 테라헤르츠 소형 광섬유 발생기를 개발하였다.

본 논문에서는 파장이하의 테라헤르츠 영상을 구현하는데 있어서 InAs 반도체 표면에서 파장이하의 크기를 갖는 개구에서 발생한 테라헤르츠 펄스의 위상정보의 차이가 유용하게 이용될 수 있음을 분석하고 확인하였다. 파장이하의 InAs 개구에서 발생한 테라헤르츠 펄스는 시간영역에서 빠른 위상변화가 관측되고, 이러한 위상변화는 푸리에영역에서 공간주파수의 분포가 주파수의 파수보다 클 때 생기는 회절에 의한 기하학적인 위상정보를 포함하고 있는 전파계수의 기대값으로 설명될 수 있다. 이러한 위상변화를 이용하여 약 $\lambda/10$ 크기의 테라헤르츠 영상을 성공적으로 얻었다. 이와 더불어 투과형 InAs 박막을 이용하여 광섬유 크기까지 소형화된 테라헤르츠 광섬유 발생기를 개발하였다. InAs 박막은 광축방향으로 진행을 위하여 45도 전달된 광섬유 끝단에 부착되고 이를 이용하여 약 $\lambda/2$ 크기의 테라헤르츠 근접장 영상을 확보하였다. 테라헤르츠 광섬유 발생기는 수 마이크로미터의 광섬유 코어크기까지의 분해능을 얻을 수 있으며, 테라헤르츠 근접장 영상, 분광/편광 연구 및 원거리 전송 분야에 응용될 수 있는 가능성을 가지고 있다. InAs 박막을 이용한 테라헤르츠 근접장 영상기술과 함께 테라헤르츠 파형재단을 이용한 테라헤르츠 기능적 영상기술을 구현하였다. 테라헤르츠 재단 영상기술을 이용하면 기존의 테라헤르츠 영상보다 영상대비가 증가된 영상을 얻을 수 있으며 앞서 기술된 테라헤르츠 근접장 기술과 함께 적용될 수 있다. 두 개의 물질의 영상대비를 증가시켜주는 테라헤르츠 펄스를 얻기 위하여 두 개의 물질의 측정값의 차이를 이용한 cost를 정의하고 이 cost를 반복적으로 증가시키는 방식을 컴퓨터를 이용하여 계속적으로 최적화 재단하여 영상대비가 증가된 주파수 특성이 반영된 테라헤르츠 기능적 영상을 얻었다.

본 논문에 기술된 InAs 박막을 이용하여 개발된 투과형 테라헤르츠 근접장 기술과 기능적 영상 구현을 위한 파형재단 기술이 테라헤르츠의 분해능 한계를 벗어나 세포를 포함하는 수 마이크로미터 크기의 물질에 대한 영상 및 분광연구에 확대적용 될 수 있으리라 기대한다.

감 사 의 글

부족한 제가 이 한편의 논문을 완성하기까지 많은 분들의 도움이 있었습니다. 먼저 학위과정 동안 저를 지도해주신 안재욱 교수님께 진심으로 감사드립니다. 논문 지도뿐만 아니라 교수님께서 말씀해주신 조언과 충고를 통해서 많이 배우고 성장할 수 있었습니다. 또한 바쁘신 일정 중에도 논문심사를 기꺼이 허락해주신 김병윤 교수님, 조용훈 교수님, 정기훈 교수님, 조영달 교수님께 다시 한 번 감사드립니다.

학위과정동안 실험 및 논문에 항상 많은 도움을 준 실험실 식구들, 김영찬 박사, 이상경 박사, 임종석 박사, 강희, 대훈, 한결, 효섭에게 고마운 마음을 전합니다. 특히 테라헤르츠 연구와 관련하여 많은 도움을 준 강희에게 다시 고마운 마음을 전합니다.

마지막으로 언제나 같은 모습으로 힘이 되어준 가족들, 부모님과 동생 모두에게 감사드립니다. 특히 묵묵히 저를 믿어주시고 언제나 끝없는 사랑으로 이끌어 주신 부모님, 부모님의 믿음과 사랑으로 학위과정을 마칠 수 있음에 큰 감사드립니다.

이 력 서

이 름 : 이 민 우

생 년 월 일 : 1980년 8월 29일

학 력

1996. 3. – 1999. 2. 인천 대인고등학교
1999. 3. – 2005. 8. 성균관대학교 물리학과 (B.S.)
2005. 9. – 현재 한국과학기술원 물리학과 석박사 통합과정

경 력

2006. 9. – 2007. 6. 한국과학기술원 물리학과 일반물리학 조교
2007. 9. – 2007. 12. 한국과학기술원 물리학과 전자기학 조교
2008. 3. – 2008. 6. 한국과학기술원 물리학과 광학 조교
2009. 3. – 2009. 6. 한국과학기술원 물리학과 일반물리학 조교

학 회 활 동

1. Kanghee Lee, **Minwoo Yi**, Jin-Dong Song, and Jaewook Ahn, *Generation of polarization shaped terahertz waves*, 한국물리학회 가을학술논문발표회 및 임시총회, BEXCO, 부산, October 19-21, 2011. (우수발표상)
2. **Minwoo Yi**, Kanghee Lee, Jin-Dong Song, Jaewook Ahn, *Sub-wavelength terahertz microscopy using spectro-temporal phase analysis*, IRMMW-THz, Hyatt Regency Downtown, Houston TX USA, October 2-7, 2011.
3. 강병수, 최무한, 이승훈, **이민우**, 안재욱, 최춘기, 민범기, 바비넷 원리가 적용된 복합층 구조 협대역 투명 테라헤르츠 메타물질, 한국광학회 하계학술발표회, BEXCO, 부산, July 14-15, 2011.
4. **Minwoo Yi**, Kanghee Lee, Jin-Dong Song, and Jaewook Ahn, *Temporal and spectral deformation of THz pulses from sub-wavelength size InAs apertures*, Advanced Lasers and Their Applications workshop, Seogwipo, Jeju, May 12-14, 2011.
5. **Minwoo Yi**, Kanghee Lee, Jongseok Lim, Youngbin Hong, Young-Dahl Jho, and Jaewook Ahn, *Terahertz Waves Emitted from an Optical Fiber*, 2nd THz-Bio Workshop, Seoul, January 19-20, 2011. (우수발표상)
6. **Minwoo Yi**, Dae-Hoon Han, Yong-Je Choi, Ki-Hun Jeong, and Jaewook Ahn, *Tailored Terahertz Pulses by Changing Shapes of Planar Metamaterials*, 한국물리학회 가을학술논문발표회 및 임시총회, 보광휘닉스파크, October 20-22, 2010. (우수발표상)

7. Sang-Gil Park, Yongje Choi, **Minwoo Yi**, Jun-Hyuk Choi, Kyung-Hwan Jin, Jong-Chul Ye, Jaewook Ahn, and Ki-Hun Jeong, *High Power THz Photoconductive Antenna Using Localized Surface Plasmon Resonance*, IEEE Optical MEMS and Nanophotonics, Sapporo, Japan, August 9-12, 2010.
8. **Minwoo Yi**, Kanghee Lee, Jongseok Lim, Jaewook Ahn, S. H. Shin, Jin-Dong Song, Youngbin Hong, Young-Dahl Jho, *Terahertz Emission from Optical Fiber Tip and near-Field Microscope Applications*, CLEO/QELS, San Jose, May 16-21, 2010.
9. **Minwoo Yi**, Dae-Hoon Han, Yong-Je Choi, Ki-Hun Jeong, Jaewook Ahn, *Terahertz inductive coupling transparency induced by double asymmetric split resonator*, The 7th Asia-Pacific Laser Symposium, Seogwipo KAL Hotel, Jeju, May 11-15, 2010.
10. **Minwoo Yi**, Kanghee Lee, Jongseok Lim, Youngbin Hong, Young-Dahl Jho, and Jaewook Ahn, *THz waves emitted from an Optical Fiber*, The 7th Asia-Pacific Laser Symposium, Seogwipo KAL Hotel, Jeju, May 11-15, 2010.
11. 이민우, 이강희, 임종석, 신상훈, 송진동, 홍영빈, 조영달, 안재욱, *광섬유를 이용한 테라헤르츠 발생과 근접장 현미경 응용*, 학국광학회 동계학술발표회, 한국과학기술원, 대전, January 20-22, 2010. (우수논문상)
12. 최용제, 이민우, 진경환, 예종철, 안재욱, 정기훈, *Plasmon Enhanced Photoconductive antenna for High Power THz Emission*, 포토닉스학회, 평창, December 3-4, 2009.
13. K.-H. Lee, **M. Yi**, K.-H. Jin, J.-C. Ye, J. Ahn, *Terahertz Imaging of Sub-Wavelength Objects Via Multispectral Reconstruction Algorithm*, IRMMW-THz, Paradise Hotel, Busan, Korea, September 21-25, 2009.
14. **M. Yi**, Y. Kim, D.-S. Yee, J. Ahn, *Modulation-Limited Interference Terahertz Shapes Via One-Dimensional Multilayer Structures*, IRMMW-THz, Paradise Hotel, Busan, Korea, September 21-25, 2009.
15. Kang Hee Lee, **Minwoo Yi**, Jaewook Ahn, *Experimental Study Of Terahertz Radiation Patten In Large-area Photoconductive Antenna*, 한국물리학회 봄학술논문발표회 및 임시총회, 대전, April 23-24, 2009.
16. Youngchan Kim, Dae-Su Yee, **Minwoo Yi**, and Jaewook Ahn, *High-speed, High-resolution Terahertz Spectrometers*, International Symposium on Laser Spectroscopy, Daejeon, November 13-14, 2008.
17. 이강희, 이민우, 진경환, 예종철, 안재욱, *의료 영상 수집용 원격 테라헤르츠 시분해 분광 모듈 개발과 테라헤르츠 영역에서의 압축 측정(compressed Sensing)*, 한국물리학회 가을학술논문발표회 및 임시총회, 광주, October 23-24, 2008.
18. 김영찬, 이민우, 안재욱, 이대수, *High-speed, High-resolution Terahertz Time-Domain Spectrometer Using Asynchronous Optical Sampling*, 한국물리학회 가을학술논문발표회 및 임시총회, 광주, October 23-24, 2008.
19. **Minwoo Yi**, Kanghee Lee, Youngchan Kim, Dae-Su Yee, Jaewook Ahn, *The Multilayer Interference Study of Terahertz Transmission Time-domain Spectroscopy*, 한국물리학회 가을학술논문발표회 및 임시총회, 광주, October 23-24, 2008.
20. Sung-Goo Lee, **Minwoo Yi**, Jaewook Ahn, Jae-Eun Kim, and Hae Yong Park, *Optimization of Photonic Crystal Interfaces for High Efficiency Coupling of Terahertz Waves*, IRMMW-THz, California USA, September 15-19, 2008.

21. 이대수, 김영찬, 이민우, 안재욱, 비 동시성 광 샘플링 방식을 이용한 테라헤르츠 시간 영역 분광법, 한국물리학회 가을학술논문발표회 및 임시총회, 대전, April 17-18, 2008.
22. **Minwoo Yi**, Kyeong-jin Jang, Jaewook Ahn, Inhee Maeng, Joo-Hiuk Son, *Optimal Cd Molar Fraction in Zn_{1-x}Cd_xTe Terahertz Emitters*, CLEO/QELS, Baltimore USA, May 6-11, 2007.
23. **Minwoo Yi**, Kyeong-jin Jang, Inhee Maeng, Joo-Hiuk Son and Jaewook Ahn, *Shapes of Terahertz Pulses Generated via Optical Rectification in ZnTe and CdTe*, Asia-Pacific Microwave Photonics Conference, Jeju, Korea, April 25-27, 2007.
24. **Minwoo Yi**, Kyeong-jin Jang, and Jaewook Ahn, *Terahertz waveforms generated via optical rectification process in zinc-blende crystals*, 한국물리학회 가을학술논문발표회 및 임시총회, 대구, October 19-20, 2006.

연구 업적

1. **Minwoo Yi**, Kyong Hwan Jin, Jong Chul Ye, Jaewook Ahn, *Terahertz Spectroscopy by Spectral Encoding*, (Submitted).
2. Kanghee Lee, **Minwoo Yi**, Jin Dong Song, and Jaewook Ahn, *Polarization shaping of few-cycle terahertz waves*, Optics Express **20** (11), 12463-12472 (May 2012).
3. **Minwoo Yi**, Kanghee Lee, Jin Dong Song, and Jaewook Ahn, *Terahertz phase microscopy in the sub-wavelength regime*, Applied Physics Letters **100** (16), 161110 (April 2012).
4. Sang-Gil Park, Kyong Hwan Jin, **Minwoo Yi**, Jong Chul Ye, Jaewook Ahn, and Ki-Hun Joeng, *Enhancement of terahertz pulse emission by optical nanoantenna*, ACS Nano **6** (3), 2026-2031 (February 2012).
5. Youngchan Kim, **Minwoo Yi**, Bog. G. Kim, and Jaewook Ahn, *Investigation of THz birefringence measurement and calculation in Al₂O₃ and LiNbO₃*, Applied Optics **50** (18), 2906-2910 (June 2011).
6. **Minwoo Yi**, Kanghee Lee, Jongseok Lim, Youngbin Hong, Young-Dahl Jho, and Jaewook Ahn, *Terahertz Waves Emitted from an Optical Fiber*, Optics Express **18** (13), 13693-13699 (June 2010).
7. Youngchan Kim, Dae-Su Yee, **Minwoo Yi**, and Jaewook Ahn, *High-Speed High-Resolution Terahertz Spectrometers*, Journal of Korean Physical Society **56** (1), 255-261 (January 2010).
8. **Minwoo Yi**, Youngchan Kim, Dae-Su Yee, and Jaewook Ahn, *Terahertz Frequency Spreading Filter via One-dimensional Dielectric Multilayer Structures*, Journal of Optical Society of Korea **13** (3), 398-402 (September 2009).
9. Youngchan Kim, Ki-Bok Kim, Dae-Su Yee, **Minwoo Yi**, and Jaewook Ahn, *High-Speed High-Resolution Terahertz Time-Domain Spectrometer*, Hankook Kwanghak Hoeji **19** (5), 370-375 (October 2008).
10. Kanghee Lee, **Minwoo Yi**, and Jaewook Ahn, *Modleing of THz Frequency Spectrum via Optical Rectification in THz Time Domain Spectroscopy*, Journal of the Korean Society for Nondestructive Testing **28** (2), 119-124 (April 2008).
11. **Minwoo Yi**, Kanghee Lee, Inhee Maeng, Joo-Hiuk Son, R. D. Averitt, and Jaewook Ahn, *Tailoring the Spectra of Terahertz Emission from CdTe and ZnTe Electro-Optic Crystals*, Japanese Journal of Applied Physics **47** (1), 202-204 (January 2008).

12. **Minwoo Yi**, Kanghee Lee, and Jaewook Ahn, *Optimal Molar Fractions of Ternary Zinc-blende Terahertz Emitters*, Journal of the Korean Physical Society **51** (2), 475-479 (August 2007).

특 허

1. Jaewook Ahn, **Minwoo Yi**, *Terahertz Single-point fiber detector using thin electro-optical materials and manufacturing method thereof*, Korea Patent, 10-2012-0009146 (국내출원).
2. Jaewook Ahn, Kanghee Lee, **Minwoo Yi**, Jongseok Lim, Youngdahl Cho, Yong-bin Hong, Jihoon Jeong, *Device for terahertz emitter using thin indium arsenic film optical fiber and manufacturing method thereof*, Korea Patent, 10-1067368 (2011-09-19).
3. Jaewook Ahn, Kanghee Lee, **Minwoo Yi**, *Contact type terahertz time domain spectrum device*, Korea Patent, 10-1017796 (2011-02-18).

출 판 물

1. G.-S. Park et al., *Convergence of Terahertz Sciences in Biomedical Systems*, Ch 7. "Sub-single Cycle Pulses of Electromagnetic Radiation," written by Jaewook Ahn and **Minwoo Yi**, (Springer, New York, 2012).